Search for beyond Standard Model physics with high-p_T leptons

Viazlo, Oleksandr

2017

Link to publication

Total number of authors:
1

Search for beyond Standard Model physics with high-p_T leptons

Oleksandr Viazlo
Department of Physics | Faculty of Science

Search for beyond Standard Model physics with high-p_T leptons

Oleksandr Viazlo

LUND UNIVERSITY Department of Physics Lund University Box 118 SE-221 00 Lund SWEDEN	DOCTORAL DISSERTATION
	Date of issue 2017-01-24
Author: Oleksandr Viazlo	Sponsoring organization

Search for beyond Standard Model physics with high-p_T leptons

Abstract: This thesis covers four different topics related to the physics analysis in the ATLAS experiment that uses protonproton collisions data provided by the Large Hadron Collider. The first topic is focused on the numerical simulation of the Transition Radiation Tracker which is one of the ATLAS tracking detectors. The implementation of the alternative Argon based gas mixtures used in the drift tubes is described. A performance study with focus on the hit and track parameters with respect to the gas mixture is discussed as well.

The second topic is related to the ATLAS luminosity monitor called LUCID. A number of studies are presented from the design phase of the detector and of its calibration system as well as detector operation, the performance and luminosity measurements.

The two last topics are analyses that searches for beyond Standard Model physics with the ATLAS detector. The first search presented in the thesis is done in a final state with same-sign electron pairs using the data collected at a center of mass energy of $\sqrt{s} = 8$ TeV. No significant excess above the predictions of the Standard Model is observed. Limits on the fiducial cross section for new physics as a function of the invariant mass of electron pairs have been set as well as mass limits for doubly charged Higgs models.

The second analysis is focused on a search for a new heavy charged gauge boson in the final state with one lepton and missing transverse momentum at $\sqrt{s} = 13$ TeV. Since no significant deviation from the Standard Model is observed, limits on a new heavy charged gauge bosonmass are set.

Key words: LHC, ATLAS, TRT, LUCID, Luminosity, Beyond Standard Model, Doubly Charged Higgs:

Classification system and/or index terms (if any)

Supplementary bibliographical information	Language English
ISSN and key title	ISBN 978-91-7753-157-9

Recipient's notes	Number of pages 212	Price
	Security classification	

Signature   Date 2017-01-10

Search for beyond Standard Model physics with high-p_T leptons

Oleksandr Viazlo

LUND

UNIVERSITY

Abstract

This thesis covers four different topics related to the physics analysis in the ATLAS experiment that uses proton-proton collisions data provided by the Large Hadron Collider.

The first topic is focused on the numerical simulation of the Transition Radiation Tracker which is one of the ATLAS tracking detectors. The implementation of the alternative Argon based gas mixtures used in the drift tubes is described. A performance study with focus on the hit and track parameters with respect to the gas mixture is discussed as well.

The second topic is related to the ATLAS luminosity monitor called LUCID. A number of studies are presented from the design phase of the detector and of its calibration system as well as detector operation, the performance and luminosity measurements.

The two last topics are analyses that searches for beyond Standard Model physics with the ATLAS detector. The first search presented in the thesis is done in a final state with same-sign electron pairs using the data collected at a center of mass energy of $\sqrt{s} =8$ TeV. No significant excess above the predictions of the Standard Model is observed. Limits on the fiducial cross section for new physics as a function of the invariant mass of electron pairs have been set as well as mass limits for doubly charged Higgs models.

The second analysis is focused on a search for a new heavy charged gauge boson in the final state with one lepton and missing transverse momentum at $\sqrt{s} =13$ TeV. Since no significant deviation from the Standard Model is observed, limits on a new heavy charged gauge boson mass are set.

Acknowledgements

Preface

The studies reported in this thesis were performed during my work with the ATLAS experiment at the Large Hadron Collider (LHC) in 2012-2016. All the studies are based on data collected by the ATLAS experiment or related to the ATLAS detector performance. ATLAS is a multi-purpose detector which is registering results of hadron collisions at the LHC. It consists of a set of subdetectors which perform dedicated tasks providing specific information about particles created in collisions. While LHC can collide both proton and lead beams, this thesis focuses on proton-proton collision data.

The first study concerns one of the ATLAS tracking subdetectors – the Transition Radiation Tracker (TRT). It uses a gas mixture as an active detector volume to detect charged particles. The TRT was designed to use only one type of gas mixture, based on Xenon. However, some parts of the detector started to leak after few years of running. Thus, to decrease the operational costs of the detector, it was decided to switch to a cheaper gas mixture based on Argon. My task was to rewrite the TRT simulation software, used for Monte Carlo (MC) simulation of physics processes, to support the new gas mixture. It was a very challenging yet interesting task, because I had to review the whole chain of the numerical simulation of the TRT detector and add support for the new gas in each step. After the implementation was completed, I did a performance study of the TRT with focus on the hit and track parameters for the Argon and Xenon gas mixtures.

Later in my PhD studies in 2014, I joined the LUCID group, which was designing the new LUCID-2 detector. My involvement with LUCID lasted for more than two years. The LUCID detector is a luminosity detector which measures the collision rate of the hadron-hadron interactions in ATLAS. The luminosity measurements are crucial because luminosity is used for all analyses which measure or put limits on cross sections of processes. During the design phase, many tests were done to find an optimal design and the optimal parameters for various detector components. During

the assembly and installation phase, a number of tests were done to make sure that all components performed as they should. An overall test of the system was done to make sure that no damage has been done during the installation of the detector. During the operation phase, which is still ongoing, many studies have been made to understand the performance of the calibration system and the detector.

I contributed to all the steps mentioned above. I took part in the development of the LUCID design and particularly the design of the calibration system. I made a series of tests to find the optimal design parameters of the LED and laser diffusers used to distribute LED and laser signals evenly and deliver them to all detector channels. I spent a lot of time investigating the behavior of the LED system as well as the PMT and PIN-diode signal behavior. I also conducted tests with Bi-207 radioactive sources which are used to monitor the photomultiplier (PMT) gain. I participated in the detector assembly in the clean room and did detector testing during this process. Testing of the LED and laser diffusers were done to cross-check the integrity of fibers and the homogeneity of signals between all PMTs. Also, a temperature stress test was performed in order to understand what maximum temperature can be tolerated without destroying the detector during the beampipe bake-out procedure. In the operational phase, the main focus was on understanding the aging of the PMTs and the possibility of improving the calibration system. Lastly, I became the ATLAS Forward Detectors Run Coordinator for five months, where my task was to ensure the successful operation of LUCID and to verify the correctness of the measured luminosity during the ATLAS data taking.

During the second half of my studies, I was doing searches for new physics beyond the Standard Model (BSM) in final states with isolated leptons. The first search I did was an inclusive search with same-sign lepton pairs. The analysis was performed in three channels: $e^{\pm}e^{\pm}$, $\mu^{\pm}\mu^{\pm}$ and $e^{\pm}\mu^{\pm}$. My task was to perform a complete analysis with the $e^{\pm}e^{\pm}$ channel and to make cross-checks for other channels. To achieve this, I was doing event and lepton selections, a study of the MC inputs, testing of the charge flip and non-prompt background modelling, optimization of the selection criteria, verification of prompt background predictions, estimation of the systematic uncertainties and provision of final numbers for the limit settings. Also, I was studying the hypothetical doubly charged Higgs signal, calculating the total efficiency of the signal selection and making the bin width optimization for the limit setting for the doubly charged Higgs.

The second analysis was a search for a new heavy spin-1 gauge boson, namely, W'. The final state of interest was a high momentum lepton and significant missing transverse momentum observed in the detector (which corresponds to a particle which escapes the detector without interacting with it, for example, a neutrino). The analysis was performed in the electron and muon channels. I was working on the muon channel, making an event and lepton selection, studying the behavior of the missing transverse momentum, testing fake background predictions and performing cross-checks both in muon and electron channels. Also, I was working on a production of the new MC simulation samples of the top and diboson backgrounds which would provide enough statistics in the whole signal region and significantly reduce the dominant systematic uncertainty. However, the problem appeared to be much deeper than expected, thus it was not solved completely in time for the publication and I had to hand it over to the analysis team which started working with the new 2016 data. I also made a study of the signal selection sensitivity to the so-called Simplified Dark Matter models, which are the recommended benchmark models for searches during the current running period at the LHC.

The results of the research activities described above were included in the publications:

- G. L. Alberghi et al., *Choice and characterization of photomultipliers for the new ATLAS LUCID detector*, JINST **11** no. 05, (2016) P05014.

- ATLAS Collaboration, G. Aad et al., *Search for anomalous production of prompt same-sign lepton pairs and pair-produced doubly charged Higgs bosons with $\sqrt{s} = 8$ TeV pp collisions using the ATLAS detector*, JHEP **03** (2015) 041, `arXiv:1412.0237 [hep-ex]`.

- ATLAS Collaboration, M. Aaboud et al., *Search for new resonances in events with one lepton and missing transverse momentum in pp collisions at $\sqrt{s} = 13$ TeV with the ATLAS detector*, `arXiv:1606.03977 [hep-ex]`.

Also, I presented my results at two international conferences with published proceedings:

- O. Viazlo, *ATLAS LUCID detector upgrade for LHC Run 2*, PoS **EPS-HEP2015** (2015) 275.

- O. Viazlo, *Searches for new physics in high-mass fermionic final states and jets with the ATLAS detector at the LHC*, PoS **DIS2016** (2016) 109.

Contents

Chapter 1.

Physics of the Standard Model and Beyond

1.1. Introduction

Particle physics studies the elementary constituents of the universe and how they interact with each other. One of many questions which it attempts to address is the origin of our universe and what it consists of. Like any field of science, particle physics is based on the two pillars: experiment and theory. By making experimental observations, one obtains certain information, and by systematizing this information and making relations between the pieces, one aims to develop a theory or a model which would explain everything. The more different observations the model can explain, the more confidence one can have that the model works and that it can be used to predict as-yet unmeasured effects.

This was the case with the so-called Standard Model (SM) which became extremely popular in the last century because it was able to describe hundreds of newly observed particles in collider experiments. The SM describes with remarkable precision three types of particle interactions, with only the gravitational interaction left unincluded. Thus a significant effort is ongoing to try to incorporate gravity into the SM to obtain a complete model.

However, despite the fact that the SM agrees amazingly well with experimental measurements, and even if gravity is not taken into account, there are many reasons to think that the SM is not complete. There is a set of unsolved questions which the SM cannot address (e.g. neutrino masses, dark matter, matter-antimatter asymmetry).

Because all known elementary particles fit well in the SM, these problems make us believe that there is potentially new physics (and correspondingly new particles) in TeV or above-TeV regimes which can solve these problems. The Large Hadron Collider provides us with a possibility to explore a TeV energy frontier. This is why many analyses are focused on an investigation of new energy regime and search for possible deviations from the SM which can be hints of new physics. Since the SM was introduced more than 30 years ago, many theorists spent a tremendous amount of time and effort to create a plethora of models which extend the SM and address multiple unsolved problems. These models can predict signatures and criteria which are most sensitive to the possible new physics and motivate strategies of the searches.

This chapter contains a brief description of the SM, its problems and some Beyond Standard Model (BSM) models which have been developed to address several of these problems.

1.2. The Standard Model

1.2.1. Elementary particles

The SM is a very successful model which describes all the known particles in existence to a remarkable degree of accuracy. All of the SM particles are fundamental particles (they have no internal structure) that make up the matter and forces in the universe. The elementary particles can be classified into two groups:

- the spin-1/2 fermions, which obey Fermi-Dirac statistics,

- the bosons, which obey Bose-Einstein statistics and have integer spin values.

The matter in the universe is made of fermions, which are classified into three generations. Each generation consists of two electromagnetically charged quarks and one charged lepton as well as an associated neutral neutrino. Fermions from different generations have the same charges but differ by mass. One quark from a generation has charge +2/3e, while the other has -1/3e. Charged leptons carry an integer charge -1e. Experimental evidence supports the hypothesis that the number of fermion generations has to be three [1]. Each higher generation consists of more heavy particles which decay to lighter particles from lower generations, and that can be interpreted as an explanation of why the observed stable matter in the universe is

made exclusively from particles of the first generation. In addition to electric charge, quarks also carry colour charge, which allows two otherwise identical quarks to jointly occupy an energy and spin state inside a hadron.

There are three different "colours" within the SM, namely: red, green and blue. The number of colours has been experimentally confirmed by measurements of the ratio of hadronic to $\mu^+\mu^-$ production cross sections in the electron-positron annihilation [2]. Each fermion has an associated antiparticle, which is the particle with opposite charges but with identical mass and spin. A list of fermions and their properties is presented in Table 1.1.

Generation	Leptons			Quarks		
	Flavour	Mass [GeV]	Charge [e]	Flavour	Mass [GeV]	Charge [e]
1st	ν_e	$< 2 \times 10^{-9}$	0	up	$2.2^{+0.6}_{-0.4} \times 10^{-3}$	2/3
	e	0.000511	-1	down	$4.7^{+0.5}_{-0.4} \times 10^{-3}$	-1/3
2nd	ν_μ	< 0.00019	0	charm	1.27 ± 0.03	2/3
	μ	0.106	-1	strange	$96^{+8}_{-4} \times 10^{-3}$	-1/3
3rd	ν_τ	< 0.0182	0	top	174.2 ± 1.4	2/3
	τ	1.777	-1	bottom	$4.18^{+0.04}_{-0.04}$	-1/3

Table 1.1.: The fermion particle generations with their electrical charges and masses.

The remaining particles described by the SM are bosons. These particles have integer values of spin. A list of all known elementary bosons is shown in Table 1.2. Many experimental measurements obtained with the help of colliders prove the existence of the bosons. The first evidence of the Z and W bosons was obtained by the UA1 and UA2 collaborations [3,4] which made the first measurements of their masses. The gluon has been experimentally confirmed in electron-positron annihilation at the PETRA storage ring by observation of the three-jet topology [5]. The Higgs boson was discovered by the ATLAS and CMS collaborations in 2012 [6,7].

1.2.2. Types of interactions and fields

The SM is a Quantum Field Theory that describes interactions between particles. There are three fundamental forces which are incorporated into the SM framework: the electromagnetic, the weak and the strong forces. These forces are mediated between

Boson	Mass	Charge [e]	Spin	Interaction	Range	Interact with
photon	0	0	1	Electromagnetism	∞	charge
8 gluons	0	0	1	Strong	10^{-15} m	colour
$W^{\pm}$	80.4 GeV	± 1	1	Weak	10^{-18} m	weak isospin
Z	91.2 GeV	0	1			+ hypercharge
Higgs	125 GeV	0	0			

Table 1.2.: The Standard Model bosons with their masses and charges, and corresponding interaction types.

matter particles (elementary or composite) by carrier particles with spin 1, which are called gauge bosons. Each fundamental force has its own gauge boson(s): the electromagnetic force is mediated via an exchange of massless photons, the strong force is mediated by massless gluons, while the weak force is transmitted by massive W and Z bosons. In quantum field theories the forces are given by the dynamics of the quantised, relativistic and locally interacting fields. The electromagnetic, weak and strong forces have different strengths and act over different ranges (see Table 1.2). Both types of fundamental matter particles, leptons and quarks, interact through the electromagnetic and weak forces (except neutrinos, which interact only weakly), whereas only quarks interact strongly.

The SM combines two main theories built to describe all three fundamental interactions, the force-carrier bosons and the matter particles. The first one is the Glashow-Salam-Weinberg (GSW) theory which unifies the electromagnetic and weak interactions. The second theory, quantum chromodynamics (QCD), describes the strong interactions of quarks and gluons. Both GSW and QCD theories are constrained by principles of local gauge invariance of the fields based on the $U(1)_Y \times SU(2)_L$ weak isospin and hypercharge, and $SU(3)_C$ color symmetry groups, respectively. Thus, the SM is a Quantum Field Theory based on the $U(1)_Y \times SU(2)_L \times SU(3)_C$ symmetry group with $1 + 3 + 8 = 12$ generators that correspond to 12 massless gauge bosons (see Table 1.2), if the gauge symmetry is unbroken. Both GSW and QCD theories, unlike the quantum electrodynamics (QED), are non-abelian, which determines the property of self-interactions between the corresponding gauge boson fields. In particular, self-interaction of the gluon field leads to essential characteristics of the QCD, such as asymptotic freedom and confinement.

The weak W and Z bosons have been experimentally proven to be massive, indicating that the electro-weak symmetry of the SM is spontaneously broken. In the SM the spontaneous symmetry breaking is implemented by the Higgs mechanism. In this approach, a doublet of complex fields is introduced which interacts with the SM particles and has a potential with an infinite number of degenerate vacuum states. The choice of one particular ground state with nonzero vacuum expectation value, v, breaks the $SU(2)$ symmetry and results in one scalar neutral particle (Higgs boson) that must be present in the SM. As was mentioned above, the existence of the Higgs boson has been confirmed recently.

The Higgs mechanism gives masses not only to Z and W gauge bosons but also to fermions through the corresponding Yukawa coupling terms. An important property of the Higgs field is that it flips the left-handed fermions into right-handed fermions and vice versa. As right-handed neutrinos have not been observed and, thus, are not included in the SM, the left-handed neutrinos can not interact with Higgs boson and remain massless within the SM. However, as will be discussed further, there is experimental evidence which proves that neutrinos are massive.

The SM has been tested in thousands of measurements by many different experiments. All measurements are in remarkably good agreement with theoretical predictions. For example, comparison of the latest measurements of different SM process cross sections by the ATLAS collaboration with theoretical predictions is shown in Figure 1.1.

1.3. Physics Beyond the Standard Model

1.3.1. Problems of the Standard Model

The SM is currently the best description of the micro-world. It predicted many particles before their discovery. However, despite its great phenomenological success, the SM does not describe the full picture and is believed to be incomplete. The following *big questions* [9] remain unsolved within the SM:

- *The particle content of the dark matter.* An existence of the dark matter is confirmed in the astrophysics and cosmology. The most compelling hypothesis is that the dark matter is made out of massive neutral particles weakly interacting with the
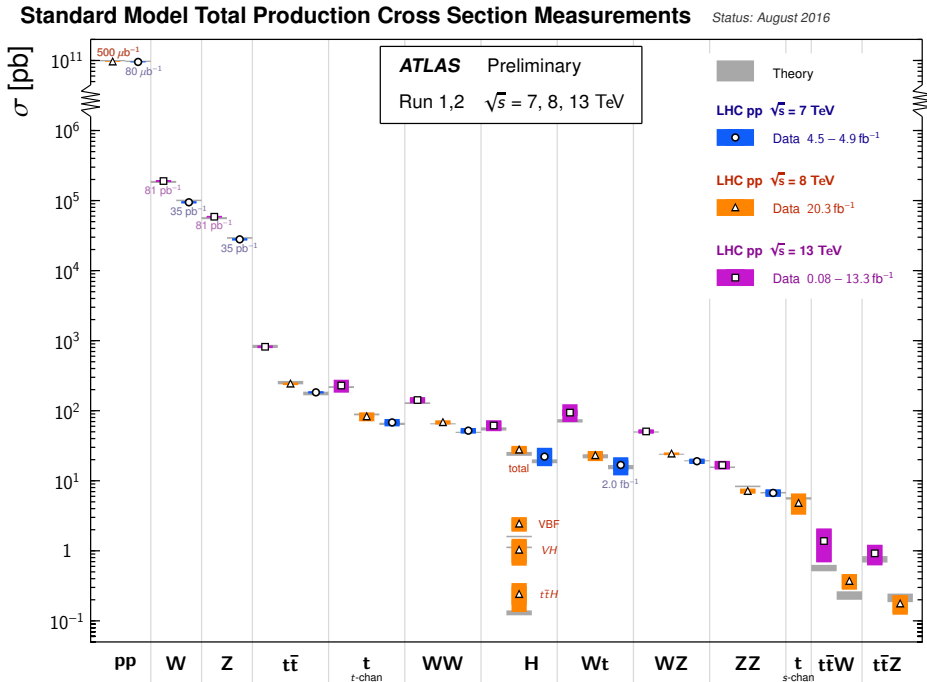
Figure 1.1.: Summary of the Standard Model total production cross section measurements made by the ATLAS experiment, compared to the corresponding theoretical expectations [8]. Theoretical predictions and their errors are shown with gray bars, while experimental measurements are shown with hollow markers with colored bars, which represent measurement errors. All theoretical expectations were calculated at next-to-leading order or higher in perturbative QCD.

matter (WIMPs). They are expected to have a mass of order less than a TeV. In this scenario, the WIMPs can be directly produced at high energy colliders.

- *Origin of the mass.* The Higgs Mechanism is introduced in the SM ad hoc. The Higgs boson is the first scalar fundamental particle observed in nature. It gives masses to the fermions, *W*, and *Z* bosons. However, the SM does not tell us why this happens. It is still not clear whether this particle is fundamental or composite, or if there are other Higgs bosons.

- *Hierarchy problem.* The mass of the Higgs boson contains large contributions from radiative loop corrections. In particular, it is sensitive to heavy particles of the SM (as well as to hypothetical particles of new physics that might lie at the TeV scale). In the SM these corrections are quadratically divergent which leads to an unnaturally high mass of the Higgs boson. It is possible to restore the Higgs mass to a proper value through *fine-tuning*, but this is considered to be unnatural. Some models which predict new physics and new particles at TeV or above scale allow avoiding this problem by compensating problematic terms in the Higgs mass formula (e.g. little Higgs model [10]).

- *Origin of matter-antimatter asymmetry.* Amounts of matter and antimatter created after the Big Bang are expected to be equal. However, the universe visible from Earth is made almost entirely of matter. A possible explanation could come from new physics predicting baryon number violation, CP-violation and new scalar particles at the TeV scale.

- *Origin of mass hierarchy of fermion masses.* The mass of the top quark is almost 10^6 times larger than masses of up and down quarks, which calls for an explanation. Discovery of new particles would provide additional clues to this puzzle.

- *Neutrino mass.* The experimental results on neutrino oscillations [11] confirm that neutrinos are massive particles. However, in the SM no mass term for the neutrino particles is incorporated. An extension of the SM with a model containing a massive right-handed, sterile neutrino can solve this problem. In such a model, the SM neutrinos acquire mass and the so-called seesaw mechanism explains the smallness of their masses [12].

- *Gravity is not part of the SM.* The Quantum Field Theory, which provides a theoretical framework for the SM, is used to describe the micro-world, while the General Relativity, used to describe gravity, works in the macro-world and cannot

be easily quantized. It is not an easy task to fit them into a single framework of the SM comfortably. However, a unification is possible in the context of the String Theory.

These questions unsolved by the SM motivate us to continue searches for new physics beyond the SM at the TeV scale and higher.

1.3.2. Models beyond the Standard Model

Despite the described problems above, the incredible accuracy of the SM, thus far measured up to TeV scale, leads to the understanding that SM is simply incomplete rather than incorrect. This is why a first step to build a new model which could address some of the problems is first to verify that it agrees with the SM predictions. This is why many new models aim to expand the SM rather than to provide an entirely new approach. Such models are typically called Beyond Standard Models (BSM). There is a plethora of models which address SM problems in many different ways.

This thesis covers two searches. One of them is focused on the search for new physics with same-sign dilepton signature. Such final state can be produced in many BSM models, e.g. models which predict double charged Higgs or Majorana neutrino. Another one is focused on the search for new heavy spin-1 gauge boson, namely W′, with lepton plus missing transverse momentum signature. BSM models which potentially can be confirmed by these searches are discussed below.

In general, there are many possibilities and ways to go beyond the SM. Some famous examples can be found in ref. [13]. Many models are based on the idea of Grand Unified Theory [14], which seeks to find a simple symmetry group which are based on the SM symmetry group and contains all known interactions [15,16]. One such model is the model based on the $SO(10)$ group, which leads to intermediate symmetry:

$$SO(10) \rightarrow SU(3)_C \times SU(2)_L \times SU(2)_R \times U(1)_{B-L} \qquad (1.1)$$

It yields the so-called Left-Right Symmetric Model (LRSM), which adds right-handed weak interaction to the SM and accordingly new right-handed W_R and Z_R gauge bosons. The breaking of $SU(2)_R \times U(1)_{B-L} \rightarrow U(1)_Y$ occurs due to a triplet of complex Higgs fields, consisting of Δ_R^0, Δ_R^+ and Δ_R^{++}, at a high energy scale [17]. Doubly-charged

Higgs Δ_R^{++} can decay to two same-sign lepton pair, which makes it a signal candidate for the same-sign dilepton analysis described in Chapter 5. Spontaneous breaking of this symmetry provides mass to the right-handed W_R. Since $SU(2)_R$ symmetry is broken at higher energy scale than $SU(2)_L$, it makes W_R a signal candidate for the analysis described in Chapter 6. This model addresses a few SM problems. Firstly, it assumes Majorana nature of the neutrinos and assigns mass to them by a seesaw mechanism and allows scenarios in which the neutrino masses are naturally light [12]. Secondly, LRSM provides spontaneous parity breaking [18], while in the SM parity is broken explicitly.

Another set of models is little Higgs models. These models address hierarchy and fine-tuning problems described above. The idea of the models is that the Higgs boson becomes a pseudo-Goldstone boson due to some global symmetry breaking at a TeV energy scale. The quadratic divergence corrections present in the SM Higgs scalar mass calculation from one-loop contributions from the SM top quark and gauge bosons will be canceled by the identical contributions from new heavy gauge bosons and new heavy fermionic states (to oppose the top contribution) introduced by the model [10, 19]. These models assume production of doubly charged Higgs and new heavy charged gauge bosons, which are particles of interest for the searches presented in this thesis.

In addition to the models described above there are many other theories and models, such as Kaluza-Klein, Zee-Babu, SUSY and others which either assume new charged spin-1 boson or same-sign dilepton final state, which proves the high potential of the BSM searches presented in this thesis.

Chapter 2.

The LHC and The ATLAS experiment

The Large Hadron Collider (LHC) is a circular accelerator at CERN with a designed center-of-mass (CM) energy of proton-proton collisions of 14 TeV and up to 2.3 TeV per nucleon for heavy ion collisions. Collisions are registered by the four large experiments: ATLAS, CMS, ALICE, and LHCb. This chapter contains a short overview of the LHC performance as well as a description of the ATLAS experiment.

2.1. The LHC performance and beam structure

In what follows, only proton-proton collisions are considered. The proton bunches are delivered to the LHC by an injector chain that consists of Linac2, the Proton Synchrotron Booster (PSB), the Proton Synchrotron (PS), the Super Proton Synchrotron (SPS) [20]. The schematic picture of the full acceleration chain is shown in Figure 2.1.

The maximum number of bunches possible in the LHC is 2808 [21]. Bunches are grouped in so-called bunch trains. The design distance between the bunches in the train is 25 ns. The longest possible train in the LHC during normal operation consists of 72 bunches with gaps between the trains of at least 12 empty bunches [20] The energy of the protons in the injected bunches equals 450 GeV and the bunches are injected from the SPS one after another. When the injection is done, the fill is complete and an additional acceleration in the LHC starts. When the bunches have been accelerated to the collision energy (up to 7 TeV) and when all experiments are ready to record data, the so-called physics run starts. During physics runs all the LHC experiments collect physics data for further offline analysis.
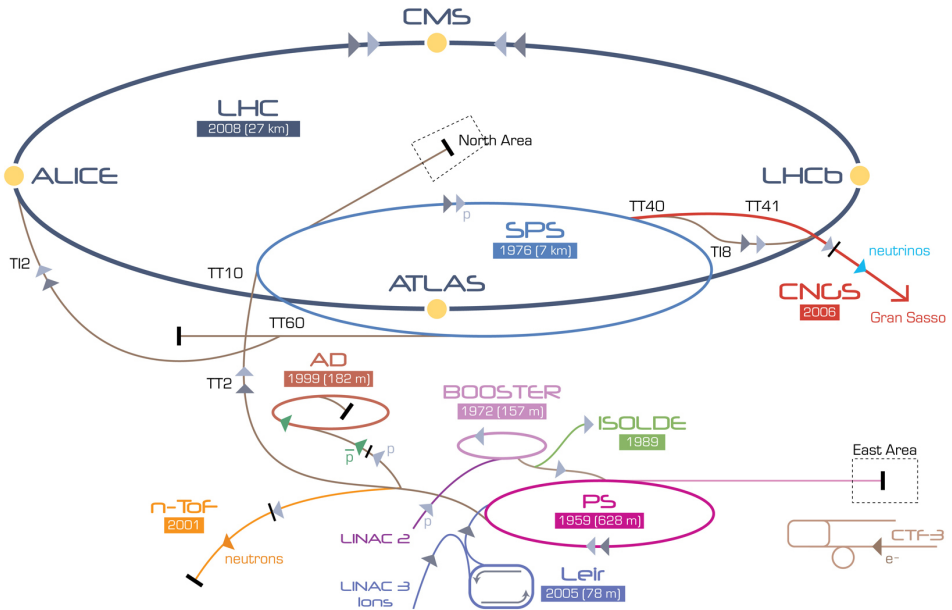
Figure 2.1.: Schematic picture of the LHC accelerator complex at CERN.

The number of protons in the bunches is decreasing with time due to the proton-proton (pp) collisions. To achieve maximum delivered luminosity to the experiments it is therefore optimal to dump the beams when their intensity becomes too low and to inject new beams into the ring. After the beams have been dumped, the magnetic field (which is equivalent to the current in the magnets) has to be slowly decreased to make the machine ready for new 450 GeV bunches and a new acceleration cycle. The period between fills, where there are no bunches in the LHC, is called the interfill period. In the interfill period, the ATLAS sub-detectors perform calibrations to prepare for the next run. The luminosity distribution during the physics runs shown in Figure 2.2 demonstrates the decrease of the luminosity over the run as well as the interfill period between the runs.

It is worth mentioning that there are other types of runs, which are used for LHC beam performance studies or special detector tests. One example of such a special run is the so-called van der Meer (vdM) run which is used to calibrate the luminometers in the experiments as will be described in Section 4.4.2.

The LHC running schedule is split into different periods which are called Runs (not to be confused with physics runs mentioned above). Run-1 started at the LHC
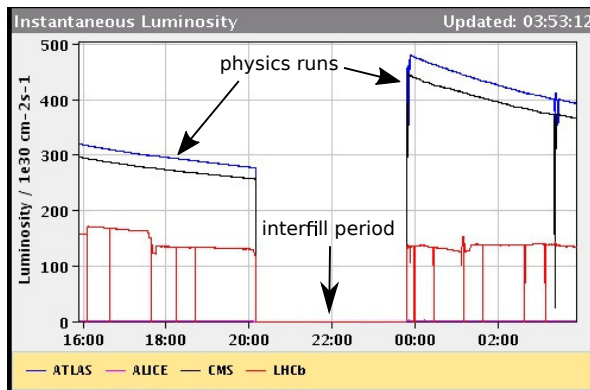
Figure 2.2.: Example of the luminosity during two runs as a function of time. The period with zero luminosity between the runs corresponds to the interfill period used by the detector groups to make calibrations.

startup and was using a 50 ns bunch spacing in the trains and had a center-of-mass energy of 7 and 8 TeV. Run-2 started in 2014 and is still ongoing at the time of writing. The center-of-mass energy of the collisions is 13 TeV and the bunch spacing is 25 ns (which corresponds to the designed bunch spacing). During Run-3 and Run-4 LHC will operate with 14 TeV CM energy and with a significantly increased luminosity. The total planned luminosity to be delivered by LHC to the experiments is 3000 fb^{-1}. Information about all running periods is shown in Figure 2.3.

2.2. The ATLAS experiment

The ATLAS (A Toroidal LHC ApparatuS) experiment is a multi-purpose detector at the LHC. It has a forward-backward symmetric design with respect to the Interaction Point (IP). It consists of the Inner Detector (ID), the Electromagnetic (EM) and hadronic calorimeters and the Muon Spectrometer (MS). The magnetic field is provided by the magnet system. A detailed description of each subsystem is presented below.

2.2.1. The ATLAS coordinate system

An illustration of the coordinate system and the track parameters are shown in Figure 2.4. The base vectors e_x, e_y and e_z shown in the figure represent the x-, y- and
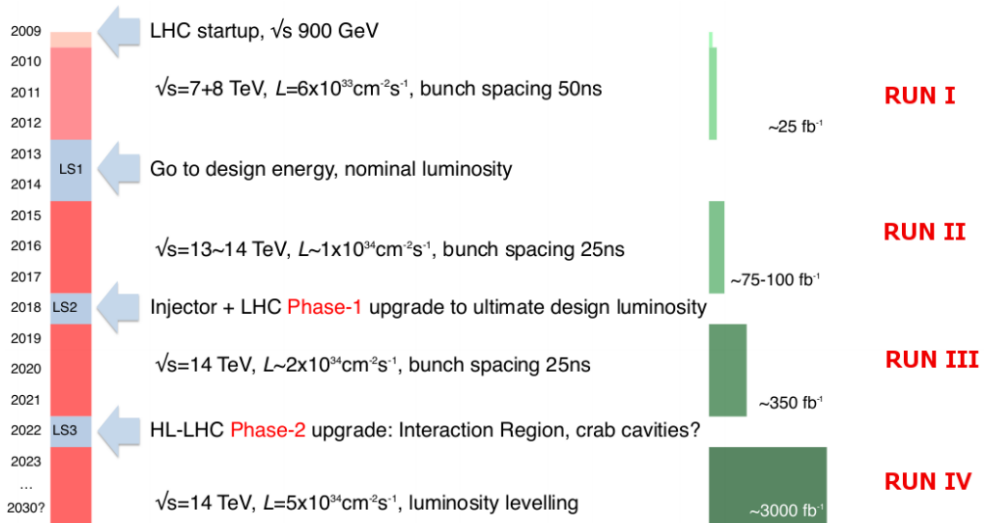
Figure 2.3.: An approximate timeline of the scheduled LHC upgrades with planned integrated luminosity to be delivered to the experiments [22].

z-axes respectively. The vector e_x is pointing to the center of the LHC ring; vector e_y is pointing vertically upward; vector e_z is pointing along the beam axis. Tracks of charged particles in ATLAS are parameterized with these five parameters [23]:

- The transverse impact parameter d_0, which is the distance to the beam axis in the $x - y$ plane.

- The longitudinal impact parameter z_0, which is the distance to the coordinate system origin in z-direction.

- The azimuthal angle ϕ, measured in the $x - y$ plane starting from vector e_x.

- The polar angle θ, measured from vector e_z.

- The charge of the particle divided by its momentum, q/p, which characterizes the track curvature.

2.2.2. Magnet System

The ATLAS Magnet System [25] provides a magnetic field to bend tracks of charged particles. This is used to measure the momentum of the particles as well as their charge
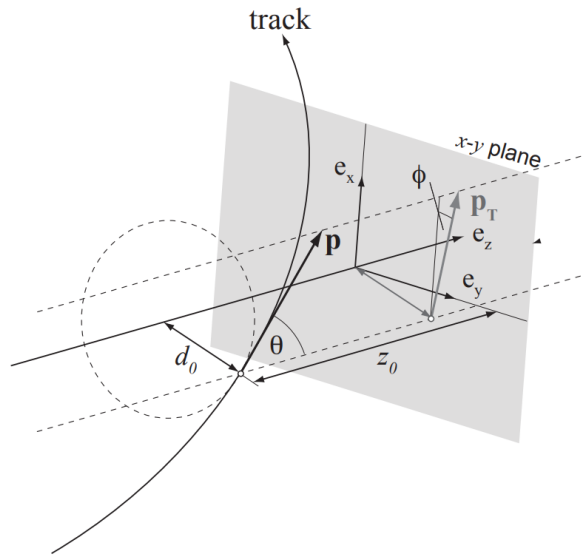
Figure 2.4.: Track parameterization in the ATLAS coordinate system [24].

by the curvature of the track. The magnet system consists of three superconducting magnets:

- The Central Solenoid. It is placed around the Inner Detector and provides a 2 T magnetic field directed along the beam axis inside the ID. Since it is placed before the EM calorimeter, the material budget has to be low in order to not distort measurement in the calorimeter.

- The Barrel Toroid. Provides ~ 0.5 T inside the barrel muon spectrometer.

- The End-Cap Toroids. Provides ~ 1.0 T inside the toroid muon spectrometer.

The magnet configuration is shown in Figure 2.5.

2.2.3. The inner detector

The innermost detector of ATLAS and the closest one to the interaction point (IP) is the inner detector (ID). The main purpose of the ID is to reconstruct tracks of all charged particles which pass through the detector and to measure their momenta. Tracking detectors also have to provide information on the sign of the electrical charge of the

Central Solenoid

Barrel Toroids

End-Cap Toroids
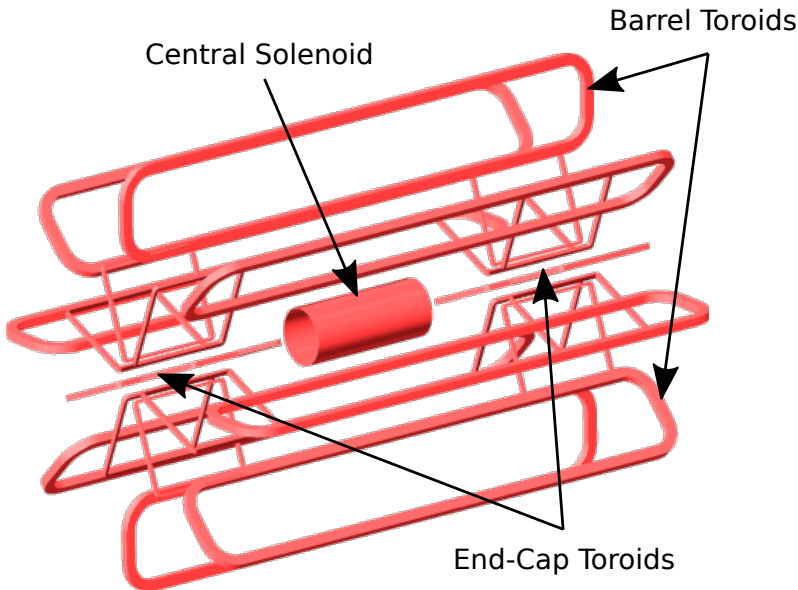
Figure 2.5.: Illustration of the ATLAS magnet system.

particles, which is why a strong magnetic field is applied within the ID, which makes tracks of particles with different charges bend into different directions.

Vertices are formed from reconstructed tracks. The primary vertex corresponds to the vertex where the pp collision took place, while secondary vertices correspond to the decay of particles.

The ID is done with different layers of detectors. When a particle interacts with one of them it deposits a part of its energy to the sensor, and this energy is being converted by the sensor readout electronics. If the signal is larger than a predefined threshold a hit is recorded. One wants to have a large number of hits in order to precisely measure the particles track. However, too much of detector material can lead to multiple scattering and conversion of photons. The material budget of the ID is shown in Figure 2.6.

The particle density is falling with the distance from the IP as $1/R^2$, thus the layers close to the IP need to have a high granularity in order to be able to distinguish between hundreds of particles from one pp collision, while the outermost layers can have a lower granularity. The ID consists of three subdetectors, listed from innermost
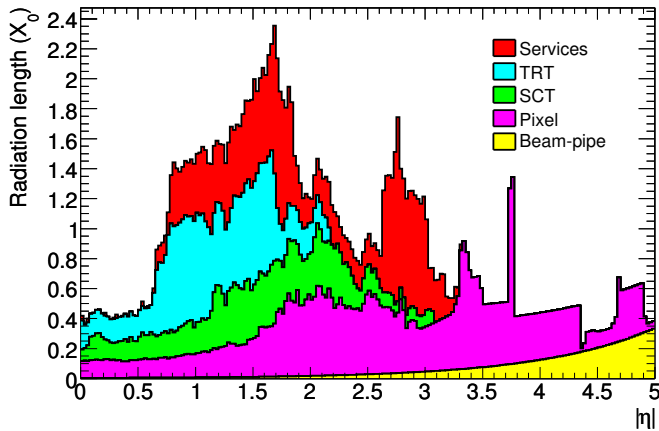
Figure 2.6.: The material budget of the ATLAS Inner Detector as a function of absolute pseudorapidity in units of radiation length X_0.
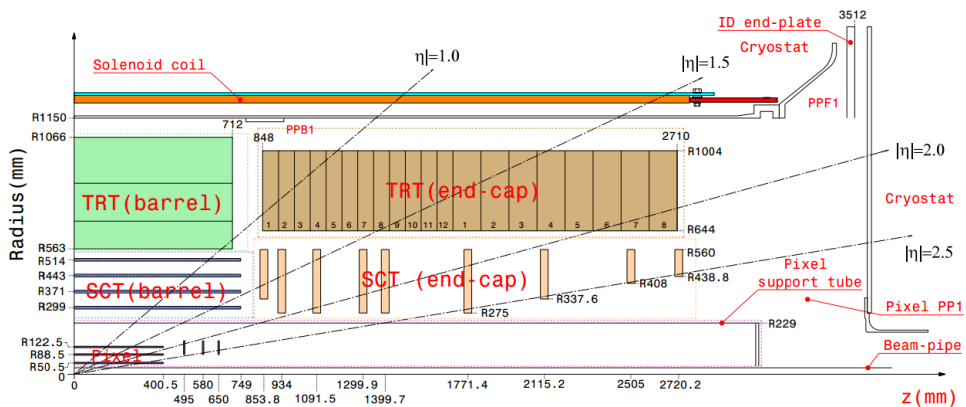
Figure 2.7.: A quarter of the Inner Detector showing the detector acceptance and the geometrical sizes of the layers.

to outermost: the high-granular silicon pixel detector, the silicon strip (SCT) detector and the transition radiation tracker (TRT).

All subdetectors consist of two barrel parts (Barrel A and Barrel C) and two end-cap parts (End-cap A and End-cap C) which are placed symmetrically with respect to the interaction point. The ID geometry and acceptance is shown in Figure 2.7.

The Pixel detector is a semiconductor detector which consists of silicon pixel sensors [26]. The detector resolution in the barrel (endcap) region is 10 μm in $R - \phi$ and 115 μm in R (z).

The SCT detector is a semiconductor microstrip detector. Each layer consists of two layers of strips rotated in 40 mrad with respect to each other. The detector resolution in the barrel (endcap) region is 17 μm in $R - \phi$ and 580 μm in z (R).

The TRT contains ~ 300000 thin-walled proportional-mode drift tubes providing on average 30 two-dimensional space points with $\sim 130 \ \mu m$ resolution for charged particle tracks with $|\eta| < 2$ and $p_T > 0.5$ GeV [27–29]. In addition to continuous tracking, the TRT provides electron identification through the detection of transition radiation X-ray photons, which are created by the charged particles passing through layers of radiator material between the tubes. A detailed description of the detector can be found in Chapter 3.

2.2.4. The calorimetry system

The ATLAS calorimeters are designed to trigger on and to measure accurately the energy and position of photons, electrons and hadrons, as well as to ensure a good missing energy measurement, which is crucial for new physics searches. The calorimeter system is divided into two main parts: an inner electromagnetic (EM) calorimeter aimed at detecting electrons and photons, and an outer hadronic calorimeter designed to detect mesons and baryons which penetrate the EM calorimeter.

The EM calorimeter covers the rapidity region $|\eta| < 3.2$. The hadronic calorimeter is divided up into a barrel hadronic calorimeter covering $|\eta| < 1.7$, an hadronic end-cap calorimeter covering $1.5 < |\eta| < 3.2$ and a forward calorimeter covering $3.1 < |\eta| < 4.9$. A global view of the ATLAS calorimeter system is illustrated in Figure 2.8.

EM calorimeter

The ATLAS EM calorimeter is a sampling calorimeter with accordion-shaped lead absorbers and kapton electrodes. Figure 2.9 shows the accordion shaped geometry of the ATLAS EM calorimeter. The accordion geometry provides a fast signal readout and an azimuthal symmetry without cracks. Liquid Argon (LAr) is used as an active
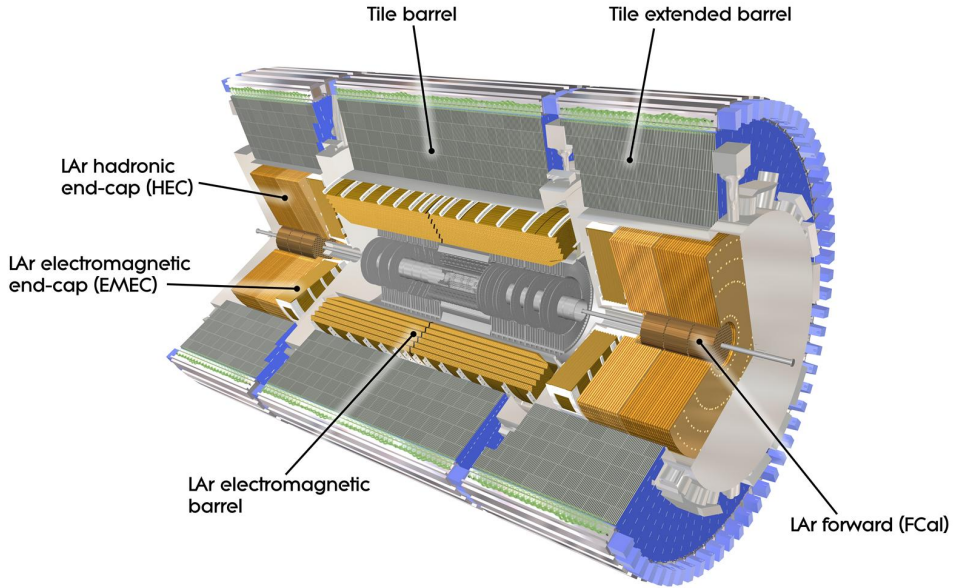
Figure 2.8.: Three-dimensional view of the ATLAS calorimetry.

material. The EM calorimeter is divided into two barrel parts ($|\eta| < 1.475$) and end-caps ($1.375 < |\eta| < 3.2$). The end-cap calorimeter on each side consists of two wheels: the Inner Wheel ($1.375 < |\eta| < 2.5$) is the closest part to the beampipe, while the Outer Wheel ($2.5 < |\eta| < 3.2$) is the part furthest from the beampipe. The amount of material in terms of number of electromagnetic radiation lengths (X_0) is shown in Figure 2.10. The thickness of the EM calorimeter is above $24X_0$ in the barrel and above $26X_0$ in the end-cap regions.

Both the barrel and the end-cap calorimeters are segmented into three longitudinal layers. The first layer has a thickness of about $6X_0$ and plays a role as a preshower. It has the finest granularity in η with a cell width of about 4 mm. The second layer has a thickness of about $18X_0$ and is designed to contain almost a full EM shower. It has the finest cell granularity in ϕ and provides the azimuth coordinate of the electromagnetic shower direction. The third layer has a two times coarser granularity and the thickness varying between $2X_0$ and $12X_0$. The read-out granularity of the LAr system and the accordion shape of the EM calorimeter are schematically illustrated in Figure 2.9.
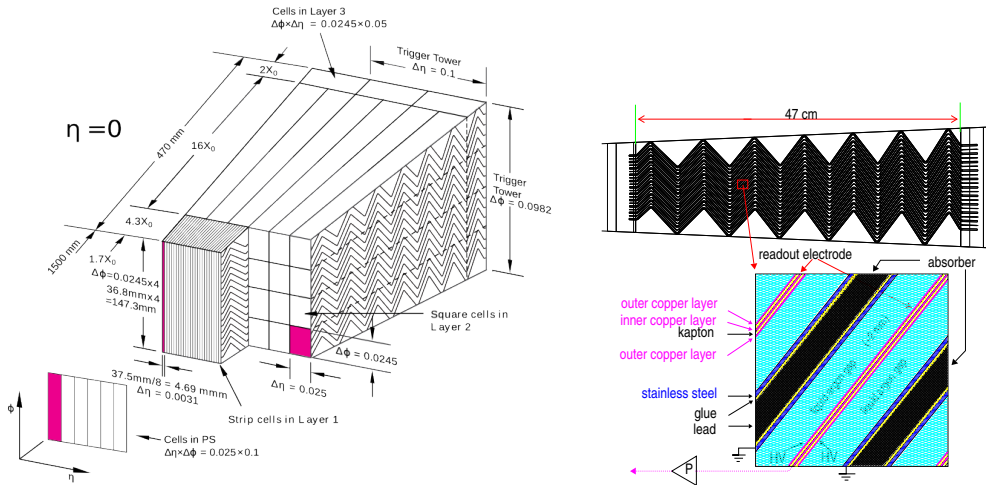
Figure 2.9.: Read-out granularity and accordion shape of the barrel EM calorimeter.
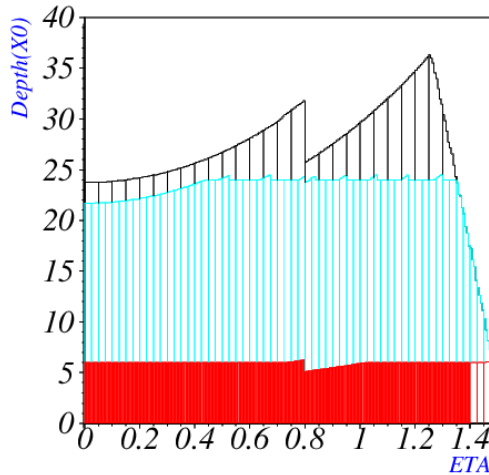
Figure 2.10.: The amount of material traversed by a particle before and in the EM calorimeter, in units of radiation lengths X_0, as a function of $|\eta|$. Different colors represent three different longitudinal layers of the EM calorimeter.

The main goal of the lead absorbers in the sampling EM calorimeter is to develop an electromagnetic shower, with a part of the EM shower detected in the LAr sensitive material. The energy deposited in the absorber material is accounted for by the known sampling fraction of the calorimeter. In order to achieve a good performance of an EM calorimeter, an important aspect is the material in front of the calorimeter as it degrades the energy resolution of the calorimeter [30]. A presampler is placed before

the ATLAS EM, calorimeter covering the pseudorapidity range of $|\eta| < 1.8$. It is needed in order to recover the energy lost in the material before the calorimeter (inner detector, cryostat, etc). The relative energy resolution for EM objects is parameterized as follows:

$$\frac{\sigma(E)}{E} = \frac{a}{\sqrt{E[GeV]}} \otimes \frac{b}{E[GeV]} \otimes c \tag{2.1}$$

where a is the sampling term which describes the statistical fluctuations of the EM shower, b is the noise term due to electronics and pile-up and c is the constant term which accounts for non-uniformity of the calorimeter response. The sampling term mostly contributes at low energies, whereas at high energies the energy resolution goes asymptotically towards the constant term, which is designed to be 0.7%. The transition region between the barrel and the end-cap, $1.37 < |\eta| < 1.52$, has a significant amount of material in front of the calorimeter (about $10X_0$), making the energy resolution there to be poor and thus it is usually excluded in physics analyses.

The drift of ionisation electrons in the LAr gap is ensured by a high voltage system which generates an electric field of about 1 kV/mm. The induced current on the electrodes is then used to reconstruct the deposited energy in an EM calorimeter cell.

The reconstruction of the electrons and photons starts by reconstructing clusters, i.e., a group of calorimeter cells containing almost the full EM shower. Clusters matched to a well-reconstructed track in the ID and originating from the interaction point (IP) are then classified as electrons. Clusters without corresponding track matching are considered as unconverted photons. If there are two tracks corresponding to the reconstructed cluster, and if a conversion vertex can be reconstructed, the cluster is classified as a converted photon.

Hadronic calorimeter

The hadronic calorimeter surrounds the EM calorimeter and is designed to detect the hadrons penetrating the EM calorimeter. It consists of a Tile calorimeter in the range of $|\eta| < 1.7$, constructed with an iron-scintillating-tiles technique, and an hadronic end-cap LAr calorimeter spanning $1.5 < |\eta| < 3.2$. The acceptance of the hadronic calorimeter is extended by the LAr Forward calorimeter up to $|\eta| < 4.9$ (see Figure 2.8). The LAr technology for large $|\eta|$ is chosen because of its intrinsic radiation hardness. The signal in the Tile calorimeter is provided by scintillating tiles as an active material,

while the absorbers are made of iron. The calorimeter is divided into a barrel and two extended barrels with the inner radius of 2.28 m and the outer radius of 4.23 m. Similarly to the EM calorimeter, the Tile calorimeter is longitudinally segmented into three layers, which are needed for triggering and reconstruction of jets. The readout of the tiles is performed by optical fibers. The tiles are grouped into readout cells, which are designed to be projective with respect to the interaction point.

The end-cap hadronic calorimeters are constructed with copper as an absorber and LAr as an active material. The absorber plates are orthogonal to the beam axis and consist of two consecutive wheels with a thickness of 25 and 50 mm. The forward calorimeter is placed at a distance of about 5 meters from the interaction point. It consists of three longitudinal sections: the first is made of copper absorbers, while the next two are made of tungsten absorbers. The forward calorimeter also provides an electron reconstruction capability.

2.2.5. Muon Spectrometer

The Muon Spectrometer (MS) is the outermost part of the ATLAS detector and is designed to trigger on and detect muons, the only charged particles that penetrate the calorimeter system, and it covers the pseudorapidity range of $|\eta| < 2.7$. It is a tracking detector which measures the muon tracks deflected in the strong magnetic field. The MS consists of one barrel ($|\eta| < 1.05$) and two end-cap sections. The system of large superconducting air-core toroid magnets provides the magnetic field of 0.5 T and 1 T in the barrel and end-cap, respectively, resulting in a bending power between 2.0 and 7.5 Tm [31]. It is equipped with three cylindrical layers of Monitored Drift Tube Chambers (MDT) and Cathode Strip Chambers (CSC) providing track measurement; three doublet layers for $|\eta| < 1.05$ of Resistive Plate Chambers (RPC) and three triplet and doublet layers for $1.0 < |\eta| < 2.4$ of Thin Gap Chambers (TGC) providing triggering and (η, ϕ) measurements of the muon track momentum. The CSC is used in the forward region instead of MDT due to the high background conditions. A combination of four complementary technologies is needed to provide a precise muon measurement over a large $\eta-$range. The layout of the muon spectrometer is shown in Figure 2.11.

The MS allows for a precise muon momentum measurement in the pseudorapidity region up to $|\eta| < 2.7$ and provides a relative resolution better than 3% over a wide
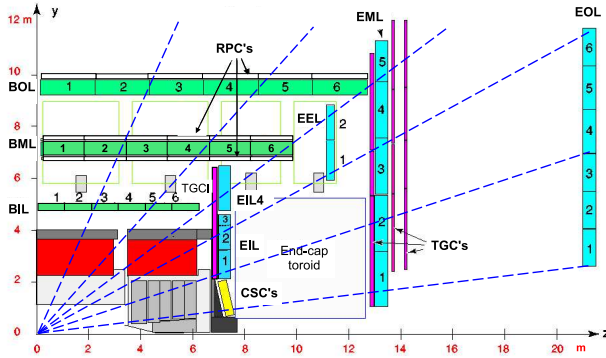
Figure 2.11.: Cut-view of one quadrant of the Muon Spectrometer.

range of p_T. It deteriorates to 10% at $p_T \sim 1$ TeV. The MDT and the CSC provide a single hit resolution in the bending plane of about 80 μm and 60 μm, respectively.

The muon track in the MS is reconstructed in two steps. In the first step the muons are triggered in the RPC/TGC and local track segments are defined in each layer of chambers. In the next step, the local track segments from different layers are combined through a χ^2-fit forming a full MS track. To reduce the probability of background tracks penetrating the calorimeter, the fitted tracks of the muon candidates are required to point towards the interaction point.

2.2.6. Trigger system

The maximal theoretically possible collision rate at the LHC is 40MHz. Since the size of one *pp* collision event recorded by the ATLAS detector is 1-2 Mbytes, there is no physical possibility to record such a huge stream of data and store it permanently. However, more than 99% of the events happening in *pp* collisions have no interest for physicists because they have been well studied previously due to their high cross section. Thus one wants to "hunt" only for events which occur very rarely. This is why non-interesting events have to be rejected by the trigger system. The ATLAS experiment has three levels of triggers: a hardware-based level 1 (L1), a software-based level 2 (L2) and the Event Filter (EF) [32]. The reduction of the rate of the accepted events for the three trigger levels is shown in Figure 2.12. The L1 trigger uses trigger chambers in the MS and the coarse-granulated calorimeter information to find high-p_T

charged leptons, photons or large missing transverse energy. The so-called regions of interest (ROI) are then formed corresponding to the (η, ϕ) phase space of the detector where large signals have been observed. These regions are used by the L2, which uses the full granularity information within a ROI. The EF takes events which passed L2 and apply the same algorithms as in the offline analysis to make a final decision to store or discard the event.

Event rate and decision stages

Rate (Hz)

Jets
b → μ
π/K → μ

W, Z

Top

H → γγ

LVL1   40 MHz

LVL2   75 kHz (100 kHz)

< 2.5 μs

average ~10 ms

Event Filter ~1 kHz

few sec

100 Hz

10^8
10^6
10^4
10^2
10^0
10^{-2}
10^{-4}

25 ns   μs   ms   sec

10^{-8} 10^{-6} 10^{-4} 10^{-2} 10^0 sec

Available processing time
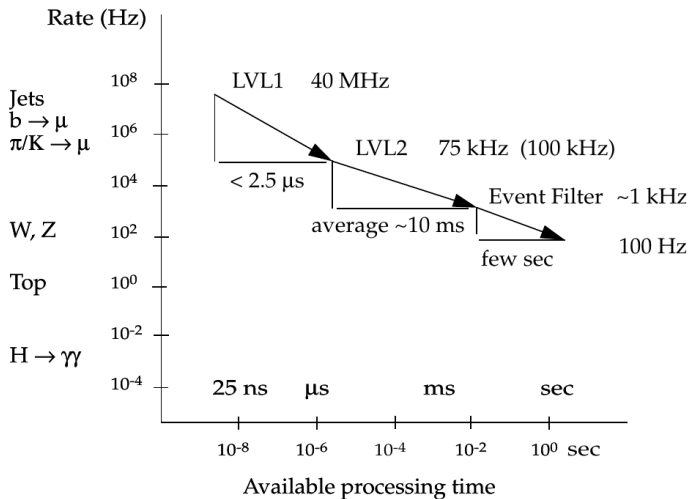
Figure 2.12.: The acceptance rate as a function of time needed to make a decision about the event by the trigger. A comparison with the rate of the SM processes occurring in the *pp* collision are shown as well [33].

In this manner, one can significantly reduce the rate and accept only events of interest. A comparison of the trigger acceptance rate with the rate of some SM processes is shown in Figure 2.12.

Chapter 3.

Simulation and performance studies of the Transition Radiation Tracker with Argon-based gas mixture

This chapter describes the performance of the ATLAS Transition Radiation Tracker (TRT) detector with an Argon-based gas mixture in some sectors of the detector. The TRT was designed for a Xenon-based mixture with carbon dioxide and Oxygen additions (in proportions 70/27/3). However, leaks in some drift tubes led to the decision to switch to a cheaper Argon-based mixture for the leaking modules. This chapter covers a description of the implementation of the Argon mixture in the TRT digitization package. The chapter consists of three sections. In Section 3.1, an overview of the detector running conditions is given. In Section 3.2, the general TRT description is presented with an emphasis on a description of the drift tubes, the gas used and the front-end electronics. Section 3.3 gives an overview of the digitization package as well as a detailed description of the Argon implementation in the code. Section 3.4 describes a performance study of the TRT regarding a hit and track parameters with a focus on the active gas mixture, and particularly the comparison of Xenon- and Argon-based mixtures. In Section 3.5, conclusion of the Argon studies is presented.

Modelling of the new Argon gas mixture and the new detector configuration (which allows to simulate the detector with different gas mixtures in different parts) were integrated into the official TRT digitization package and are currently used for the Monte Carlo simulation of the TRT detector. The previous implementation of the Xenon-filled drift tubes was used as a basis for the modelling of Argon-filled drift tubes. All Argon gas mixture properties needed for the implementation in the digitization

code were measured in the laboratory with a drift tube prototype or modelled by the Garfield package [34]. A tracking performance study was done to understand the behavior of the Argon mixture in the TRT as compared to the Xenon one.

3.1. Motivation

During LHC Run-1 the TRT detector was successfully operating and was providing an essential part the of tracking information as well as particle identification information by detecting transition radiation photons. At the end of Run-1 a few leaks in the drift tubes were observed, which triggered a large investigation in order to understand and fix the problem. After investigation of the problem during the technical LHC shutdown some of the problematic tubes were fixed, however, a large part of the leaking tubes were impossible to fix due to the lack of access to them. Therefore some changes in the gas system were done in order to minimize the leaks, and a study of the possibility of using Argon-based gas mixtures (which are significantly cheaper) started. With time, the amount of leaking gas increased, and it became inevitable to switch to the Argon mixture for the most leaking TRT modules. In Figure 3.1 the gas configurations of the TRT used in years 2015 and 2016 are shown, demonstrating that the problem was gradually increasing with time.
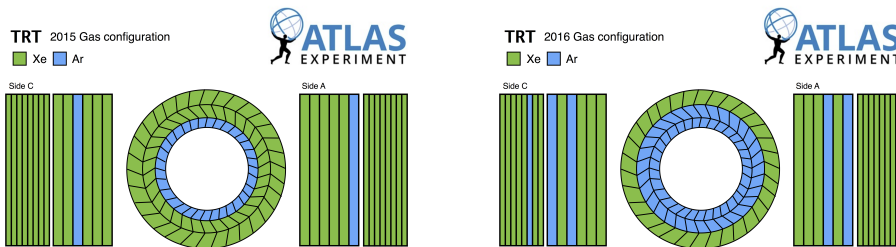
Figure 3.1.: TRT gas configurations used in 2015 (left) and 2016 (right) during physics data taking [35].

3.2. Detector design

The general description of the TRT detector has been given previously in Section 2.2.3. In this chapter the main focus will be on straw tube performance, readout electronics as well as on a short overview of the track reconstruction with the TRT.

3.2.1. The straw tube and operating gas mixture

The main elements of the TRT are proportional straw-shaped drift tubes, hereafter called straw tubes or simply straws. The tubes need to have good electrical and mechanical properties (the cathode resistance has to be as low as possible). It is important to minimize possibility of gas leaks as well as to avoid bending of the tubes, which would lead to changes in the alignment. The geometrical factor has to be taken into account as well: large straws in diameter provide a better hit efficiency, while small straws provide short drift time (the time needed to collect electrons in the straw tube), which is crucial in order to cope with a 25 ns distance between bunch crossings. Another crucial requirement is a limit on the thickness of the tubes. In order to let low-energy transition radiation photons (created mainly by electrons passing through radiators) go through and be adsorbed in the gas, straw walls need to be as thin as possible. One also wants to keep the material budget as low as possible in the ID to reduce multiple scattering, which is the main source of uncertainty of the track transverse momentum (p_T) measurement.

All these requirements were considered during the design phase, in order to get an optimal choice. The straw size is 4 mm in diameter. Walls are made from two layers of multilayer film. A section of the straw wall is shown in Figure 3.2. The multilayer film consists of a 6 μm thick carbon-polyimide layer, which protects a 0.2 μm thick Al layer, which is coated by a 25 μm Kapton film. These two films are placed back to back and are glued by a 5 μm thick polyurethane layer. Mechanically, each straw is supported by 4 carbon fiber bundles. The anode is a 30 μm diameter tungsten wire coated with a 0.6-0.7 μm layer of gold.

The active detector volume of a straw is a gas mixture which is flushed through the tubes with the help of the gas system. This mixture was carefully chosen in order to be safe to use (to prevent sparks that can perforate the walls), be compatible with the detector materials, and to not produce dissociation products after the electron
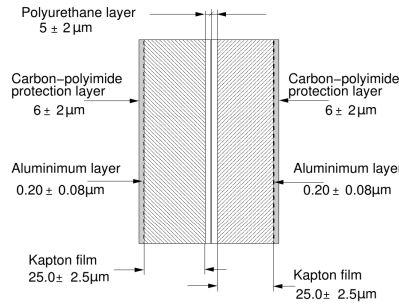
Figure 3.2.: Section of the TRT straw tube wall.

avalanche with aggressive properties that could chemically damage the straw. A high electron drift velocity is preferred, as well as a wide operating plateau (the high voltage range where straws work in the proportional regime). The latter is important in order to have a safety margin in case the high voltage has to be changed to correct for temperature variations, to enhance the signal to noise ratio or to adjust for heavy-ionizing particle effects [27]. Several noble gases were considered as a main component of the gas mixture. Because they are inert they are safe to use in the detector for a long time, and they have excellent photoadsorption cross sections. The target energy of transition radiation photons for electron identification is in the range of 1-20 keV. In Figure 3.3 the absorption lengths are shown for the four heaviest noble gases. As one can see, the best choice would be Radon, but due to its radioactivity it can not be used. The next candidate was Xenon, and it was chosen to be the main gas component. Because of the high cost of Xenon it was decided to use Argon gas for a large number of tests and during the commissioning phase before *pp* collisions. This is the reason why the read-out electronics was designed with a possibility to work with both Argon-and Xenon-based gas mixtures, as described in Section 3.2.2.

In order to have a well controlled electron avalanches in the straw, one has to add another gas component, a quencher. The main purpose of the quencher is to absorb UV photons created in the avalanche process and to prevent secondary avalanches, which can lead to an early breakdown. After a dedicated study, reported in [27], it was decided to use carbon dioxide as a quencher due to its suitability and well known properties. In order to increase the width of the operating plateau even more, a third gas component, Oxygen, was added. By itself O_2 does not interact with UV photons, but ozone (O_3), which is created in the electron avalanches, does. However, O_2 is a strongly electronegative gas, which can negatively affect straw performance
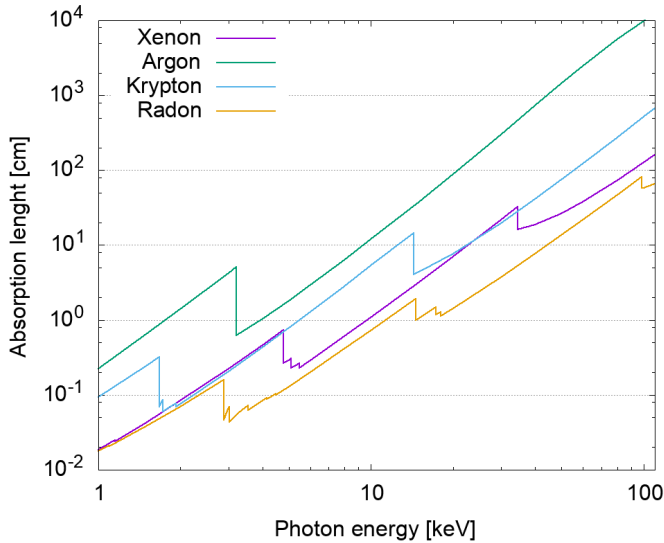
Figure 3.3.: Absorption length as a function of photon energy for the heaviest noble gases. The plot is based on data reported in [36].

by capturing drifting primary electrons, as described below, and therefore only a few percent of it can be used in the mixture.

The final choice of the gas mixture to be used in the TRT was decided to be 70% of Xenon, 27 % of carbon dioxide and 3% of Oxygen. When some straws started to leak, it was decided to switch the main gas component from Xenon to Argon for these straws, due to economic reasons. Argon has significantly higher absorption length with respect to Xenon, as can be seen in Figure 3.3 (approximately an order of magnitude difference), therefore straws with Argon almost completely lose the ability to detect transition radiation, which means losing the particle identification capability.

The operating gas gain for the straws was chosen to be $2.5 \cdot 10^4$ [37] and it had to be the same for all straws. It corresponds to 1530 V for the Xenon mixture, as shown in Figure 3.4. The gas gain curve for the Argon mixture is significantly different, and to reach the same gain only a voltage of 1420 V had to be applied.
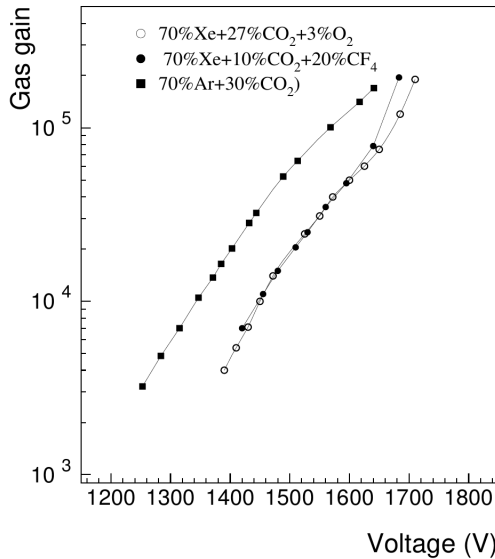
Figure 3.4.: Straw gas gain as a function of high voltage for different gas mixtures [27].

3.2.2. Front-end electronics and signal processing

The main purpose of the TRT is to provide hits for track reconstruction and information for electron identification by detecting transition radiation photons. In order to get the best possible position resolution of hits one needs not only to have a possibility to identify which straws particle traversed, but also to measure the closest approach of the charged particle to the straw wire, the so-called track to wire distance. For this purpose, the drift time of electron clusters has to be measured. The TRT front-end electronics was designed to perform these precise time measurements. One has to measure the time of signal arrival (drift time of the electron clusters to the anode wire) and the duration of the signal, the so-called Time over Threshold (ToT). Time over Threshold is needed to distinguish signals from particles originating from different bunch crossings and can be used for particle identification because it characterizes the amount of the ionization in the straw gas. Typical time needed for electrons to drift from the straw wall to the anode wire in the Xenon-based gas mixture corresponds to 40-45 ns, which dictates the size of the read-out window to be 3 BCID or 75 ns. As shown in Figure 3.5, the signal is sampled with 24 bits (3.125 ns each). A value of 1 is assigned to a bit if the signal amplitude is higher than the predefined threshold, otherwise a value of 0 is assigned. The first transition in the bit pattern from 0 to 1

corresponds to the so-called leading edge of the signal and the transition from 1 to 0 corresponds to the trailing edge of the signal. Their difference is equal to the Time over Threshold of the signal.
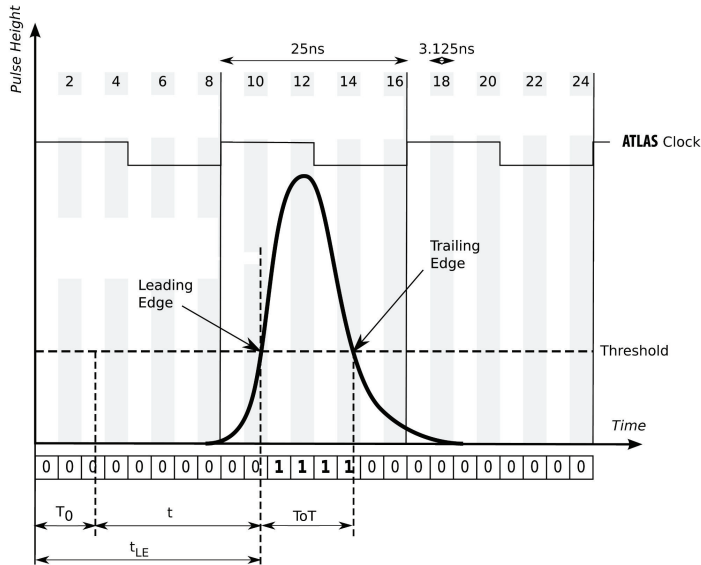
Figure 3.5.: Illustration of the digitization of the straw signal.

A typical signal from the straw consists of two components, as shown in Figure 3.6: a sharp peak, which corresponds to the fast electron drift, and a slowly falling ion tail, which corresponds to the gas ions created in the avalanche process. Only the electron peak contains information of interest (the drift time of the primary electron clusters), thus the ion tail is canceled out by adding a mirror image pulse to the signal.

The ion tail cancellation and signal digitization is done by a custom-made ASDBLR (Amplification, Shaping, Discrimination and Base-Line Restoration) chip. This chip also performs restoration of the signal baseline and discrimination. Electronics make discrimination with two different thresholds. One threshold, the so-called Low Threshold (LT), is used to trigger on cases when a high-energetic particle passes through the straw and ionizes the gas along its path, and it is shown in Figure 3.5. The second threshold, the so-called High Threshold (HT), is used for the case of transition radiation photon detection. Contrary to the high-energetic particles, transition radiation photons deposit all their energy essentially in one point when interacting with gas. This corresponds to a large number of primary electrons, which leads to a large read-
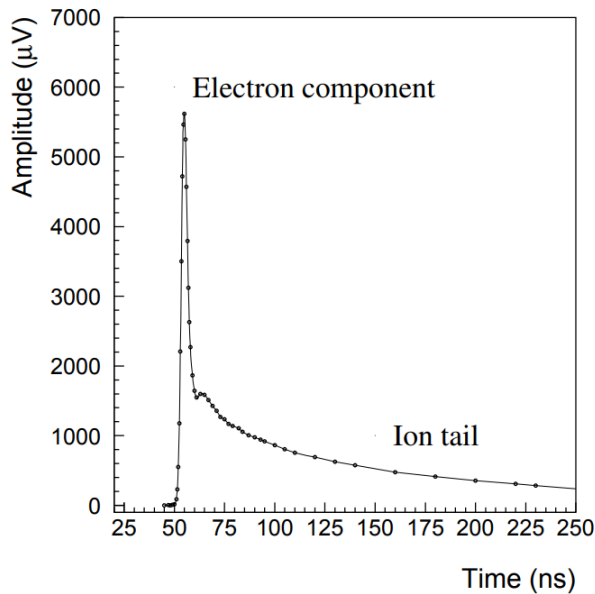
Figure 3.6.: Typical signal from the TRT straw [38]. The sharp peak corresponds to the fast electron drift component. The following tail is caused by slow drift of ions in the gas.

out signal. Threshold values used for the Xenon-based gas mixture correspond to 300 eV and 6 keV for LT and HT respectively. Discrimination with HT is done per BCID.

In total, the ASDBLR chip provides 24+3 bits, which corresponds to 24 LT bits and 3 HT bits over the 75 ns read-out window. A schematic illustration of the ASDBLR chip operation principle is shown in Figure 3.7. ASDBLRs are placed close to the straws in order to reduce noise in the signal. One chip reads eight straws. The next component in the read-out chain is a complementary read-out chip DTMROC (Drift Time Measurements Read-Out Chip), which accepts information from two ASDBLRs and holds data in the pipeline until the first level trigger arrives. The overall TRT read-out chain is shown in Figure 3.8. The detailed description of the TRT electronics is reported in [39].

3.2.3. Tracking with the TRT

The track reconstruction algorithm requires a set of spatial hits and the corresponding error matrices in order to build a track. The TRT electronics provide drift time
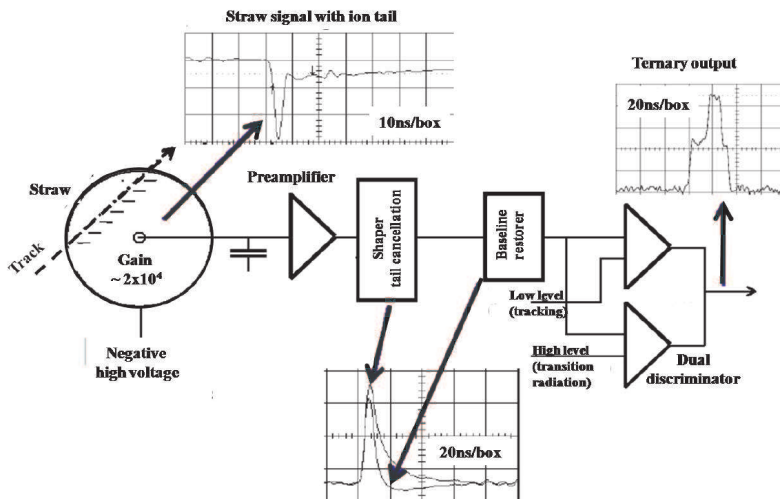
Figure 3.7.: Schematic illustration of the straw signal digitization by the ASDBLR chip [40].
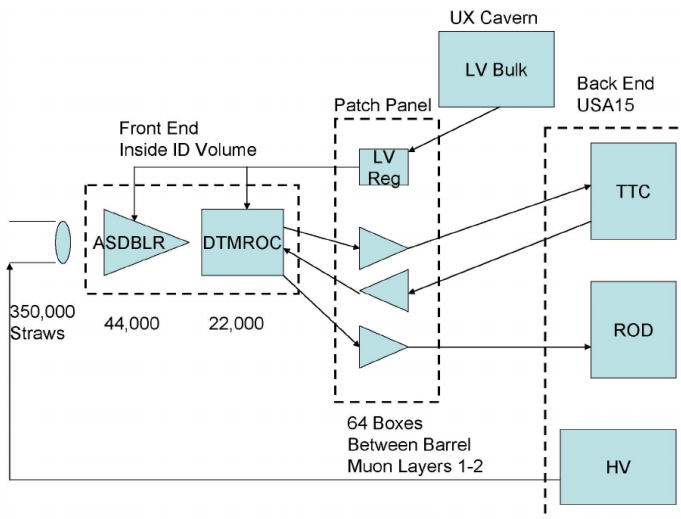
Figure 3.8.: Schematic representation of the TRT read-out electronic [39].

measurements which can be transformed to the drift radius (drift distance of the electron cluster which reached the anode wire first), which can then be used in the track reconstruction.

The first task therefore is to properly measure the drift time of the electrons to the anode wire. The measured leading edge time has two components: the actual

drift time t and the calibration constant T_0, as illustrated in Figure 3.5. The calibration constant T_0 has three parts:

- The collision time with respect to the ATLAS clock, since there could be some uncompensated delays due to propagation in the wires and electronics.

- The time of flight of the particle to the straw. Straws are placed at a distance varying from 0.5 to 2.6 meters from the interaction point, which corresponds to up to 9 ns for a relativistic particle to reach the furthest straws.

- Time of the signal propagation in the wire to the front-end electronics, typically a few nanoseconds.

The calibration constant T_0 is obtained for each DTMROC from the calibration procedure which is done after each run. The next task is to transform the drift time to a drift radius. It is done with the help of the so-called $r - t$ relation which gives the drift radius as a function of the drift time. This relation is determined from data and is fitted by a third degree polynomial, which is used for calculations of the drift radius itself. More details on the $r - t$ relation are given in Section 3.3.5. The last missing parameter, the hit measurement error, is also calculated in the special calibration procedure. A detailed description of the calibration procedure can be found in [41].

The main tracking algorithms used in ATLAS are the global χ^2 fit, when tracks are fitted by minimization of the χ^2 value, and Kalman filter which makes pattern recognition layer by layer. When a track is fitted, all the used hits in the fit are removed from the list of available hits, and the tracking algorithm is executed iteratively until all tracks are reconstructed. In Figure 3.9, a schematic representation of a track passing two straws is shown. The drift radius obtained from the drift time with the $r - t$ relation is shown with a dashed line around the wire. The track to wire distance is the distance of the closest approach of the track to the anode wire (r_{track}). The difference between the drift radius and the track to wire distance is called the position residual. By calculating position residuals for each hit and for all tracks in the barrel or end-cap parts of the detector and by measuring the width of the residual distribution one can estimate the resolution of the detector. In the same manner, the time residuals can be measured, which are equal to the difference between the drift time and the track time, which are obtained by using r_{track} and the inverse of the $r - t$ relation.

There are two types of TRT hits: precision hits and tube hits. Precision hits are the hits described above. Tube hits are hits where the drift time information is not used,
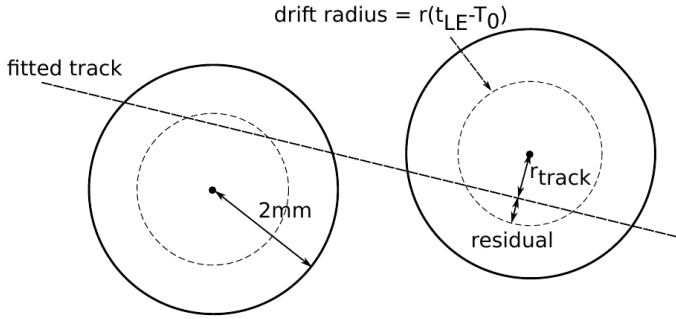
Figure 3.9.: Illustration of the main hit parameters such as drift radius, track to wire distance (r_{track}) and position residual.

only the fact that there is a hit in the straw. For such hits, the drift radius is assigned to be 0 mm, and the hit error is $\frac{d}{\sqrt{12}}$, where d is a diameter of the straw (4 mm). Tube hits have a difference between track and drift radius larger than 2.5 times the uncertainty of the drift radius. Since the track fitting is done iteratively, some hits can go back and forth from being tube or precision hits.

The main TRT detector contribution to the tracking is an improvement of the momentum resolution of tracks measured with the Inner Detector. The large number of hits in the TRT provides a solid handle to measure the track curvature, which translates into a track momentum measurement. Momentum resolution can be expressed by the following formula [42, 43]:

$$\frac{\delta p_T}{p_T^2} = \frac{\sqrt{([c^2])}}{0.3B}$$ (3.1)

where p_T is the transverse momentum of the track, δp_T is its error, and $[c^2]$ is the variance of the track curvature, which can be expressed as [42]:

$$[c^2] = \frac{\sigma^2}{L^4} \frac{720N^3}{(N-1)(N+1)(N+2)(N+3)}$$ (3.2)

where σ is the spatial resolution of the hit, B is the magnetic field and L is the length of the measured track. As can be seen from the formula above, the momentum resolution is proportional to the spatial resolution of the hits and is inversely proportional to the

square root of the number of hits. Therefore spatial resolution and the number of hits are the parameters of interest during the tracking performance studies.

The importance of the TRT for the momentum resolution can be seen in Figure 3.10. This plot shows the momentum resolution of cosmic rays data collected in 2008, for Inner Detector tracks reconstructed with and without the TRT. A clear and significant improvement can be seen, especially in the high momentum region.
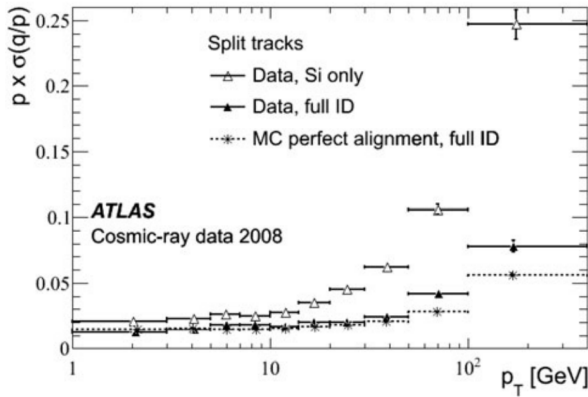
Figure 3.10.: Momentum resolution determined from cosmic rays data, taken in 2008, as a function of transverse momentum [44]. The resolution is shown for simulated full ID tracks (stars), full ID tracks (solid triangles) and silicon-only tracks (open triangles).

3.3. Modelling of the new Argon-based gas mixture in the TRT

In this section, the description of the digitization code will be presented, with a detailed explanation of the implementation of the Argon-based gas mixture. The main task of the digitization code is to simulate the number and properties of the primary electron clusters as well as their drift in the gas to the anode wire. The response of the front-end electronics which provides the final digitized timing information is simulated as well.

3.3.1. Monte Carlo simulation of the ATLAS detector

Before going into the detailed description of the TRT detector modelling, it is important to summarize the general approach used in ATLAS for detector modelling.

To have the possibility to reconstruct any physics process which happens in high energy particle collisions, or to measure a corresponding physics parameter of a process, one has to have a clear picture of the response from each detector sub-system. Besides the understanding of the real detector performance, it is equally important to have a simulation of the detector which one can trust. A simulation of the detector response allows one to perform many sophisticated studies, such as a study of the detector effects and systematic uncertainties, distinguishing background processes from specific processes of interest or even to make a prediction for the possibility to "see" a signal from a hypothetical model with a given amount of data. A lot of effort was spent to develop and validate the detector simulation software. In ATLAS, the simulation of the detector response is done in a few well-defined steps, which are:

- Event generation. In this step, the physics process of interest is modelled. The outcome of this step is a list of final state particles characterized by their 4-momenta. This is done by specialized Monte Carlo generators. This step involves many calculations and modelling, such as calculation of the matrix elements of hard processes, modelling of the initial- and final-state radiation of incoming/outcoming partons, creation of the colorless hadrons from the quarks and non-stable particle decays, etc. Typical MC generators used in ATLAS are PYTHIA [45], HERWIG [46], SHERPA [47] and others.

- Simulation. Particles created in the collisions traverse the detector and interact with the detector material. These interactions are simulated by software package, which define trajectories of particles and the energy depositions in all sub-detectors. In ATLAS it is done using the GEANT4 [48] package, which returns a list of hits, the so-called simulation hits, or simply "simhits", which contain position and timing information of the interaction together with the amount of energy lost by the particle due to the interactions (deposited in the detector material).

- Digitization. Energy depositions in the detector create analog signals which are read and processed by the read-out electronics. During the digitization step, the behavior of the front-end electronics is simulated together with the signal

processing, in order to simulate the same outputs (measured quantities) as the real electronics provide (e.g. hits in the pixel or strip, digitized current from the PMT or calorimeter cell, etc.). Due to the different designs of the electronics for different sub-detectors, the digitization software is different for each sub-detector. Such software is written and maintained by each sub-detector community separately.

- Reconstruction. The final step is to collect all information from all sub-detectors, apply all the needed calibration and alignment corrections and reconstruct physics objects. This step is identical to the one applied to the real data, only that the above mentioned corrections can be different for simulated and real data, e.g. some timing shifts in the electronics can not be simulated because they do not play any role, which means that the timing corrections of the calibrated constants will be different for simulation and real data.

A more detailed description of the ATLAS detector simulation can be found in Ref. [49].

3.3.2. Simulation and digitization of the Argon gas mixture in the TRT

The geometry of the TRT is described in the ATLAS simulation package and during the simulation step it is used to simulate particle interactions with the detector material. However, because the GEANT4 package does not provide precise enough calculations of energy deposition in thin layers of gas in tubes (which is described in the following Section 3.3.4), it was decided to take care of this simulation during the digitization step in the digitization package. Thus in the simulation step, only the list of hits in the TRT is used when calculating energy depositions in the gas inside the tubes during the digitization step.

The digitization package also covers the simulation of the following properties:

- The number of the primary ionization clusters along the particle path and the number of electrons in these clusters

- The drift time of the electrons to the anode wire, taking into account the magnetic flux density and drift diffusion

- The probability of electron recapture by the Oxygen molecules

- The signal shaping and discrimination by the front-end electronics

- The detector white noise

All these parameters depend on the type and the proportion of the components used in the gas mixture. To implement the new Argon gas mixture into the digitization package, all these properties were considered in detail to ensure that a proper implementation of all of them is done.

3.3.3. Implementation of the mixed gas TRT configuration

Before describing the details of the Argon mixture simulation and digitization, one has to briefly explain how the digitization code works and how the Argon option was embedded in the code. All tubes in the code inherit a geometry of the "ideal" tube, defined during the design phase. However, each tube has some unique characteristics. It has a unique position, which is linked to the value of the magnetic field in the straw. It can even be dead, which means that the straw will be skipped in the digitization. When GEANT4 propagates particles, it simulates their interactions with matter in order to obtain an array of simulation hits. In each hit an energy deposition in the detector material takes place. The digitization code takes the list of simulated hits and loops over all of them for each track. If a particles hits a TRT straw, the processing of the straw begins. The first step is to check if the straw is dead or not by accessing the information from the straw database. If it is not dead, a drift time simulation is done. The Argon implementation was done by assigning each straw additional characteristics, such as the type of gas mixture used. This information is also stored in the straw status database. Then the simulation of the parameters described above is done accordingly to the type of gas mixture. It is worth mentioning that such an approach allows to simulate the detector with mixed gas configurations, i.e., when some parts of the detector are operated with Xenon, and other parts – with Argon mixtures.

3.3.4. Simulation of the energy deposited in the gas and the initial number of electrons in a cluster

During the development phase of the TRT simulation and digitization software, it was found that the GEANT4 simulation does not provide accurate enough description of

the physics of a charged particle passing through the very thin gas layers (straws). In [50] the author made a comparison of the photoabsorption cross section parameterization used in GEANT4 with the another one more detailed. Even though the difference between these two parameterizations was small, using them in the code led to a 7% difference in the mean free path length, which is significant for the TRT straw simulation. That is why a dedicated model, the so-called photoabsorption ionization (PAI) model [51], is now used to simulate deposited energy in the straw. This model derives ionization cross section for a charged particle with a given gamma factor numerically from the tabulated values of photoabsorption cross section for the gas. The missing piece for the Argon-based gas mixture simulation was the lack of the photoabsorption cross section for Argon itself in the code. Cross section as a function of photon energy reported in [52] was therefore taken and implemented in the code.

As described previously, propagation of a charged particle through the ATLAS detector is done by GEANT4, and in practice, it corresponds to the list of simulated hits in the detector. These hits are used as a reference, while the real ionization clusters are calculated by the PAI tool along the "simhits" path. The PAI tool calculates the mean free path, which is the distance between two neighbor electron clusters in the gas, and energy deposited in the cluster. The mean free paths for Xenon- and Argon-based gas mixtures, calculated by the PAI tool, are shown in Figure 3.11 as a function of the scaled kinetic energy (the kinetic energy of a particle scaled by the factor $\frac{m_{proton}}{m_{particle}}$). As one can see, the mean free path for the Argon mixture is approximately 1.5 times longer than the one in the Xenon mixture. The mean free path for a highly energetic pion is 150-160 μm in the Xenon mixture. If a pion penetrates a straw centrally close to the anode (i.e. will travel 4 mm in the gas), then 25-27 primary clusters will appear. However, if it will travel 2 mm in the gas, the number of clusters will be only 12-14, and a part of them will not reach the anode due to recapture in the Oxygen. That is why measurements of the time of when the first cluster arrived to the anode will not directly correspond to the measurement of the distance of the closest approach between the wire and the track, which can be seen in Figure 3.12. This effect is directly linked to the spatial resolution of the hit. For the Argon mixture, the number of clusters will be even smaller (8-9 clusters created by a particle traveling 2 mm in the mixture), which leads to an even worse spatial hit resolution in the Argon mixture comparing to the Xenon one.

When a charged particle traverses the active gas volume of the straw, it interacts with gas molecules. It can either ionize them by kicking out an electron or excite them.
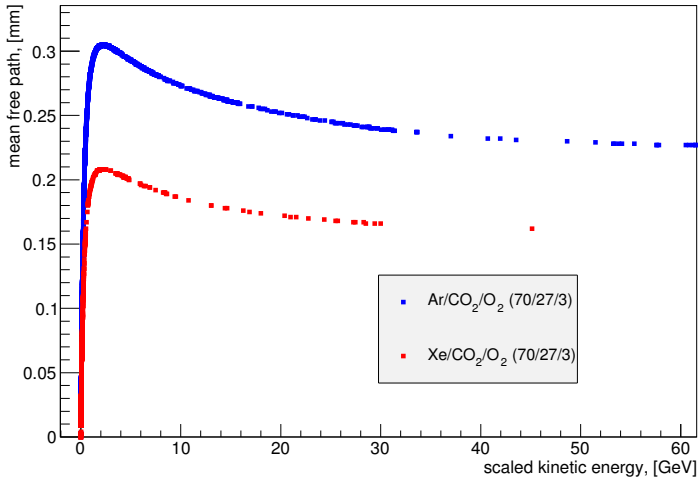
Figure 3.11.: Mean free path of a relativistic muon as a function of scaled kinetic energy $\left(E_{kin}\frac{m_{proton}}{m_{particle}}\right)$ for Xenon- and Argon-based gas mixtures.

The energy needed to kick out the least bound shell electron for TRT gasses lays in the range of 10-20 eV, but a part of the energy goes to the excitation of gas molecules, which is why the average energy needed to create an ion pair (the so-called W-value) is higher than the energy required to kick out an electron from a shell. The list of these values for all gasses used in the TRT is shown in Table 3.1. Using the values from the table and knowing the gas mixture proportions (70/27/3 %) one can estimate the average energy for a Xenon-based mixture, which is equal to 25.3 eV.

The W-value for an Argon-based mixture was calculated in the same manner and is equal to 28.3 eV, which is implemented in the digitization code. The number of primary electrons, $N_{prim.electrons}$, is calculated by the formula:

$$N_{prim.electrons} = floor\left[\frac{E_{deposited}}{W} + 1\right] \tag{3.3}$$

where $E_{deposited}$ is the energy deposited in the gas, W is the average ionization energy described above, and $floor$ is a function which returns the largest integer which does not exceed the argument of the function. From this formula, one can conclude that the number of primary electrons in clusters in the Argon-based mixture is smaller than in a Xenon-based one, assuming the same amount of deposited energy.

Gas	W [eV / ion pair]
Xe	22.1 ± 0.1
Ar	26.4 ± 0.5
CO_2	33.0 ± 0.7
O_2	30.8 ± 0.4

Table 3.1.: The average W-value for electrons and photons in different gases considered for the TRT [53].

3.3.5. Electron drift velocity and $r - t$ relation

A very crucial part of the digitization is to model the drift time of the primary electrons to the anode wire, because the drift time is directly related to the drift radius which gives the position of the hit with respect to the straw wire. During the drift in a tube, the electron interacts with gas molecules but continues its path to the wire due to the presence of the electric field. In Figure 3.12 (left) an example of drift trajectories of electrons in a straw without magnetic field is shown. Simulation of the drift of all electrons created in the gas in all tubes of the detector is computationally very heavy, moreover, besides the drift in the gas one has to simulate the creation of the avalanches with a proper simulation of all the secondary effects, such as the creation of the UV photons etc. However, if one assumes that all tubes are kept in the same condition (constant gas gain) during the detector operation, it would be possible to use tabulated average values of the drift time calculated by the Garfield package (and cross checked in the laboratory) to simulate it. This is the approach used by the TRT community.

In Figure 3.13 (left) the drift distance as a function of the drift radius obtained with the Garfield package for a case without magnetic field is shown. It was obtained by making a scan of drift distances (in the range from 0 to 2 mm) and simulating the time it takes for the first electron to reach the anode wire. The relation shown is called the $r - t$ relation and is used in the code to translate the drift distance to the drift time. In Figure 3.12 (right) drift trajectories of a cluster in the presence of a magnetic field are shown. One can see that the magnetic field significantly affects electron drift trajectories and makes the drift time longer. The $r - t$ relation for the case of a 2T magnetic field is shown in Figure 3.13 (right) and it is clearly seen that the drift time is longer in this case. However, the magnetic field is not homogeneous within the detector. The inhomogeneity effect was studied before (for example in [54]) and it was found that the drift time dependence on the magnetic field can be described by a
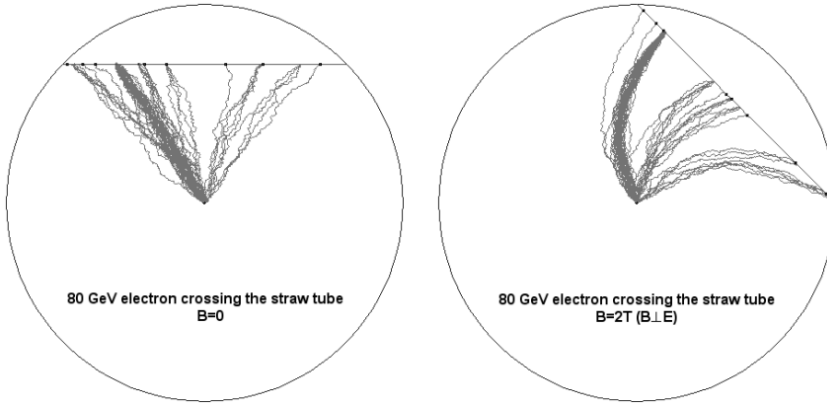
Figure 3.12.: Drift of primary electron clusters in a straw tube without (left) and with (right) a magnetic field [53].

second-degree polynomial. To get the $r - t$ relation for a specific value of the magnetic field, B_{eff}, the following interpolation formula is used:

$$RT(B_{eff}) = (RT_{MAX} - RT_{WO}) \cdot \frac{B_{eff}^2}{B_{max}^2} + RT_{WO} \qquad (3.4)$$

where RT_{MAX} corresponds to the $r - t$ relation for the magnetic field B_{max} (which is equal to 2T – the maximum magnetic field in ATLAS) and RT_{WO} is the $r - t$ relation for the case without magnetic field.

For the Argon gas mixture, two such $r - t$ relation tables were added to the TRT digitization package. In the early development stage a Xenon gas $r - t$ relations scaled by the ratio of the average drift velocities in Argon and Xenon were used in the code (gray points in the Figure 3.13). Comparison of the scaled Xenon and Argon curves demonstrates the difference of the shape of the distributions for Argon and Xenon gasses (see Figure 3.13).

Movement of the electrons in the gas contains a stochastic component due to collisions with gas atoms. This means that the drift time can differ for clusters that drift the same distance. The spread of the drift time as a function of the drift distance is shown in Figure 3.14. Black points correspond to the drift time spread obtained with the Garfield simulation for the Argon gas mixture. In the digitization code, the spread is parameterized by a 4-th order polynomial in order to preserve consistency
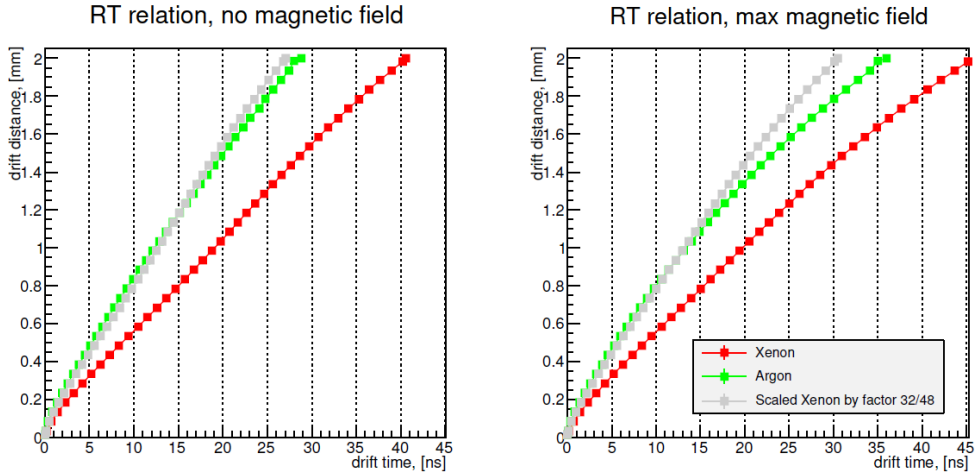
Figure 3.13.: r-t relation for the Xenon- (red) and Argon-based (green) gas mixtures. The curve for the Argon-based mixture was obtained from the Garfield simulation. A scaled (by the ratio of the average drift velocities in the Argon and Xenon mixtures) r-t relation of the Xenon-based mixture is shown in gray and was used in the initial studies of the Argon mixture.

(the spread of the drift time is shown with red and green points in Figure 3.14 for Xenon and Argon accordingly).
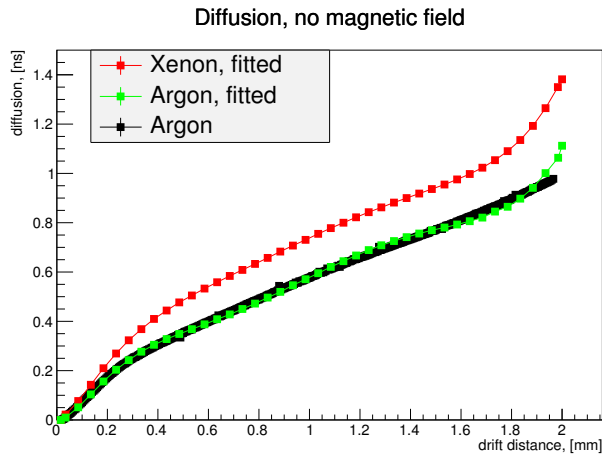
Figure 3.14.: Electron drift-diffusion in Xenon- (red) and Argon-based (green) gas mixtures as modelled in the digitization package (with a 4-th degree polynomial). Black points correspond to the Garfield simulation for the an Argon-based gas mixture.

3.3.6. Electron attachment processes in Oxygen

When electrons drift towards the anode, there is a probability that they will be captured by the Oxygen molecules in reactions: $O_2 + e^- \rightarrow O_2^-$ or $O_2 + e^- \rightarrow O + O^-$. To take into account this effect, a special study was done, reported in [54]. It was found that the electron capture probability strongly depends on the distance from the primary electron to the anode. A Garfield simulation shows that this dependence can be parameterized with a 4-th order polynomial (see Figure 3.15), which was implemented in the TRT digitization package. Because the Argon-based mixture contains the same amount of Oxygen, the same survival probability curve was used for it as well. However, a separate implementation for the Argon case was done in the code to allow for future tuning of this effect separately for Xenon and Argon gas mixtures in a case when other concentrations of Oxygen will be used.

As described previously, Oxygen was added to the mixture to increase the operating plateau of the straw, but there is another effect which it also takes care of. Drifting ions might free electrons when they reach the cathode, which in turn can produce electron avalanches, and this is not a desirable effect. As can be seen from Figure 3.15, Oxygen addition to the gas mixture provides approximately a 65% probability that these electrons will be recaptured and will never reach the anode.
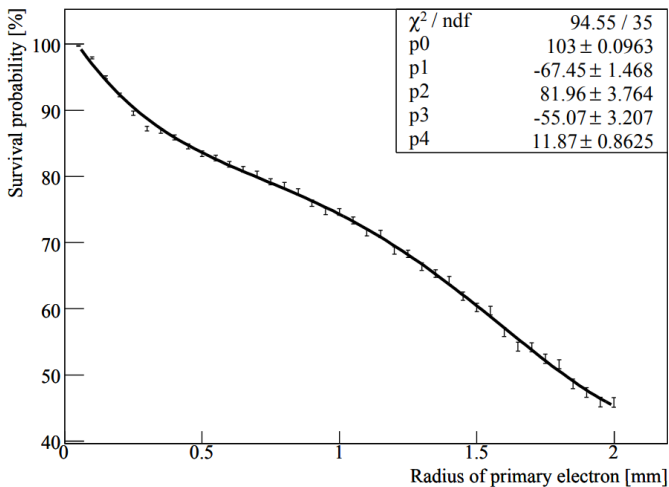
Figure 3.15.: Survival probability of the primary electron to reach the anode [54].

3.3.7. Signal shaping and discrimination

The TRT front-end electronics shape the signal before discriminating it by making a convolution of it with a special shaping function. These functions for Argon- and Xenon- based mixtures are different and one has to simulate them in order to simulate the proper response in the electronics. This was another missing piece which had to be implemented for the Argon mixture. The drift velocity in the Argon mixture is significantly larger than for Xenon. Thus the straw signal will differ significantly as well. Argon gas was used for tests and commissioning phases, and this is why a compatibility with the Argon mixture was foreseen for the ASDBLR chip. It contains a set of four shaping functions (which can be selected by a pin on the board itself): two for Xenon and two for Argon mixtures. Two sets of functions are needed for each gas because different shaping functions are used for discrimination of LT and HT. Shaping function for Argon, measured in the lab using a prototype of the ASDBLR chip, is shown in Figure 3.16 together with Xenon functions. The shown Argon functions were implemented in the digitization package for the Argon mixture simulation. In the code, the shaping function is convoluted with energy deposits, which are stored in a vector of time bins.
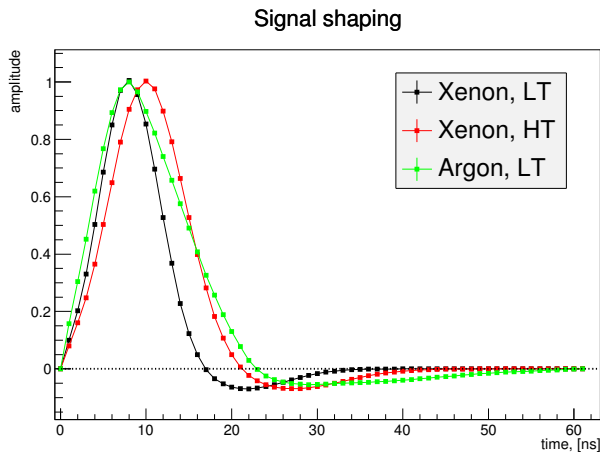
Figure 3.16.: Argon low threshold shaping function compared to the Xenon low and high threshold shaping functions.

After a convolution with a shaping function, the signal is discriminated against LT and HT, and a 24+3 bit pattern is formed. Straws with Xenon and Argon mixture should obviously have different threshold settings. As was described previously, the

Argon-based mixture has a significantly smaller signal, due to a lower number of primary electron clusters and a lower number of electrons in these clusters. When some parts of the detector work with Argon, and the others with Xenon, their performance must be kept on the same level for proper operation. In practice, this means that the hit efficiency (probability that there will be a hit if a particle traverses a straw) has to be similar for the two mixtures. To get a similar hit efficiency, the low threshold for Argon has to be lower than for Xenon. Moreover, the threshold can have different values for the barrel and end-cap parts. This is because the end-cap straws are positioned perpendicular to the barrel straws, which changes the behavior of the drifting electrons in the tubes due to the different orientation of the magnetic field. The possibility to set separate thresholds for Argon tubes was implemented in the code. After preliminary studies in the laboratory, it was found that the low threshold for Argon had to be around 100 eV, while for Xenon straws it was 285 eV for the Barrel and 300 eV for the end-cap detectors. The 100 eV value was used in the code. The low threshold values are the main parameters of interest for the Monte Carlo simulation tuning.

3.3.8. White noise modelling

During the test beam studies in 2004 [55], many sources of the TRT noise were observed. It was found that most noise sources do not affect the operation of the detector significantly, and there is no need to model them in the simulation software. An example can be a track-induced noise, when e.g. a transition radiation photon, created by an electron, can be detected by a neighbor straw which is close but doesn't belong to the track, or the appearance of a spontaneous electron cluster in the gas due to radioactive decay of unstable nuclei in the gas. However, it was decided to model the so-called white noise, which consists of high-frequency uncorrelated small fluctuations of a Gaussian nature which can pile up high enough to reach a threshold. This kind of noise can appear for many reasons, for example from the thermal noise of capacitors in the front-end electronics or noise from the anode wire. A noise model was developed by the TRT community to reproduce noise levels in the detector. The model does not explain the reasons for the noise, but numerically describes noise levels based on a few simple assumptions. Some of these assumptions are:

- The noise amplitude depends on the length of the wire.

- Every straw in the simulation has an "ideal" design shape, though in the real detector every straw is slightly different due to bending of the wire, fluctuation of the gas density and temperature, the anode being connected to different power supplies, etc. The model does not simulate the conditions of each wire since it is not practical. Instead, for every straw, its own value of the low threshold is assigned, which can fluctuate.

- The model aims to reproduce noise conditions of the detector, which means that the conditions have to be known and be used as input for the model.

- The model is universal, and it can work for any multi-channel detector with threshold discrimination.

The full description of the model is given in [50]. Below, only information related to the noise modelling in the straws with Argon gas will be discussed.

A noise amplitude is, according to the model, equal to:

$$\mathcal{A}_i = r_i \cdot \frac{\langle LT \rangle}{\langle f_i \cdot r_i \rangle} \tag{3.5}$$

where r_i is a parameter which depends on the length of the straw and is modelled with a Gaussian with a mean $\mu_i = c_1 l + c_2$, where l is the length of the wire in the straw and c_1 and c_2 are empirical parameters. The Gaussian width is equal to $\sigma_i = \omega \mu_i$, where ω is a free parameter which characterizes the relative channel-to-channel spread in noise amplitudes. $\langle LT \rangle$ is the average of the low thresholds for all tubes. In practice, this value is equal to low thresholds of "ideal" straws implemented in the code. f_i is a noise level of the i'th straw. This value is generated based on the distribution of straw noise levels measured in test beam studies in 2004 (the distribution is reported in [50]). Test beam studies were done with a Xenon-based gas mixture.

Since the low threshold is significantly different for Xenon and Argon straws and because the model is universal (can be applied to any number of straws), simulation of noise in Argon and Xenon straws is done separately. This means that the values $\langle LT \rangle$ in equation (3.5) are different and equal to the low thresholds of Argon and Xenon straws implemented in the code. All other parameters are identical for Argon and Xenon straws. It is important to mention that the noise distribution, which is used as input for the model and was measured in the test beam with Xenon straws, is utilized for the Argon straw noise modelling as well in the initial code implementation [56]. The noise distribution has to be properly measured and tuned for the Argon straws,

which was not a part of the current studies and is a topic for further Argon mixture fine tuning.

3.4. TRT tracking performance with focus on active gas mixture

At the end of the Run-1, a part of the TRT, namely, four out of 32 radial sectors in the inner layer of the barrel and one of the 14 wheels in the end-cap A, were filled with Argon mixture, while the other sectors were operating with the usual Xenon mixture, as shown in Figure 3.17. It was an excellent opportunity to test the implementation of the Argon mixture in the digitization package. This section contains an overview of the track and hit performance study of the TRT in this gas configuration.
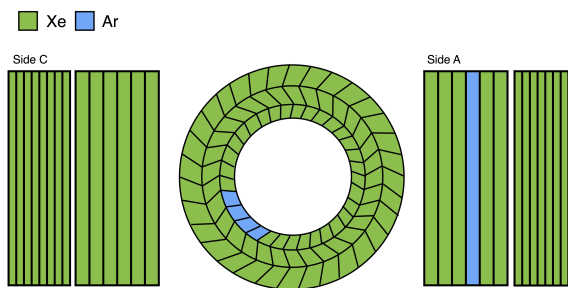
Figure 3.17.: Detector gas configuration with a couple of Argon modules used during part of 2013.

3.4.1. TRT hit and track properties

Key characteristics of a tracking detector are the spatial resolution of hits and their number. The better the resolution is, the more precisely a track and its momentum can be measured. However, there are several other characteristics sensitive to the gas mixture used in the detector, which will be discussed below. Distributions considered in this study are:

- Reconstruction hit efficiency. This parameter characterizes the probability that a particle traversing a straw will create a hit. It depends heavily on the distance of the closest approach of a particle to the anode wire, because the longer the path

of the particle is, the more gas atoms it will ionize and the stronger the signal will be. This is why it is typically plotted as a function of the track to wire distance. It is defined as:

$$\varepsilon = \frac{N_{hits}^{TRT}}{N_{hits}^{TRT} + N_{holes}^{TRT}} \tag{3.6}$$

where N_{hits}^{TRT} is the number of TRT hits in the track and N_{holes}^{TRT} is the number of holes in the track. A hole corresponds to the case when there is no hit in a straw despite a reconstructed track crossing it.

- Position residuals. As described previously (see Section 3.2.3), the width of this distribution characterizes the detector resolution.

- Number of precision and tube hits per track. These parameters directly correlate with the track momentum resolution.

- Track extension fraction, defined as a probability to find an extension of the track reconstructed in the silicon detector in the TRT.

- $r - t$ relation. It relates drift time to the drift radius and provides a direct comparison of drift velocities in Xenon and Argon mixtures.

3.4.2. Tracking performance

To make a performance comparison of Xenon and Argon straws, only straws in the first barrel layer were considered, because only the first layer contained some straws with Argon and some with Xenon (while the second and third layers were operating fully with Xenon, as shown in Figure 3.17). It is worth mentioning that the first layer of the TRT consists of two types of straws: regular and short, while the second and third layers only have regular straws. Short straws were introduced to the first layer during the design phase in order for the TRT to better cope with high-μ running conditions and to keep the occupancy on a lower level. Each layer of the TRT barrel part is split into 32 modules, which are placed radially. Modules 1-28 contained Xenon mixture and modules 29-32 contained Argon mixture. For the end-cap detector part, only one wheel in one side was operating with Argon. Therefore for the comparison the same wheel number from the other side was used in order to have the identical geometry for both Xenon and Argon cases.

One of the main differences between the Xenon and Argon gas mixtures is the electron drift velocity. Electrons drift faster in Argon. This can be seen from the plot in Figure 3.18, which shows $r - t$ relation obtained after an iterative calibration procedure using data. The Argon $r - t$ distribution is shorter by a few nanoseconds than the Xenon one, which means that the drift time for a given drift radius is shorter.
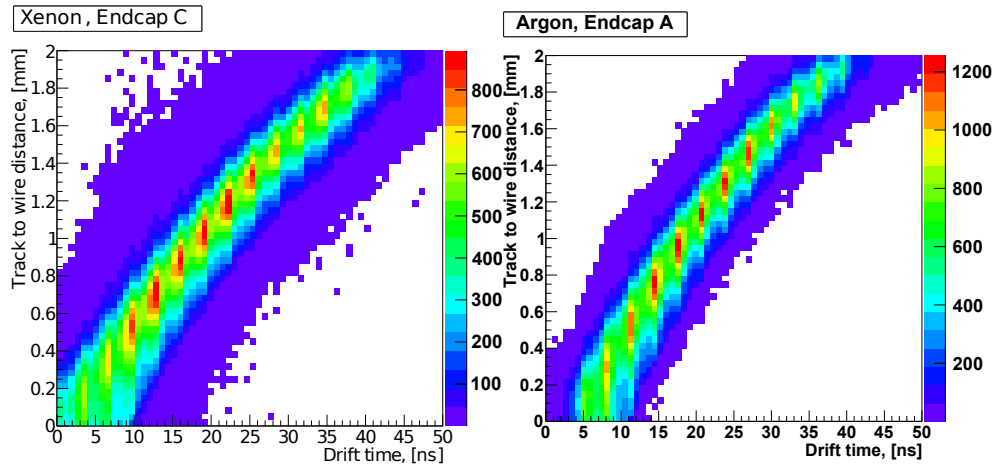
Figure 3.18.: Track to wire distance in Xenon (left) and Argon (right) straws in the end-cap detectors.

The faster drift velocity of electrons in the Argon leads thus to a shorter drift time. Since time is digitized in bins of 3.125 ns, shorter drift time will have larger digitization uncertainty. Thus Argon gas will cause a worse position resolution, which can be observed in Figure 3.19. Worse position residuals means that the momentum resolution will also become worse according to equation (3.1). Nevertheless, the difference between Argon and Xenon is small.

It is worth mentioning that these results were obtained before any fine tuning of Argon simulation parameters. Thus a slightly larger difference between data and MC distributions can be observed for Argon straws. A dedicated study was performed later by the TRT team to tune the Argon MC parameters.

The second parameter of interest is the reconstructed hit efficiency (ε). It is calculated using equation (3.6). Distributions of ε for Argon and Xenon, both for barrel and end-cap parts, are shown in Figure 3.20. Argon straws have a higher hit efficiency. To understand this effect, one has to recall that the low threshold settings for Xenon and Argon straws are quite different (300 eV versus 100 eV). The smaller low threshold
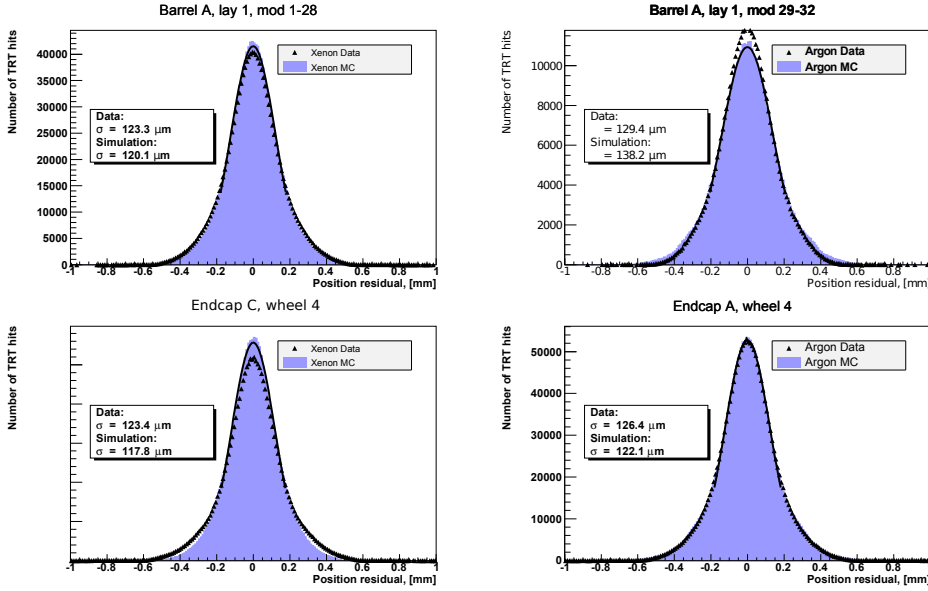
Figure 3.19.: Position residuals for Xenon (left) and Argon (right) straws in the barrel (top) and the end-cap (bottom) detectors. Data is shown with black triangles and the simulation with the solid black line.

for Argon was chosen in order to compensate for the fact that the same particle will produce a smaller number of primary electron clusters in Argon, and the number of electrons in the cluster will be smaller. It means that the signals from the Argon tubes are weaker, which means that the threshold has to be lower as well. Still, we observe higher efficiency for Argon than for Xenon. After some investigation, it was found that quite often for the signal to exceed the low threshold, two or more primary electron clusters have to reach the anode wire in Xenon straws, while in Argon in most cases only one first cluster is enough to exceed the low threshold. This is caused by the lower LT in Argon with respect to the one in Xenon. To equalize hit efficiency between Argon and Xenon, the low threshold for Argon tubes can be slightly increased. The hit efficiency is shown in Figure 3.20 as a function of the track to wire distance. It is stable throughout the straw radius except for the values close to 2 mm, which corresponds to the case when particles fly just a short path in the gas close to the straw wall. The number of primary ionization clusters is thus very small, hence the hit efficiency drops significantly.

Due to a higher hit reconstruction efficiency in Argon straws, the observed number of hits per track is also larger, as can be seen in Figure 3.21. According to equation (3.1),
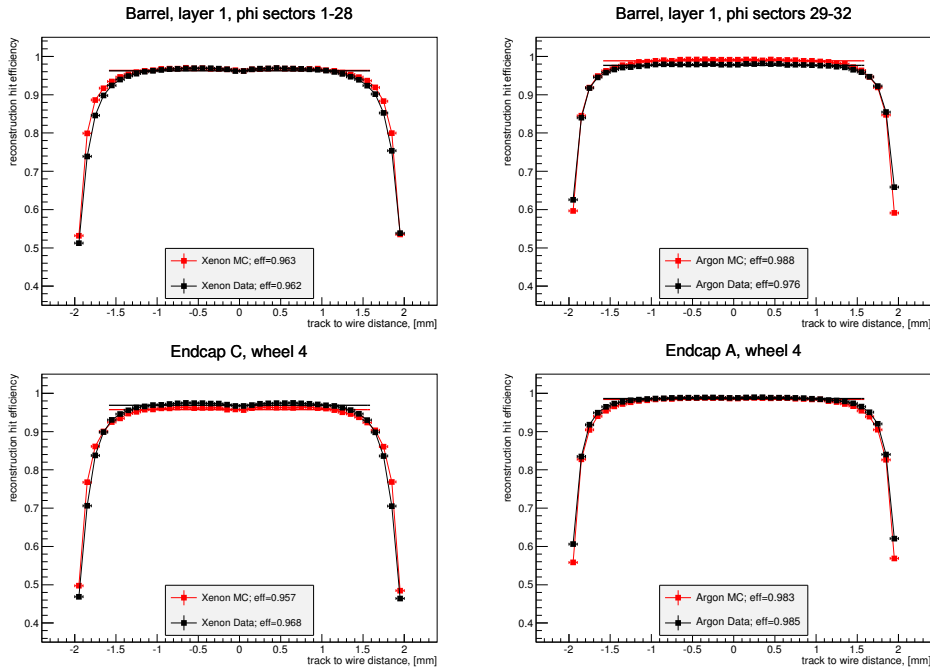
Figure 3.20.: Hit reconstruction straw efficiency as a function of track to wire distance for Xenon (left) and Argon (right) straws in Barrel (top) and End-cap (bottom) detectors.

a larger number of hits leads to better momentum resolution. However, as shown before, position residuals are worse for Argon and thus negatively affect the momentum resolution. Both factors are still quite small and therefore the momentum resolution is expected to be similar for Argon and Xenon mixtures.

The fractions of precision hits to total number of hits are shown in Figure 3.22. As mentioned earlier a hit is considered to be a precision hit if the difference between track and drift radius is smaller than 2.5 times the hit uncertainty. Argon has a higher fraction because the hit uncertainty for Argon is larger due to the faster drift time of the electron clusters and the digitization binning.

The next set of plots is related to the whole tracks. To make a clear comparison of these variables, the entire detector has to operate with either Xenon or Argon mixtures. Unfortunately, there were no such data available. Thus the comparison is made only with the Monte Carlo simulation of the two detector configurations when all tubes contain either Argon mixture or Xenon mixture. In Figure 3.23, the track extension fraction is shown. This parameter characterizes the probability to find a continuation
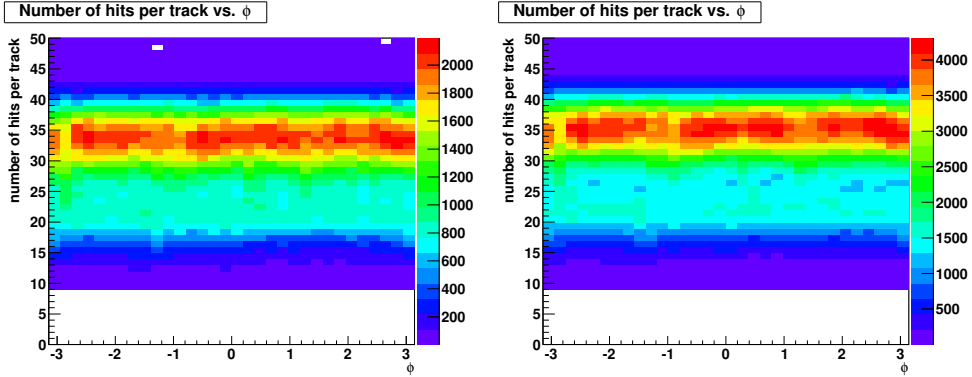
Figure 3.21.: Simulation of the number of hits per track in configurations with all straws filled with Xenon (left) and Argon (right) gas mixtures in the barrel detector.
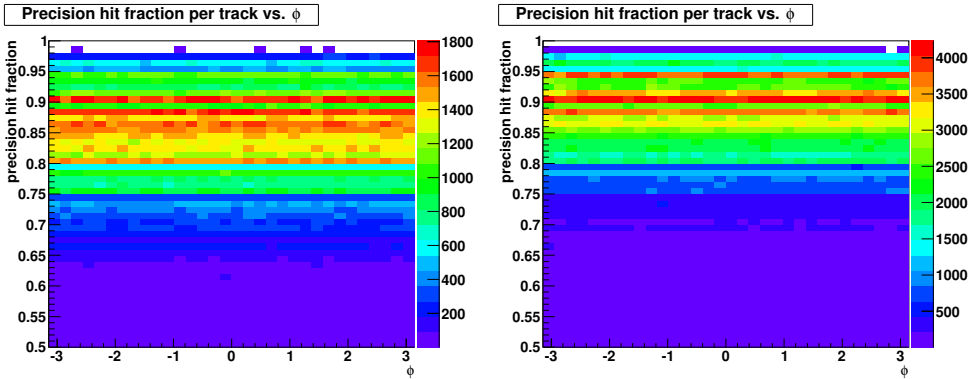
Figure 3.22.: Simulation of the precision hit fraction as a function of ϕ in configurations with all straws filled with Xenon (left) and Argon (right) gas mixtures in the barrel detector.

of a track reconstructed in the silicon part of the Inner Detector in the TRT. In the barrel region this fraction is flat, except for the area around $\eta = 0$. This can be explained by the inefficiency of the first few layers of straws in the barrel region since the first layers of the barrel region contain shorter straws compared to other layers. As mentioned before, short straws help to deal with the occupancy at high μ. These short straws are split into three parts by two glass joints. Moreover, only two outer straw parts are read out by the electronics and so the middle section (which is placed around $\eta = 0$) is not read. This is therefore an inefficient region of the detector and this is why a drop in the extension fraction is observed. The behavior of the end-cap region can be explained by geometrical factors, because in the intermediate region between the barrel and

the end-caps particles traverse a smaller number of straws and with increasing η the number of straws is increasing. One can observe that the fraction is slightly higher for the Argon straws. This can be explained by the higher reconstruction hit efficiency and the larger number of hits per track for Argon tubes.
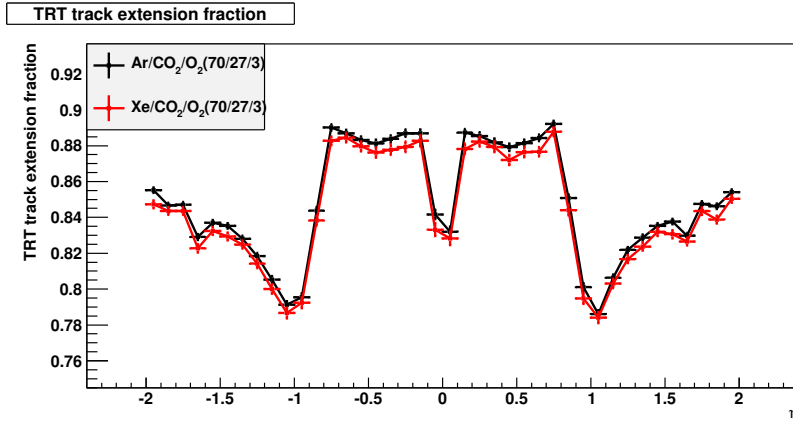
Figure 3.23.: Simulation of the track extension fraction as a function of η for Xenon and Argon gas mixture.

3.5. Summary

The implementation of the new Argon gas mixture to the TRT digitization code has been discussed. The simulation of an Argon gas mixture works well although a fine tuning of the simulation is needed. The tracking performance of the TRT was compared for the case of Argon and Xenon gas mixtures, and it was found that the tracking performance was not significantly affected by the gas mixture used. Operating the TRT with some parts with Argon mixture will therefore not affect tracking performance.

Chapter 4.

LUCID - The ATLAS Luminosity Monitor

This chapter describes the LUCID-2 detector which was built specially for the Run-2 phase of the LHC program. It covers aspects such as the design of the detector and its key components,the assembly and testing of the new detector as well as operation and performance of the detector during the 2015-2016 data taking periods. Special attention is given to the calibration system of the detector and the development of the calibration procedure.

4.1. The new LUCID-2 detector

LUCID (LUminosity Cherenkov Integrating Detector) is a luminosity monitor with two detectors placed around the beam-pipe on both forward ends of the ATLAS detector. It is a relative luminosity detector which detects inelastic pp scattering events in order to measure luminosity and provide online monitoring of the instantaneous luminosity. The first version of the detector was installed in 2008 and it is described in [40]. It was used as the main luminosity detector for Run-1 of the LHC program in 2009-2010 [57] and in combination with other luminosity detectors in 2011-2013. The second version of the detector and read-out electronics was designed to cope with the increased luminosity and the decreased bunch spacing (from 50 ns to 25 ns) for Run-2 of the LHC program. In this section the design of the new detector and its electronics is presented.
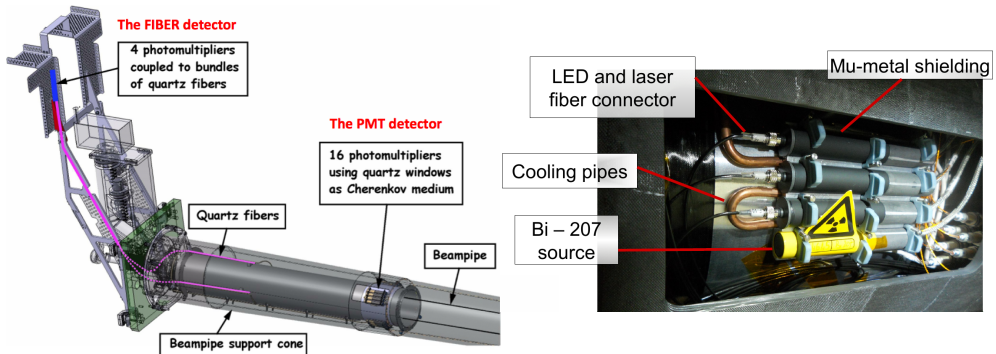
Figure 4.1.: (left) Schematic drawing of one of the two detectors, showing the position of the photomultiplier tubes and quartz fibers with respect to the LHC beampipe; (right) A quarter of one of the detectors. All tubes are placed inside mu-metal shielding to protect the PMTs from a stray magnetic field. Cooling pipes carrying water were installed in order to protect the PMTs from overheating during the beampipe bake-out procedure. Three of four tubes have fiber connectors, which transfer LED and laser pulses for calibration. The fourth tube is equipped with a Bi-207 source and is completely sealed.

4.1.1. The detector design

LUCID consists of two identical parts which are placed on both sides of the ATLAS intersection point at a distance of 17 meters. Each detector consists of 20 photomultipliers (PMTs). 16 of them, grouped four by four, are placed close to the beampipe. The center of these photomultipliers is at a distance of 125 mm from the beamline. These PMTs detect charged particles that traverse their quartz windows, where Cherenkov light is produced. Four other PMTs are placed 1.2 m away from the beampipe and are protected by the massive muon shielding. Cherenkov light is also produced in quartz fiber bundles that runs parallel to the beamline and that are coupled to the PMTs (see Figure 4.1 left).

The 20 PMTs are grouped in 5 different families:

- FIB PMTs are the ones that are protected by the shielding. Cherenkov light is produced and delivered by quartz fibers bundles (which consist of 37 optical fibers each with a 0.8 mm quartz core).

- BI PMTs are equipped with a Bi-207 radioactive source which is used for PMT gain monitoring.

- VDM PMTs were meant to be used during so-called van der Meer (vdM) scan [58,59] taken to determine the absolute luminosity.

- SPARE PMTs are spares and can be turned on if the VDM PMTs have aged too much or break down.

- MOD PMTs have a thin ring-shaped layer of aluminium deposited between the quartz window and the photocathode. The center hole of this ring has a diameter of 7 mm which can be compared to the 10 mm diameter of the photocathode and the layer thus reduces the acceptance of these photomultipliers by a factor of 2 which will help to avoid saturation of some luminosity algorithms.

BI, VDM, SPARE and MOD PMTs are grouped together and 16 PMTs form four such groups which are placed equidistantly from each other around the beampipe (see Figure 4.1 left).

The gain of the PMTs is monitored by the dedicated gain monitoring system which is described in Section 4.2.

With respect to the detector used in Run-1 [57], the new LUCID has a reduced material budget, an increased dynamic range and can measure luminosity with additional algorithms based on so-called PMT charge integration in which the pulses are integrated with flash analog-to-digital converters (FADC).

4.1.2. Choice of photomultipliers

The new LUCID uses R760 Hamamatsu PMTs, a smaller version of the previously used R762 model. These PMTs have a 10 mm quartz window diameter, while the old ones had a 14 mm diameter. A smaller PMT model has been chosen to reduce acceptance which will help to cope with the increased occupancy and to avoid saturation of the luminosity algorithms. In addition, 4 PMTs per side (MOD PMTs) have a specially reduced sensitive window with a 7 mm diameter which roughly corresponds to a factor 2 decrease in acceptance (see Figure 4.2). They provide luminosity algorithms that will saturate at higher luminosity than the standard photomultipliers. A detailed description of choice and characterization of the PMTs used in the detector can be found in [60].

Figure 4.2.: R760 Hamamatsu PMT with specially reduced sensitive window size used in the LUCID detector.
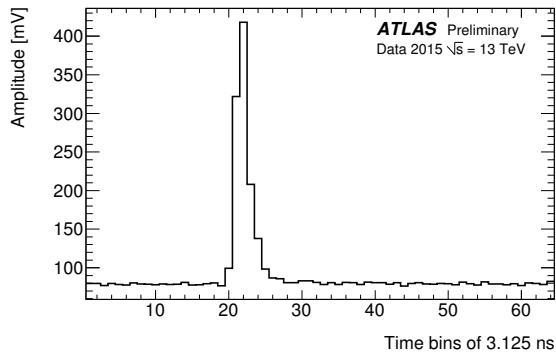
Figure 4.3.: Digitized pulse shape of a signal from one of the PMTs of the LUCID detector during a run recorded on the 10th of June 2015 at $\sqrt{s}$ = 13 TeV. The polarity of the pulse is inverted. The FADCs measure the pulse amplitude in time bins that are 3.125 ns long.

4.1.3. Read-out electronics

New readout electronics have been built that consist of VME boards that digitize the PMT signals with FADCs. The electronics record hits if the pulseheight is above a threshold and integrate the pulses in each 25 ns interval that corresponds to a LHC bunch crossing. Figure 4.3 shows a typical PMT signal shape in a physics run. The duration of the pulses is less than 25 ns.

The LUCID read-out consists of four (two per side) custom made so-called LU-CROD (LUCid ReadOut Driver) boards of VME type which sit close to the detector in the ATLAS experimental hall. The decision to place electronics close to the detector in
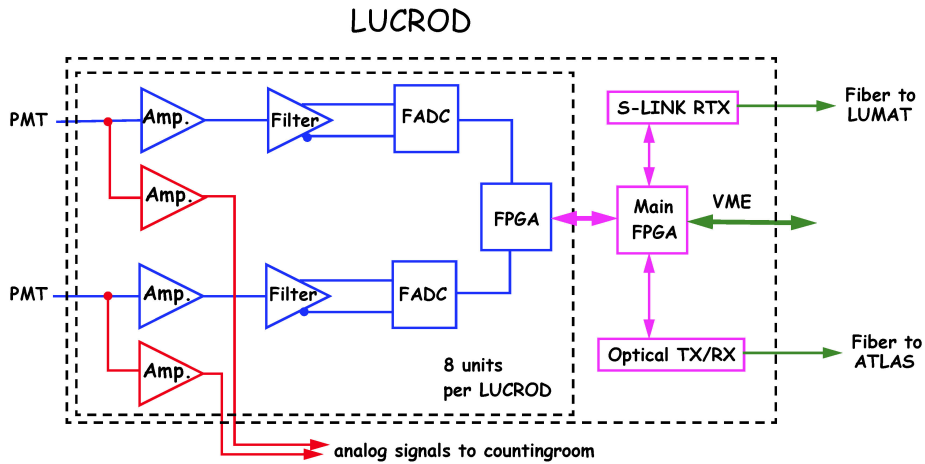
Figure 4.4.: Block diagram of the LUCROD board. Every board host two input channels. Every channel consist of a low noise amplifier, a flash ADC and a shared FPGA. There are 16 channels (8 units) per LUCROD. All units are controlled by the main FPGA, which collect information from all channels and make the required calculations.

the experimental hall was motivated by preventing signals to develop long tails in the cables. Signal from PMTs are transferred with thick cables which prevent distortion along their path. Every LUCROD board has 16 input channels and every channel consists of a low noise amplifier, a filter and a FADC. A block diagram of a LUCROD module is shown in Figure 4.4. Channels are grouped in pairs and for each pair there is a dedicated channel FPGA. All information from all channel FPGAs is collected and processed by the main FPGA. After that the information is sent to ATLAS as well as to the so-called LUMAT (LUminosity Monitor And Trigger) boards which are placed in the counting room of the experiment.

There are two LUCROD boards per side and it was decided to couple different sets of sensors to the different boards, as shown in Figure 4.5. BI, VDM and SPARE PMTs were connected to one board, while MOD and FIB PMTs were connected to the other board. The same connection scheme was used on the other side as well.

Every LUCROD board receives information from PMTs situated in one of the two detectors. In order to implement the possibility of requiring signals in both detectors, two additional boards, called LUMAT boards, are used as shown in Figure 4.5. Digital signals from PMTs of the same family, from LUCRODs on both sides, are sent to LUMAT boards, which then perform logical operations with signals from both sides.
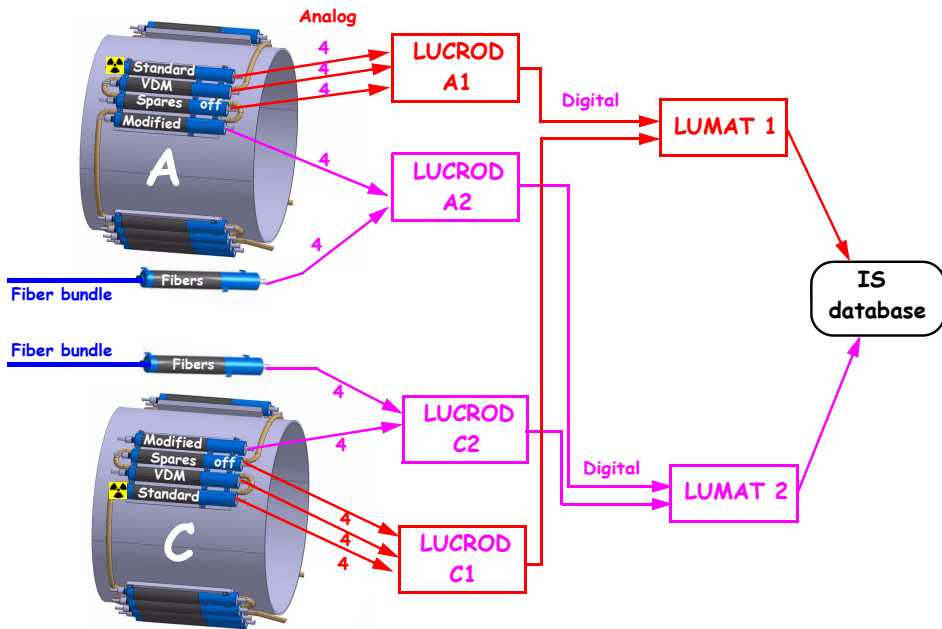
Figure 4.5.: Block diagram of the LUCID electronics. Signals from all photomultiplier tubes are collected by 4 LUCROD cards (two per side) that digitize the signals with FADCs. Some of the luminosity algorithms are implemented in the LUCRODs. The number of events that fullfil different luminosity algorithms are counted and a copy of all digitized PMT signals are sent to the LUMAT cards, which perform calculations with algorithms that combine data from both detectors and publish the results to the Information Server (IS) database.
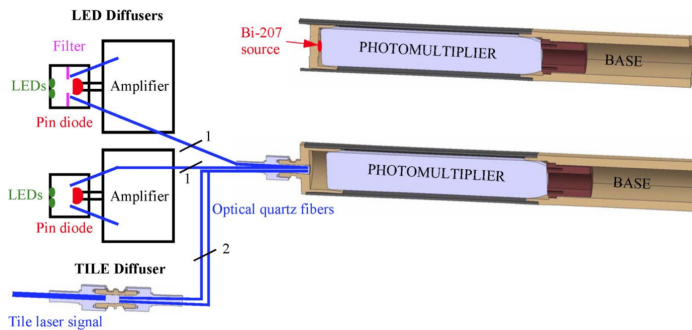
Figure 4.6.: The LUCID PMT gain monitoring system. 16 PMTs per side receive light from LEDs and the Tile laser calibration system. For redundancy, two fibers come from two different LED diffusers (with three LEDs each, monitored by PIN-diodes), and two fibers come from one laser diffuser. The four remaining PMTs in each detector are calibrated with Bi-207 sources.

Information from the LUCROD and LUMAT boards are then published to the Information Server (IS) which is a database. From there the data are accessed by programs that calculate the luminosity online.

4.2. Design of the PMT gain monitoring system

The PMT gain is monitored in 3 independent ways (see Figure 4.6):

- by LED signals carried by optical fibers;

- by laser signals transferred from the calibration system of the ATLAS Tile Calorimeter;

- by radioactive sources (Bi-207).

PMTs which are coupled with Bi-207 radioactive sources constantly see signals of radioactive decays which are treated as a background during luminosity measurements. This is why the activity of the radioactive sources has to be as low as possible on one hand, but on the other hand it has to be large enough to produce enough statistics for the calibration during the 20-30 minutes available between the LHC interfills. The source activity is completely negligible during physics runs with many pp interactions per bunch crossing. However, source activity could become a problem in special beam-separation runs (van der Meer runs), used for the absolute luminosity

calibration, due to the low luminosity. For these runs VDM PMTs were expected to be used. However, analysis of the first set of van der Meer runs, described in Section 4.4.2, demonstrated that the activity of the Bi-207 sources is small enough to allow the use of BI PMTs for absolute luminosity calibration as well. The gain of the BI PMTs is monitored by the radioactive sources, while the gain for all other PMTs is monitored by LED and laser light.

LED signals provide peaks in the amplitude and charge distributions that are recorded by LUCID in data acquisition runs between LHC fills. The stability of the PMT gain is controlled by measuring the mean value of these distributions and then changing the high voltage to the photomultiplier in order to keep these mean values constant. The stability of the LEDs themselves is controlled by PIN-diodes and an alternative way of calibration is to use the ratio of the mean charge measured by PMTs with that of the PIN-diode. This charge is proportional to the LED intensity and by using this charge ratio it is possible to rule out any dependence of the calibration results on LED intensity fluctuations. In order to provide the same amount of light simultaneously to all PMTs, a special LED diffuser was designed and manufactured. This is discussed in details in Section 4.2.1.

The Tile calorimeter laser system provides an alternative source of stable light and is treated in the same way as the LED signals in the calibration procedure. The stability of the laser signals is monitored by the Tile calibration system [40]. The laser light has to be distributed between the PMTs in the same way as the LED light. Laser light is provided by the Tile calibration system via optical fibers which means that another type of diffuser has to be used in order distribute the light to the PMTs, as described in Section 4.2.2.

Bi-207 radioactive sources provide monoenergetic electrons from an internal conversion process with energies above the Cherenkov threshold in quartz. These electrons have enough kinetic energy to penetrate the quartz window of the PMT and produce signals similar to the signals from high energetic particles in physics runs. The truncated mean of the charge and amplitude distributions from the Bi-207 sources are used in the same way as for the two methods described above. This method does not suffer from any instability issues [60]. It was decided to use a liquid Bi-207 source, as described in Section 4.2.3.

In Section 4.4.3 the calibration strategy during the 2015 and 2016 data-taking periods is discussed.

4.2.1. The LED diffuser

Despite the simple purpose of the LED diffuser to evenly distribute light among the PMTs, there was a number of constrains that made it necessary to make dedicated studies to define the optimal parameters of the diffuser. The main points which were considered during the design phase were:

- light had to be evenly distributed among PMTs;

- the LED had to be monitored by PIN-diode in order to verify its stability;

- the sensitivity of PMTs and PIN-diodes to light is very different;

- geometrical constrains such as the size of the PIN-diode, limited space for the whole diffuser and limits on the bending of fibers had to be taken into account;

- manufacturing constrains such as the complexity of drilling small holes and gluing fiber at specific angles had to be kept in mind.

To meet all these requirements a radial design was proposed with a PIN-diode facing three LEDs and located aligned with the LEDs axis. Fibers surround the PIN-diode evenly with a certain angle to the LED axis. A schematic sketch is shown in Figure 4.7 and in Figure 4.8. Such a geometry assumes that the distance between the LEDs and the fibers is the same for all fibers in order for the fibers to pick up the same amount of light.

The manufacturer provided information about LED light intensity as a function of the angle between an observer and the LED axis (Figure 4.9 (right)). A set of measurements was also done. A sketch of the experimental setup is shown in Figure 4.7. Measurements of the PMT anode current as a function of fiber angle with respect to the LED axis for different distances between the fiber surface (PIN-diode) and the LEDs were done and the results are shown in Figure 4.9 (left). With angles below 30°the intensity is relatively homogeneous, and above 30°the light intensity starts to drop off.

The sensitivity of the PIN-diodes is significantly smaller than that of the PMTs. That's why, in order to have enough light intensity to see a clear signal with PIN-diodes, one needs as small as possible distance between the LEDs and the PIN-diode. However, since the fibers sit around the PIN-diode case and due to geometrical constrains (the diffuser has certain space requirements in order to fit in the limited space inside the ATLAS shielding) the angle between the fibers and the LED - PIN-diode axis cannot be
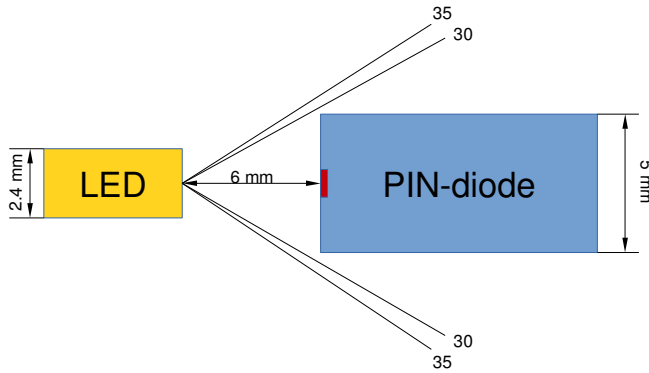
Figure 4.7.: Schematic of the experimental setup which was used in the LED diffuser design phase. LED and PIN-diode are aligned and face each other. Angles represent possible positions of the fibers around the PIN-diode. Fibers are not shown in the sketch.
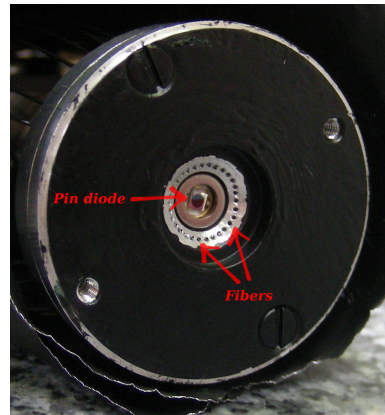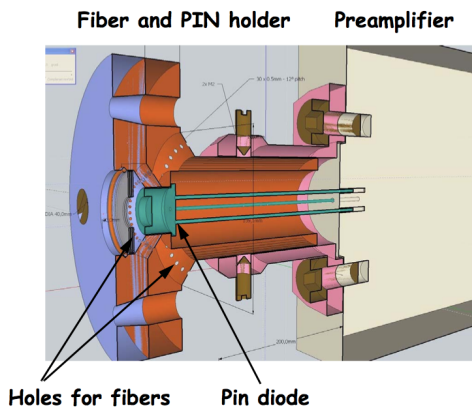
Figure 4.8.: The LED diffuser. Schematic drawing (left), photo (right).
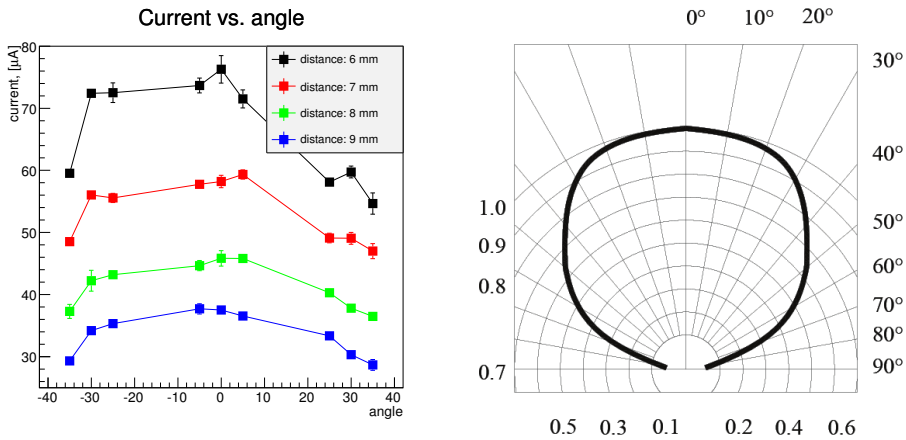
Figure 4.9.: Measurements of PMT anode current as a function of angle between fiber and LED axis for different distances between fiber and LED is shown in the left. A measurements by the manufacturer of the angular homogeneity is shown on the right.

very large because then the fibers have to be bent too much which can damage them during the detector installation.

The final design had a 6 mm distance between the PIN-diode and the LEDs and a $30°$ fiber angle.

The different sensitivity of the PMT and the PIN-diode led to another limitation caused by the dynamic range of the LUCROD board. The dynamic range is the maximum possible input voltage (after amplification) at which the read-out card has an output that is linear and thus not saturating. The dynamic range of the LUCROD card is 1.5 V. The input signal is amplified with a low noise amplifier with an amplification factor of 14, as discussed previously.

The maximum possible amplitude of the PMT signals which can be handled by the electronics without any saturation is therefore slightly above 100 mV. This introduces a limitation for the diffuser because the intensity of the LED cannot be too high, so that it produces larger than 100 mV PMT signals. However, for this LED intensity the signal from the PIN-diode will be very small and barely measurable. It was therefore needed to suppress the amount of light which goes to the fibers while keeping high intensity light for the PIN-diode. The solution was to place a ring of optical filters which covers the fibers but not the PIN-diode.

Two sets of filters with the optical densities 0.15 and 0.6 were used. Measurements with many possible combinations of filters were done in the laboratory. The setup was the same as shown in Figure 4.7. The distance between the LED and the PIN-diode and the fiber angle were set to the values decided to be used in the diffuser. Filters were inserted between the LED and the fiber to reduce the amount of light picked up by the fiber. Measurements were repeated three times for each filter configuration. The results of the measurements are shown in Table 4.1. It was decided to choose a combination with one filter with 0.15 optical density and one with 0.6, which gave a PMT signal amplitude of 85.33 $\pm$ 0.29 mV. This amplitude is slightly smaller than the threshold value of 100 mV in order to have a safety margin in case fibers are slightly off from the nominal position in the diffuser.

The LED diffuser had to be placed on top of the so-called shielding monoblock, where radiation levels are expected to be low compared to the areas close to the beampipe where LUCID sits. However, some amount of radiation will be present also in the location of the LED diffusers during operation. No estimation of the radiation hardness of the filters was done, which is why it was decided to make one diffuser with filters and another one without.

Filter configuration	Signal amplitude [mV]
2x0.15	147.90 $\pm$ 1.05
3x0.15	129.67 $\pm$ 0.72
4x0.15	106.47 $\pm$ 1.77
1x0.6	109.93 $\pm$ 0.12
1x0.6 + 1x0.15	85.33 $\pm$ 0.29
1x0.6 + 2x0.15	61.67 $\pm$ 0.62
1x0.6 + 3x0.15	41.83 $\pm$ 0.35
2x0.6	30.13 $\pm$ 0.41

Table 4.1.: Results of the measurements in the laboratory with a LED diffuser prototype to choose proper combination of optical filters to be used.
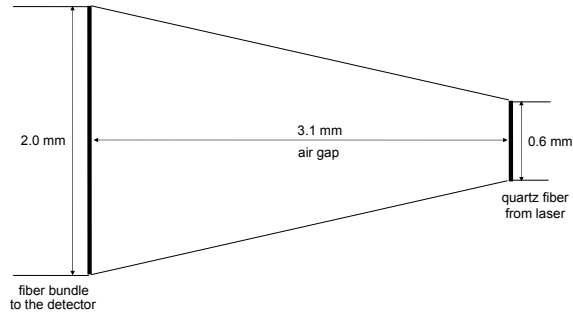
Figure 4.10.: Schematic drawing of a laser diffuser that couples a fiber bundle to the single quartz fiber which delivers laser light from the Tile calibration system.

4.2.2. The laser diffuser

The stability of the light source used for PMT gain monitoring is a crucial factor in the calibration procedure. Instead of relying on only one light source from LEDs it was decided to also use laser light provided and monitored by the Tile calibration system. To distribute the light between the PMTs one cannot use the same diffuser as for LED light, since laser light is very well collimated, which is not the case for the LEDs. In order to handle the laser light, a new diffuser was made, as shown in Figure 4.10. The diffuser connects a fiber bundle of 48 quartz fibers encased in a ferrule connector of 2 mm diameter with a single fiber of a 0.6 mm diameter, since the laser light is delivered from the Tile calibration system by a single fiber.

The light in the fiber undergoes multiple total internal reflections in the interface between the fiber core and the cladding. Due to this, the light from the fiber will come out within a certain cone. The size of the cone is characterized by the numerical aperture NA of the fiber, is given by

$$NA = n \sin \theta_{max} = \sqrt{n_{core}^2 - n_{cladding}^2} \qquad (4.1)$$

where n is the refractive index of the medium (air in our case), n_{core} is the refractive index of the fiber core, $n_{cladding}$ is the refractive index of the cladding and θ_{max} is half-angle of the light cone. To distribute the light from the single fiber to the fiber
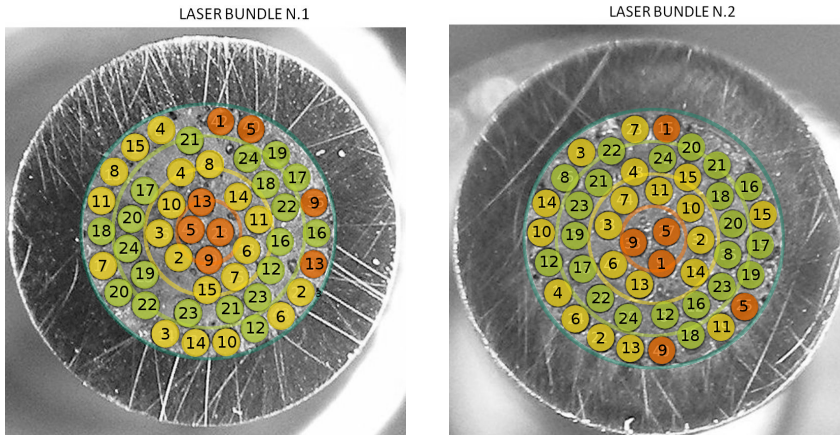
Figure 4.11.: (left) Picture of a laser diffuser with the fiber bundle which delivers laser signals to PMTs on the side A detector. Numbers correspond to PMT numbers which the fiber is connected to. Two fibers from a bundle are connected to each PMT. Fiber pairs are divided into three categories based on the distance from the center of the connector to the closest fiber in a pair: central (orange color), intermediate (yellow) and peripheral fiber pair (green). (right) Laser diffuser for the side C detector.

bundle one has to introduce an air gap between them that depends on the NA, as shown in Figure 4.10. The fiber used to deliver the laser light has a numerical aperture of 0.22, which corresponds to a 3.1 mm air gap needed to cover the 2 mm surface of the diffuser by a light spot (according to equation (4.1)). The light received by each PMT has to be similar for all photomultipliers. However, the intensity of the light is not constant within the light spot and dedicated measurements were necessary to determine the optimal air gap distance. Two conditions had to be met:

- The light has to be evenly distributed between the PMTs,

- A preference is given for a configuration in which the dimmest channel is given as much light as possible.

Each PMT is connected to two fibers in a bundle. For small distances between the fiber with the laser signal and the fiber bundle, one expects the largest intensity for the central region of the diffuser, while for the peripheral region one expects the lowest intensity. The diffuser is divided into three regions: central, intermediate and peripheral. If one of the fibers from a pair is in the central or intermediate region, another fiber from the pair was placed in the most peripheral ring of the diffuser. If
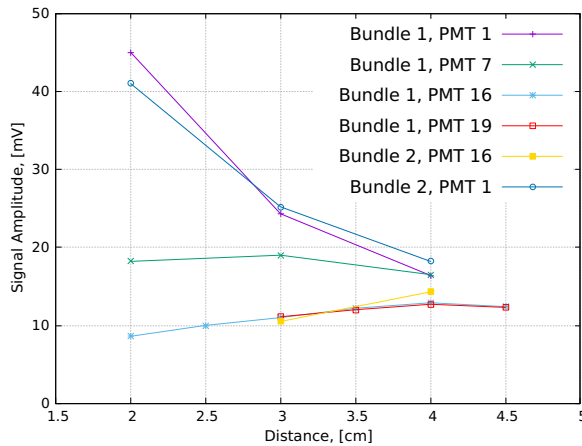
Figure 4.12.: Measurement of the PMT signal amplitude as a function of air gap distance for different categories of fibers. Fiber pairs connected to PMTs 1 represent central fiber pairs, PMT 7 intermediate pairs, PMTs 16 and 19 to peripheral pairs.

both fibers in a pair are in the peripheral region, they were placed as close as possible to the center of the diffuser. Pairs which include one fiber in the central region are called central fibers and marked orange in Figure 4.11. Pairs with one fiber in the intermediate region are marked yellow, and pairs marked green have both fibers in the peripheral region.

The measurements were done with different air gap distances for fiber pairs from each category. Due to the identical structure of the fiber bundle on side A and side C (or bundle 1 and 2), detailed measurements were done only for one bundle and only a few points were measured with the second bundle to verify the results of the first one. The amplitudes of the PMT signals were measured by an oscilloscope in the ATLAS experimental hall and the results are shown in Figure 4.12. PMT 1 represents PMTs with a central fiber pair, PMT 7 - an intermediate pair and PMT 16 and 19 - peripheral fibers for bundles 1 and 2. With increasing distance the signal amplitude is decreasing for central fibers as expected. Intermediate and peripheral fibers have maximums. The maximum for the peripheral fibers corresponds to a distance of 4 cm. Homogeneity within all categories is acceptable at 4 cm, so this distance was chosen for the final version of the diffuser.
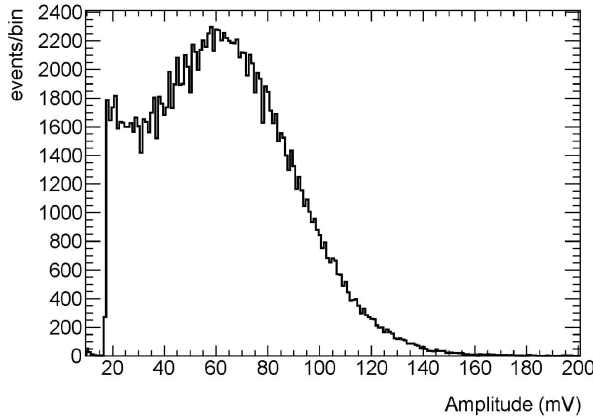
Figure 4.13.: Pulseheight distribution of Bi-207 radioactive source signals measured in a test
with a Hamamatsu R760 PMT.

4.2.3. PMTs with a Bi-207 source

To use LED or laser light sources as a reference for the PMT gain monitoring system
one has to be sure that intensity of the light delivered to the PMT will stay constant
over a long period of time. In other words one has to be sure that the light source itself
is stable and the condition of the optical fibers which deliver light to the PMTs stays
the same. An alternative option which is robust against the effects above is to use a
radioactive source.

It was decided to use a Bi-207 source because it provides monoenergetic electrons
from an internal conversion process with energies above the Cherenkov threshold in
quartz. In order to use Bi-207 for gain monitoring one needs to put the radioactive
source close to the PMT. A set of measurements with Bi-207 radioactive sources were
done in a test set-up and it was found that the peak from the electron source (shown
in Figure 4.13) corresponds to approximately 30 photoelectrons [60].

A radioactive source was enclosed in a circular case with 25 mm diameter (the
source itself is a disc with a diameter of 5 mm enclosed in a plastic film) as shown in
Figure 4.14. During measurements the source was put in contact with the PMT quartz
window. The size of the source is larger than the size of the PMT quartz window
(25 mm compared to 10 mm respectively) which led to an observed dependence of
the shape of the charge and pulseheight distributions (such as in Figure 4.13) on the
relative position of the source with respect to the center of the PMT quartz window. It
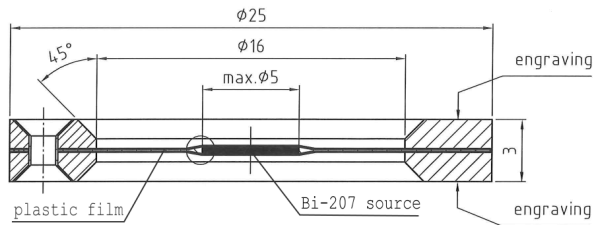
Figure 4.14.: Schematic picture the of case of a Bi-207 radioactive source used in the measurements during the characterization of the PMTs [60].

led to difficulties in positioning sources in the same way for all sets of PMTs. Despite this issue, the main problem with using Bi-207 source was the fact that the source has a 2.5 times larger size than the quartz window and it could therefore not be used in the final detector. It was decided to use liquid Bi-207 sources and put one drop on the surface of the quartz window, which eliminated the geometrical issue as well. In order to prevent contamination by the source, a special cap was glued on top of the PMT.

4.3. Temperature dependence of the PMT gain and the temperature tolerance of calibration fibers

During the first long LHC shutdown (LS1) between 2013 and 2015 the beampipe at the interaction point of ATLAS had to be removed and to be replaced with a new one made of aluminium instead of stainless steel. The new material was chosen to minimize the induced radioactivity of the beampipe. The new beampipe also had a reduced aperture in the inner detector region to allow for a new pixel inner barrel layer (IBL) of the inner tracker.

In order to remove residual gas molecules from the inner walls of the new beampipe (which otherwise will lead to significant beam-gas interactions during operation) the beampipe had to undergo a so called "bake-out" process, which consists of heating up the walls of the beampipe from the outside.

Since LUCID sits close to the beampipe there was a need to understand the temperature tolerance of the detector components. During the design phase a special cooling system of the detector was proposed in order to protect PMTs, cables and calibration fibers against potential overheating. The PMTs were placed on a special metal support,
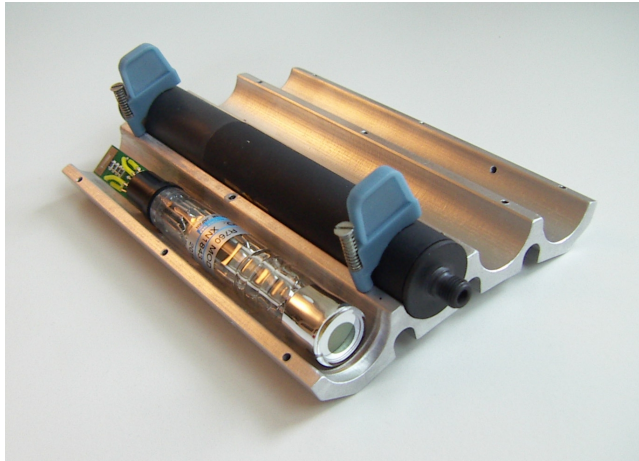
Figure 4.15.: Metal support for the PMT tubes that is used in the LUCID detector.

as shown in Figure 4.15, which were cooled down by water pipes. Fibers and cables go along the beampipe for a few meters and were more exposed to heat than the PMTs. They are also protected with cooling pipes, though it was practically impossible to provide cooling along the whole path of the fibers and therefore some areas of fibers are not cooled by the water pipes.

Special studies were done in order to understand the temperature tolerance of the quartz fibers used in the detector, as described further in this section.

Another temperature test described in this section was focused on understanding the temperature dependence of the PMTs gain during their operation.

4.3.1. Temperature controller

In order to perform any temperature tests one has to have a reliable method to measure and control temperature in the testing area. Measurements with PMTs are typically done in a light-tight black box to make sure that no external light will accidentally get on the PMT photocathode. The black box is well sealed which prevent air from the box to circulate outside, making it easy to control the temperature inside the box with a good precision. A dedicated temperature controller, based on the Arduino Mega 2560 microcontroller [61] (programmed by Arduino software), was built for this purpose. To measure temperature, the LM35CAH sensor was used which is a
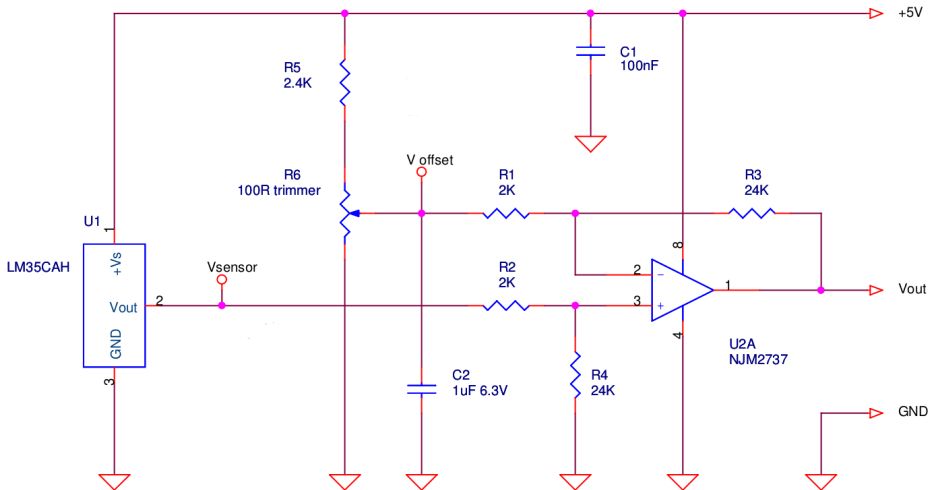
Figure 4.16.: Electrical circuit used to connect the temperature sensor LM35CAH to the Arduino read-out.

precision integrated-circuit device with an output voltage linearly proportional to the temperature in $^\circ$C. In order to interface the sensor with the readout input channel from the Arduino board, an electrical circuit (see Figure 4.16) was made, to match the output voltage from the sensor to the readout of the Arduino board. As a heater element, a simple chain of resistors was used, dissipating heat produced by the current flowing through it. The voltage on the resistors was controlled by a controller with the help of a MOSFET transistor. In order to make sure that the temperature was homogeneous within the black box, a PC fan was used to circulate the air. A heating profile was programmed in the Arduino microcontroller and the measured temperature values were sent directly to a personal computer by a serial port or were stored on an external microSD card that was connected to the Arduino board.

4.3.2. The PMT gain dependence

It is known that a PMT is more sensitive to ambient temperature than ordinary electronic components (such as capacitors and resistors) [62]. It is caused mainly by two factors: the cathode quantum efficiency is sensitive to temperature variations, and the gain of the dynode chain depends on the temperature as well.
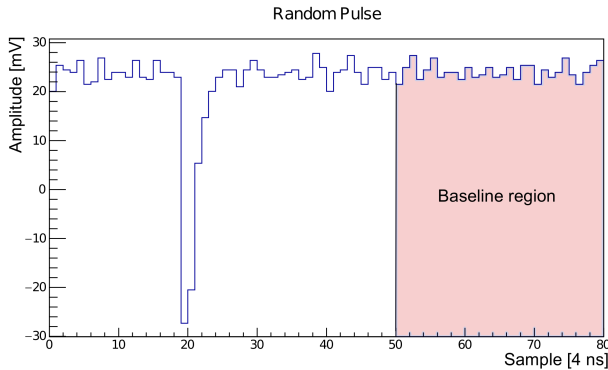
Figure 4.17.: Shape of a digitized pulse from a Bi-207 source. For pulseheight measurement the baseline has to be measured and subtracted in a region without signals.

To estimate the temperature effect on the PMT gain, a dedicated measurement was done. A R760 Hamamatsu PMT was placed in the black box together with a Bi-207 radioactive source to provide stable input signals over time. The temperature in the box was controlled by the temperature controller described in Section 4.3.1.

The interior of a PMT is at vacuum, and heat conducts through it very slowly, thus the temperature gradient has to be very small in order to make sure that the temperature of the tube reaches the same level as the ambient (measured) temperature. In order to satisfy this condition the temperature gradient was chosen to be 0.2° C per hour.

The PMT signal was digitized by a 12 bit VME Flash ADC which was operated by the ATLAS central Trigger and Data Acquisition (TDAQ) framework. In order to record only signals from the Bi-207 source, a triggering was done that requires a signal above a certain threshold. The digitized pulseheight of every triggered event was stored in ROOT files. The shape of the digitized pulses from a Bi-207 source is shown in Figure 4.17.

In order to calculate the charge and the amplitude of the Bi-207 signal, the baseline had to be subtracted. To estimate the baseline value, the last 30 (out of 80) FADC samples were used, as shown in Figure 4.17.

The recorded rate of the Bi-207 signals was around 150-200 Hz. In order to collect enough statistics to measure the mean of the charge and the amplitude distributions, every measurement was done for 5 minutes. After one measurements was finished,
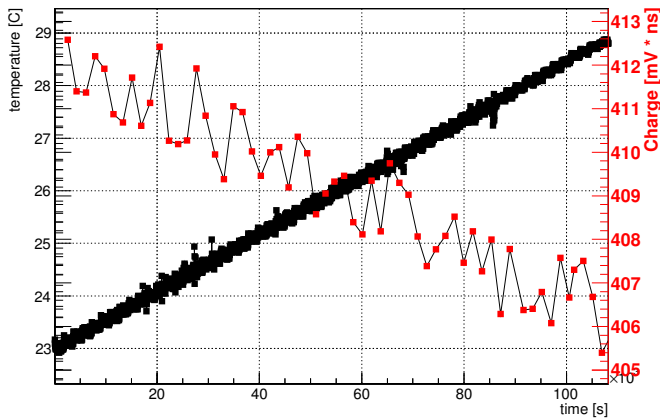
Figure 4.18.: The temperature dependence of the PMT gain represented by measurements of the mean of the charge distribution of Bi-207 source signals for different temperature values. Black markers correspond to the temperature measurement; red markers correspond to the mean of the charge distribution of Bi-207 signals collected for 5 minutes.

another was immediately started. Due to the very small temperature gradient (0.2° C per hour) the temperature within one measurement was considered to be constant.

The mean of the charge distribution and the temperature as a function of time is shown in Figure 4.18. Black points represent the measurements of the ambient temperature. The temperature was slowly increasing and the total change was 6° C over 30 hours. Red points show the mean of the charge distribution in 5 minute intervals. A clear decreasing trend is observed, which represents the temperature dependence of the PMT gain. The measured temperature dependence was 0.25 % of gain per 1° C.

4.3.3. Bake-out tests of the calibration fibers

The goal of this test was to estimate the temperature threshold at which fibers started to loose their optical properties due to heat damage of the cladding and/or the fiber core.

The experimental setup consisted of a PMT placed in the black box, a LED source and a fiber bundle. Light was transmitted from the LED to the PMT by the fiber. The

fiber bundle was placed in the thermoinsulated box, while the LED and the PMT were outside and not heated.

A high ambient temperature was obtained inside the box with the help of a thermogun, which was blowing hot air into the box constantly. The temperature was measured with the Arduino-based temperature controller described in Section 4.3.1, with the temperature probe inside the box.

The first set of measurements were done at room temperature inside the box in order to use this value as a reference (first phase of the experiment). In the second phase the thermogun was switched on and the temperature raised to around $95°$ C. This temperature was kept constant for slightly more than one hour to make sure that the fiber was exposed to a high temperature for a long enough time period to make any changes observable. In the third phase, the power of the thermogun was increased further and the temperature of the air was raised to $110°$ C and kept at this level for one hour. In the last phase the thermogun was switched off and the measurements were done for another half an hour. The LED was pulsed by a pulse generator with a rate of 1 kHz and the FADC was triggered with the same signal in order to make sure that only signals originating from the LED source were stored. Every measurement was done for a 5 minute interval and the next one was started as soon as the last one had finished. The mean of the charge distribution was calculated for each measurement and is shown as a function of time with red points in Figure 4.19. Black points correspond to the temperature measurements done during the same time. The charge measurements during the second phase (when the temperature in the box was $95°$ C) are compatible with measurements done during the first phase (at room temperature) and are stable during all of the phase two (which was one hour long), which shows that the fibers can operate normally at this temperature. During the third phase ($110°$ C) a significant decrease of the measured charge is observed, which demonstrates a change in the optical properties of the fiber. In the last phase the temperature went back to room temperature and the charge increased but didn't reach the original values, which indicates an unrecoverable damage of the fiber at the $110°$ C temperature.

This test demonstrated that the calibration fibers could be damaged if they are exposed to temperatures above $95°$ C for a long period of time.
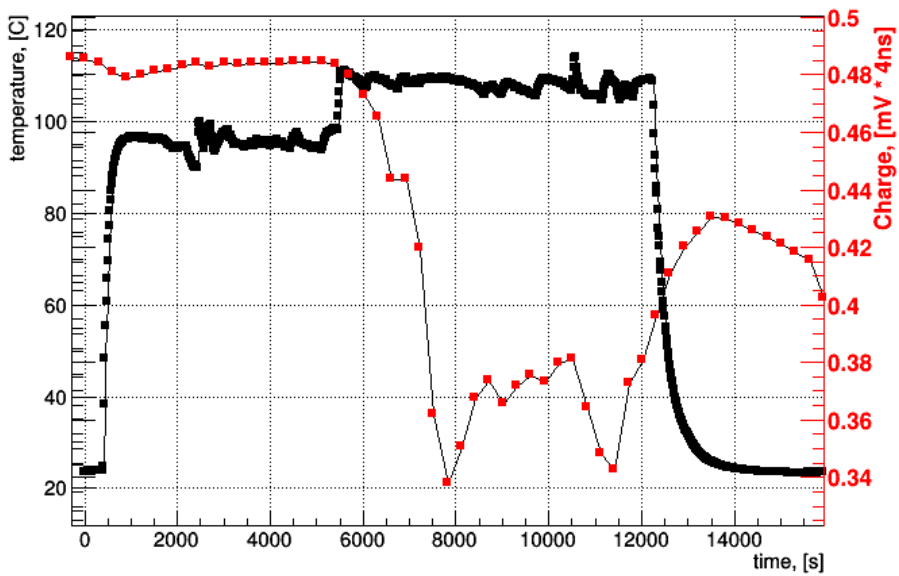
Figure 4.19.: Measurements of the mean of the charge distribution of LED signals which go through a heated fiber bundle. Black points correspond to the temperature of the fiber bundle; red points correspond to the mean of the charge collected in 5 minute intervals.
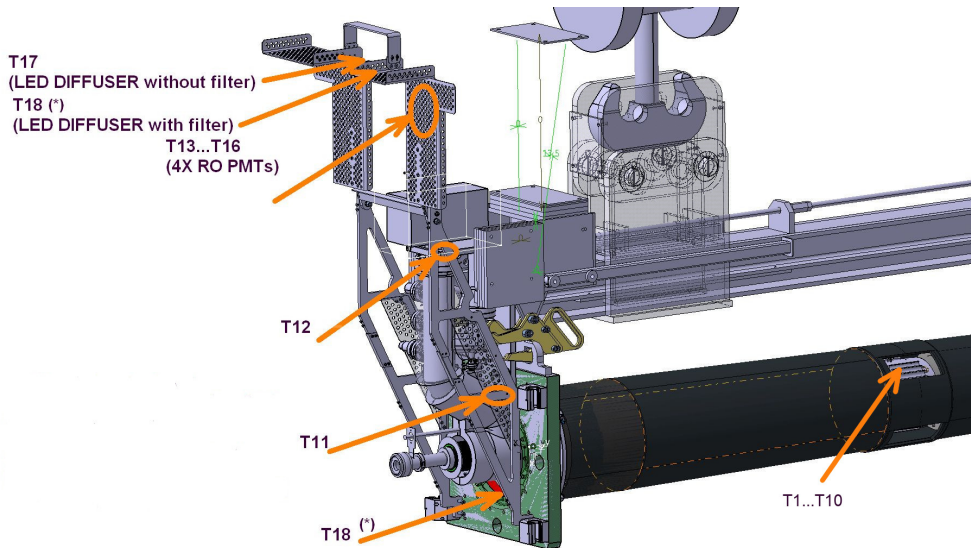
Figure 4.20.: Positions of the temperature probes close to the beampipe flange.

4.3.4. Temperature conditions during the beampipe bake-out and detector operational period

The LUCID detector was equipped with 18 temperature sensors per side which were installed (see Figure 4.20 and Figure 4.21) to monitor the temperature of the detector components during the bake-out procedure of the new ATLAS beampipe and during the detector operation. Temperatures from all sensors were recorded and archived every 10 seconds.

The temperature from the sensor placed in the cable tray and at the beampipe flange during the beampipe bake-out is shown in Figure 4.22. The temperature were well within the safety margin and didn't exceed $40°$ C. The temperature from other sensors didn't exceed $40°$ C either. It demonstrated the high efficiency of the beampipe insulation and the LUCID cooling system, and no damage to the LUCID detector components was done.

After the bake-out procedure had finished the temperature was constantly monitored to make sure that there were no large fluctuations in the cavern. A few sensors were installed close to the PMTs and their measurements can be treated as an approximate temperature of the PMT tubes. The temperature during the data-taking
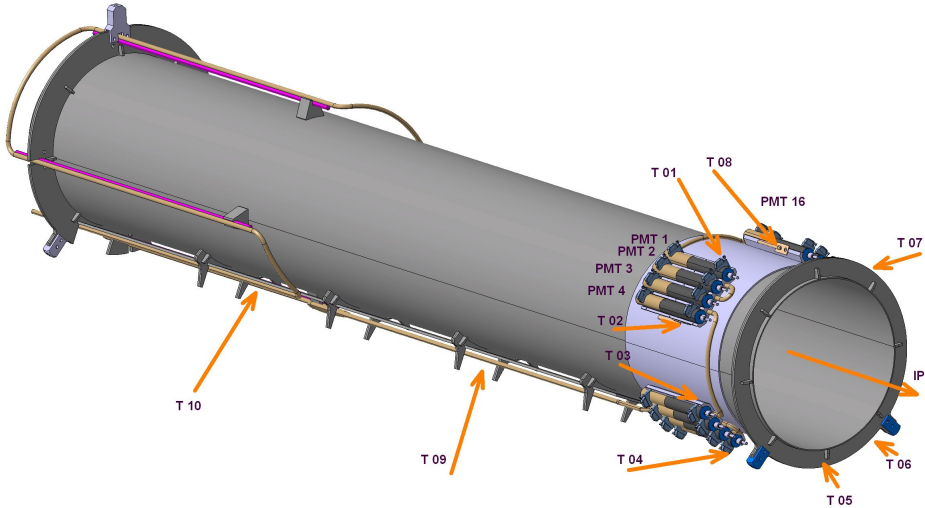
Figure 4.21.: Positions of temperature probes along the LUCID carbon support tube.
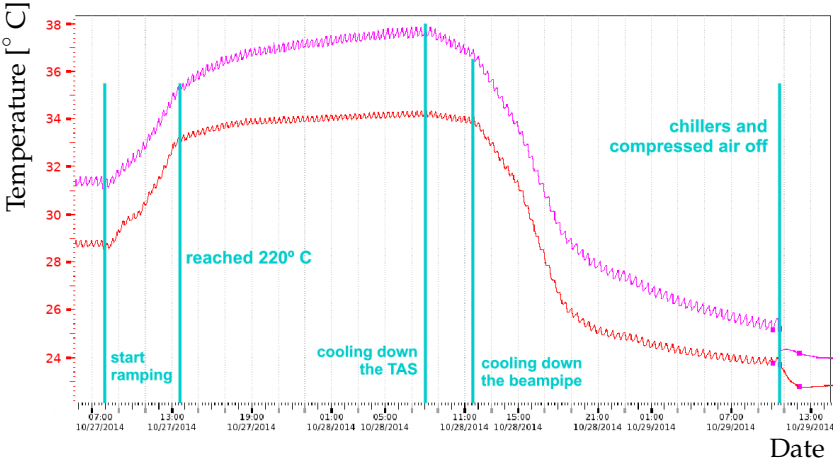
Figure 4.22.: The temperature reading from the temperature probes during the bake-out proce-
dure.
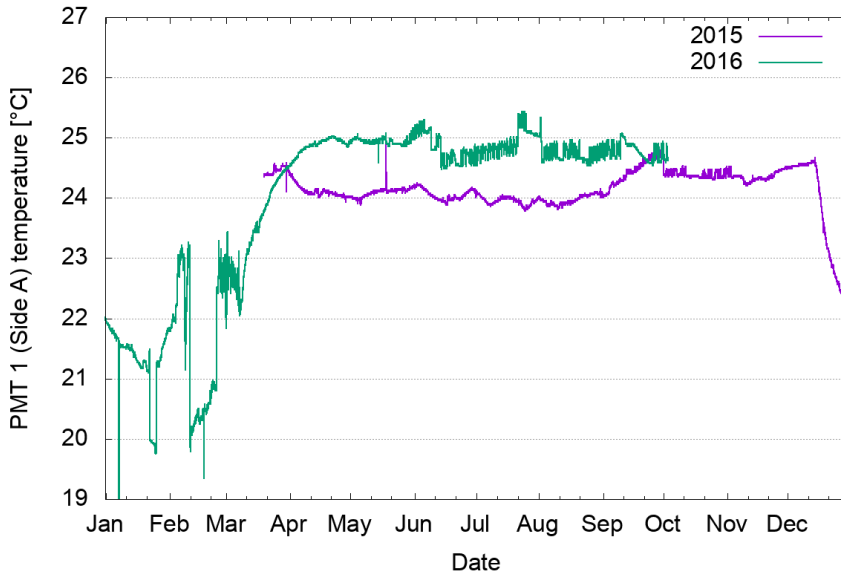
Figure 4.23.: Temperature trending plot recordered by a probe close to one of the Bismuth PMTs during 2015 (purple) and 2016 (green). This plot shows that the temperature is stable in the experimental cavern during physics runs and that fluctuations are smaller than one degree.

periods in 2015 and 2016 are shown in Figure 4.23. There are no significant fluctuations over the entire period and the measurements are all within 1° C. According to the measurements described in Section 4.3.2, the PMT gain dependence as a function of temperature corresponds to 0.25 % per 1° C, which is negligible for the luminosity measurements.

4.4. The LUCID performance and luminosity measurements during 2015

The LUCID detector has different sets of PMTs, which makes it possible for LUCID to provide many independent measurements of the luminosity by different algorithms. The electronics provide luminosity measurements using 124 different algorithms which are based on combinations of signals from different tubes. This section covers topics related to luminosity algorithms, such as a description of different counting

methods, the absolute calibration of the luminometers, the results of the luminosity measurement in 2015 and 2016 and an overview of the main systematic effects and uncertainties.

4.4.1. Luminosity algorithms

The rate of inelastic processes in hard collisions at a collider experiment can be expressed as

$$R_{inel} = \mathscr{L}\sigma_{inel} \tag{4.2}$$

where σ_{inel} is an inelastic cross section and $\mathscr{L}$ is the instantaneous luminosity delivered by the collider. A typical task in particle physics experiments is to measure the cross section of some specific process of interest. The number of collisions observed by the detector in which the process of interest took place during some time period can be expressed as:

$$N_{process} = \int_{t_1}^{t_2} \mathscr{L}\sigma_{process}dt = \sigma_{process}\int_{t_1}^{t_2} \mathscr{L}dt \tag{4.3}$$

where $\mathscr{L}$ is the instantaneous luminosity in equation (4.2). The cross section of the process of interest is then given by:

$$\sigma_{process} = \frac{N_{process}}{\int_{t_1}^{t_2} \mathscr{L}dt} \tag{4.4}$$

To measure the cross section of the process of interest one needs not only to count the number of events where the process took place but also know the luminosity of the dataset. This is true for any type of process. This is why precision measurements of the luminosity is an important task for the experiment. At the LHC, several pp interactions can occur in one bunch crossing. The number of interactions can vary from bunch crossing to bunch crossing but one can make the assumption that this number is Poisson distributed with μ being the average number of interactions per bunch crossing. Taking into account the revolution frequency of the LHC (f_{LHC}) equation (4.2) will transform to

$$\mathscr{L} = \frac{f_{LHC}\mu}{\sigma_{inel}} \tag{4.5}$$

where $\mathscr{L}$ is the instantaneous luminosity in one bunch crossing. Luminometers, used to measure the number of interactions, have a limited efficiency and acceptance, which is why they measure only a visible number of interactions (μ^{vis}), which is a product of the number of interactions and the detector acceptance and efficiency of the method ($\mu^{vis} = \varepsilon\mu$). In the same way it is possible to introduce a visible cross section (σ^{vis}), which is the product of the inelastic cross section and acceptance and efficiency ($\sigma^{vis} = \varepsilon\sigma_{inel}$). One can then write:

$$\mathscr{L} = \frac{f_{LHC}}{\sigma^{vis}}\mu^{vis} \tag{4.6}$$

There are therefore two numbers needed for the luminosity calculation: a visible number of interactions (μ^{vis}) and a visible cross section (σ^{vis}). The first number is measured by LUCID and other luminometers while the latter is measured in special runs which will be described in Section 4.4.2. The number of protons in bunches is different and can vary by up to 20% [57], therefore the number of interactions has to be measured separately for each bunch crossing in event counting measurement. Each bunch pair is identified numerically by a Bunch-Crossing Identifier (BCID) which is set for each of the 3564 possible 25 ns slots in one full revolution of the LHC beams. The LUCID electronics was designed to perform event counting separately for each BCID. Taking this into account the luminosity from all bunch crossings can be expressed as:

$$\mathscr{L} = \frac{f_{LHC}}{\sigma^{vis}}\sum_{j=1}^{n_b}\mu_j^{vis} \tag{4.7}$$

where n_b is the number of colliding bunches and μ_j^{vis} is the average number of interactions in BCID j. Due to the injection process not all slots can be occupied by filled bunches and the maximum possible number of colliding bunches equals to 2808. The luminosity in ATLAS is measured over a certain time period which is called a luminosity block (LB) and is typically equal to one minute.

The LUCID detector can measure the luminosity in three different ways: by counting the number of events, by counting the number of hits or by measuring the total charge collected by the PMTs. When a particle, created in a pp inelastic collision, penetrates the quartz window, a clear signal from the PMT is produced and if it is larger than a specific threshold value it is called a hit. If there is a hit in at least one PMT in the detector, it is called an OR event. As described earlier, LUCID consists of two identical detectors placed on both sides of the interaction point. If there is at

least one hit in the side A (side C) detector, "Event ORA" ("Event ORC") takes place. "Event OR" requires at least one hit in either detectors, while "Event AND" requires at least one hit in both the side A and side C detectors simultaneously. These four combinations are used in the same way by hit counting algorithms where the number of PMT hits is counted instead of the number of events. The LUCID electronics count the number of bunch crossings during one LB in which hits or events are present. If one assumes that the number of pp interactions in one bunch crossing follows Poisson distribution, the probability to observe an event which satisfies the "Event OR" criteria can be expressed as

$$P_{„EventOR"}(\mu_{OR}^{vis}) = N_{OR}/N_{BC} = 1 - e^{-\mu_{OR}^{vis}} \tag{4.8}$$

where μ_{OR}^{vis} is the mean of the distribution, N_{BC} is the number of bunch crossings in a certain BCID during one LB and N_{OR} is the number of bunch crossings (with the same BCID) where "Event OR" took place. One can express μ_{OR}^{vis} as

$$\mu_{OR}^{vis} = -ln\left(1 - \frac{N_{OR}}{N_{BC}}\right) \tag{4.9}$$

In its turn, the probability to observe an event which satisfies the "Event AND" criteria is given by

$$P_{„EventOR"}(\mu_{OR}^{vis}) = N_{AND}/N_{BC} = 1 - (e^{-\mu\varepsilon_{ORA}} + e^{-\mu\varepsilon_{ORC}} - e^{-\mu\varepsilon_{OR}}) \tag{4.10}$$

where $\varepsilon_{ORA}, \varepsilon_{ORC}$ and ε_{OR} are total efficiencies of "Event ORA", "Event ORC" and "Event OR" algorithms accordingly.

As one can see from equation (4.10), there is no analytical solution for μ for "Event AND" algorithms, and it can only be solved numerically.

Luminosity measurements can be used to monitor beam conditions as well. For example, it is useful during the so-called emittance scans when an optimization of beam parameters is made. This requires faster luminosity measurements over shorter periods and that is why LUCID provides an additional set of luminosity measurements every second, called online luminosity. In order to not occupy resources of the central trigger processor (CTP), which distributes the LHC clock to all sub-detectors, online luminosity measurements were implemented in such way that LUCID can provide them by running in standalone mode. In this case the LHC clock signal is not used by the LUCID electronics and a LHC clock emulator is used instead. It means that LUCID
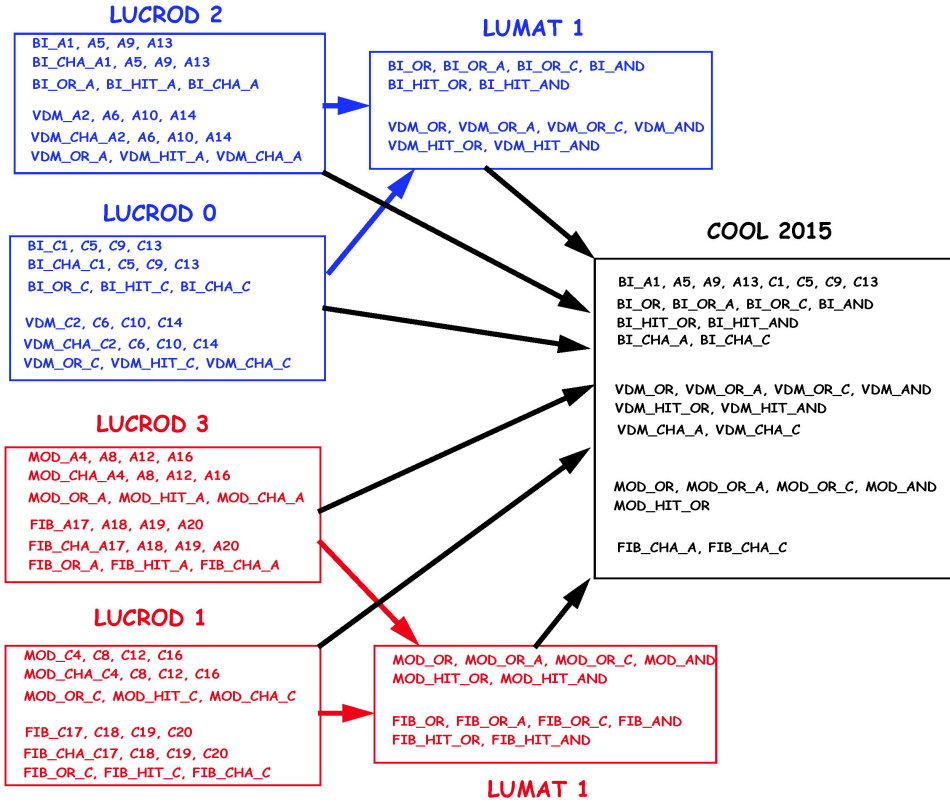
Figure 4.24.: List of luminosity algorithms provided by the LUCID detector in 2015. Only a subset of algorithms are stored in the database.

does not know which BCID slots are occupied by bunches and when they arrive. This is why online luminosity measurements are called BCID blind. In this way LUCID can provide online luminosity even when ATLAS detector does not collect data.

4.4.2. The absolute σ^{vis} calibration

An unknown component in equation (4.6) is the visible inelastic cross section σ^{vis}. This cross section is measured in van der Meer runs where the absolute luminosity is measured directly from the beam parameters [58, 59]. The absolute luminosity for centered colliding beams can be calculated from the transverse proton density
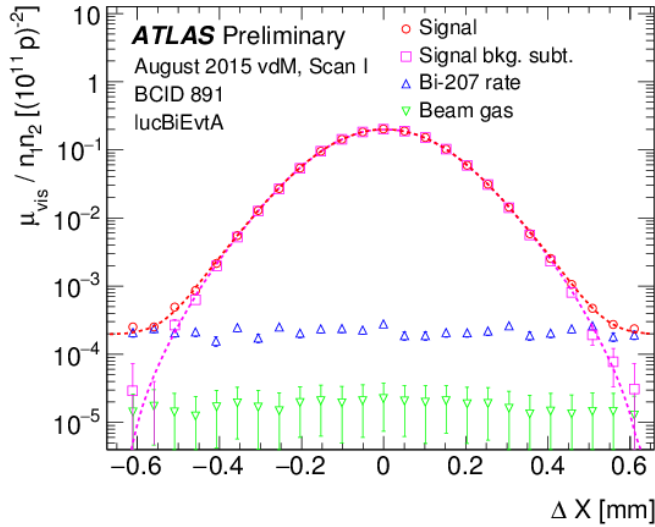
Figure 4.25.: Visible interaction rate for the LUCID algorithm (BI_OR_A) in one bunch crossing and per unit bunch population, versus nominal beam separation during horizontal scan 1 in the August 2015 luminosity-calibration session.

functions of the two beams ($\rho_1(x,y)$ and $\rho_2(x,y)$) as:

$$\mathscr{L} = f_{LHC} n_{p1} n_{p2} \int \rho_1(x,y)\rho_2(x,y)dxdy \qquad (4.11)$$

where n_{p1} and n_{p2} are the numbers of protons in each of the two colliding bunches.

The number of protons in the bunches (which is equivalent to the beam current) is measured a pair of DC current transformers (DCCT) and a pair of fast beam current transformers (FBCT). DCCT is used to measure the total beam current while FBCT is used to measure the relative intensity of individual bunches.

Van der Meer scans are performed by changing the relative position of the beams in one direction while keeping them centered in the other direction. By doing scans in both directions and measuring the interaction rate as a function of the beam separation one can obtain two scan curves (with the widths Σ_x and Σ_y). One such curve, normalized to the number of protons in the beam, is shown in Figure 4.25. The peak luminosity during a van der Meer run can be written as:

$$\mathscr{L}^{peak} = f_{LHC} n_{p1} n_{p2} \int \rho_1(x,y)\rho_2(x,y)dxdy = f_{LHC} n_{p1} n_{p2} \frac{1}{2\pi\Sigma_x\Sigma_y} \qquad (4.12)$$

if there are no correlations between the beams in x and y. By comparing equation (4.6) and equation (4.12) one can show that the visible cross section is equal to:

$$\sigma^{vis} = \frac{2\pi\Sigma_x\Sigma_y\mu_{max}}{n_{p1}n_{p2}} \qquad (4.13)$$

One can then calculate the efficiency of the luminosity algorithm as:

$$\varepsilon = \frac{\sigma^{vis}}{\sigma^{ineal}} \qquad (4.14)$$

Measured visible cross sections and efficiencies for some LUCID luminosity algorithms are given in Table 4.2. All counting algorithms can start to saturate if the number of interactions became large enough. If in all bunch crossings during a LB at least one hit is detected by LUCID (which corresponds to the "Event OR" definition) the ratio $\frac{N_{OR}}{N_{BC}}$ will be equal to 1 and it will be impossible to use equation (4.9) to calculate the number of interactions μ. Thus one can calculate the maximum possible number of interaction, μ_{max}, which different algorithms can deal with without saturation, which corresponds to the case when there is at least one bunch crossings during a LB when a combination of hits, required by a given counting algorithm, was not detected by LUCID. These values are shown in the last column in Table 4.2. However, the statistical error of logarithmic calculations of the number of interactions μ starts to become large at lower values of μ. In Figure 4.26 one can see that the maximum number of interactions per beam crossing for some physics runs in 2016 was higher than 40-45. At this values, the statistical error of the BI_OR_A algorithm exceeds 2%, which is too large of an errors for the physics runs. This is why it was decided to switch to the "HITOR" algorithm, which counts the number of hits in all PMTs per event. It saturates on a similar level as the counting algorithm for a single tube (e.g. "Bi_OR_C9" in Table 4.2).

4.4.3. Calibration strategy during 2015

The purpose of the calibration is to keep the gain of the PMT constant with time. Due to the fact that the luminosity during 2015-2016 is higher than in 2011-2012 the aging

Algorithm	σ^{vis} (mb)	ε (%)	μ_{max}
BI_OR	32.4	40.5	33
BI_OR_A	19.3	24.2	55
BI_OR_C9	6.44	8.0	168
MOD_OR	21.7	27.1	50

Table 4.2.: The result of the vdM calibrations for some of the LUCID luminosity algorithms.
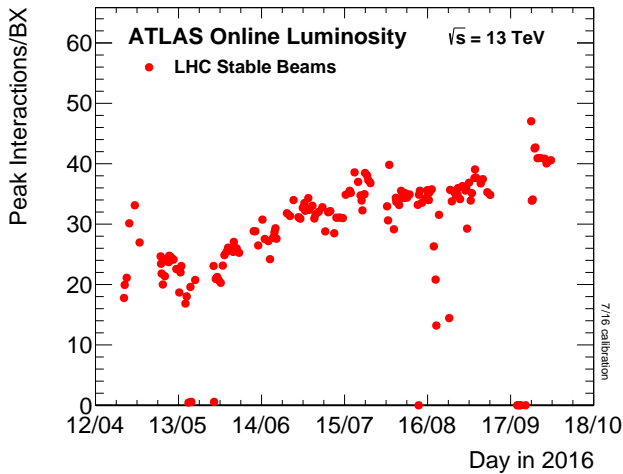
Figure 4.26.: The maximum number of inelastic collisions per beam crossing during 2016 physics runs.

effects become visible already after a few days of beam collisions. The strategy is thus to make calibration runs after each physics run.

To monitor the gain of the BI PMTs, a truncated mean of the charge distribution from the Bi-207 sources was measured in each calibration run. These values directly correlate with the gain of a PMTs. In order to keep the gain of the PMT constant it is enough to keep the truncated mean of the charge distribution constant. Therefore after each calibration run the mean charge of each tube is compared to a reference value and if there is a significant difference a program automatically adjusts the high voltage in order to correct the PMT gain. This procedure was used for 2015 and 2016 and was shown to be highly effective and robust. In Figure 4.27 the high voltage change for Bismuth PMTs during 2016 is shown. Voltage was increased up to 170 V for some tubes.
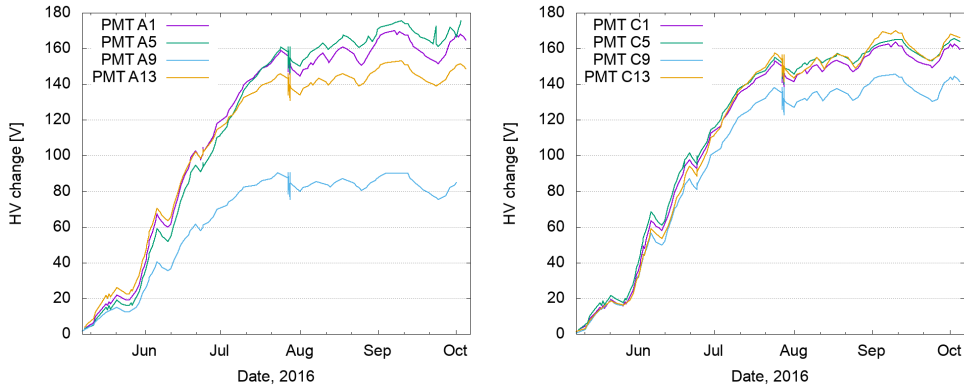
Figure 4.27.: Trending plot of the high voltage change for Bismuth PMTs on side A (left) and side C (right) during 2016.

Despite the fact that BI PMTs were the one used for the luminosity measurements, VDM PMTs were turned on as well in order to study performance of the LED calibration in comparison with Bi-207 ones. The idea of the LED calibration is identical to the Bi-207 source calibration in that the mean charge distribution of the signals from the LED light is used as a handle to control PMTs gain. If one keep this value constant the PMT gain will be kept constant as well. However, studying luminosity measurements provided by the VDM PMTs showed a discrepancy to the BI luminosity as well as with other ATLAS luminometers. Several studies were done to understand the reason for the disagreement. The initial suspected cause of the disagreement was the LED calibration procedure. However, the stability of the LED light is monitored separately by the PIN-diode, which guarantees that the LED provides the same amount of light to the PMTs over a long period of time, which rules out this as a problem in the LED calibration procedure. By studying the number of hits as a function of BCID it was found that VDM PMTs have a significantly larger background than BI PMTs which distorts the luminosity measurements during the physics runs. The cause of this background is not clear but one can suspect that the ferrule connector, which is not present in the BI PMT setup, can provide additional counts, which distort the luminosity measurements.

The laser calibrations were not studied much since the laser source is controlled by the Tile subsystem and require coordination with the Tile sub-detector which makes it more complicated to use.
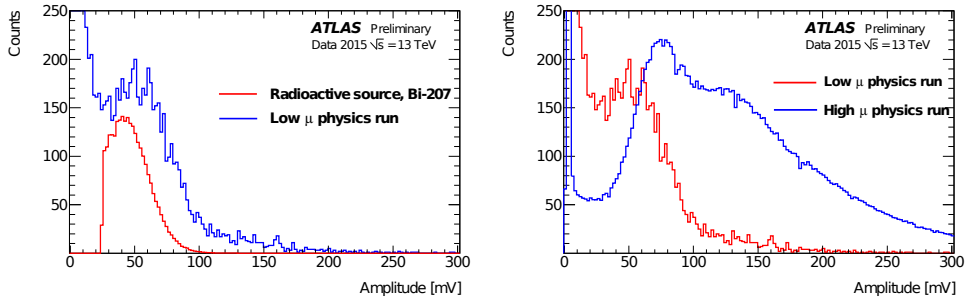
Figure 4.28.: Comparison of the pulseheight distribution in a physics run with low-μ with the same distributions during a Bi-207 calibration run (left) and with distributions during a high-μ physics run.

4.4.4. The first 13 TeV collisions at the LHC

The LHC reported the first 13 TeV *pp* collision in May 2015 and these were duly recorded by ATLAS and other LHC experiments. Starting from that time the new LUCID was succesfully operating and provided information about the luminosity delivered to ATLAS.

The PMT pulseheight distribution in a physics run is shown in the left plot of Figure 4.28 (blue) together with the same distribution during a Bi-207 calibration run (red). In both distributions a peak due to Cherenkov photons is visible. The calibration distribution is cut due to the threshold in the electronics that define a PMT-hit.

In the right plot of Figure 4.28 a comparison of the pulseheight distributions in a physics run with low-μ (red) and high-μ (blue) is shown. The pulseheight is shifted towards higher values when at high luminosity several particles traverse the photomultiplier window in the same bunch crossing. A second peak corresponding to events with two particles going through the PMT window is clearly seen.

LUCID can measure luminosity in many ways, and Figure 4.29 shows a comparison of the luminosity measured by the A and C detectors in different ATLAS data taking runs. The two measurements agree within less than 0.5%.

The left plot of Figure 4.30 shows a measurement of the average number of inelastic *pp* collisions using different ATLAS luminometers, and the right plot shows the ratio of this measurement with respect to a LUCID measurement. The BCM detector
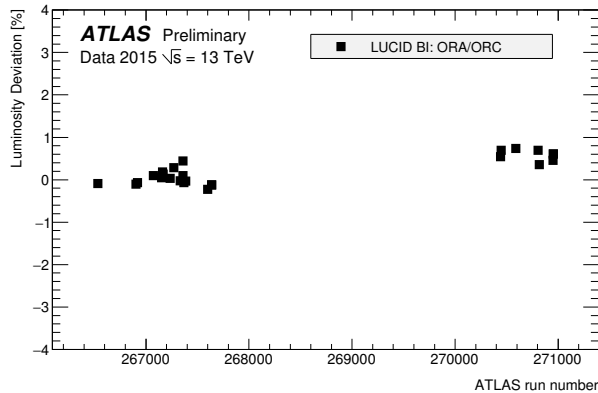
Figure 4.29.: Fractional difference in measured luminosity between the forward (A) and backward (C) arms of the LUCID detector. The agreement between the two LUCID arms is better than 1%.

(described in next section) shows a deviation of up to 2% during this LHC fill but the Tile calorimeter measurements are all in agreement with LUCID to better than 0.5%. The discrepancy with BCM is due to the sensitivity of the BCM counting algorithm and electronics to the bunch train structure. Results shown in Figure 4.30 represent one of the early run with 50 ns distance between bunches. During the first runs with a 25 ns distance between bunches the BCM detector started to show up to 20% difference with respect to other ATLAS luminometers, which led to the decision to not use BCM measurements for the final calculation of the ATLAS luminosity and systematic uncertainty. The discrepancy of the LUCID to the Tile calorimeter luminosity will be described later and was taken into account as a systematic uncertainty. The first month of data taking with the new detector therefore showed that LUCID could measure the relative luminosity with a precision of about 0.5% at low luminosity.

4.4.5. Luminosity measurements in the ATLAS experiment during 2015

During 2015 the preferred luminosity algorithm was using the LUCID BI photomultipliers which were the most stable PMTs due to the gain stability monitoring. Beside the LUCID detector there are other sub-detectors that can provide luminosity measurements. They are:
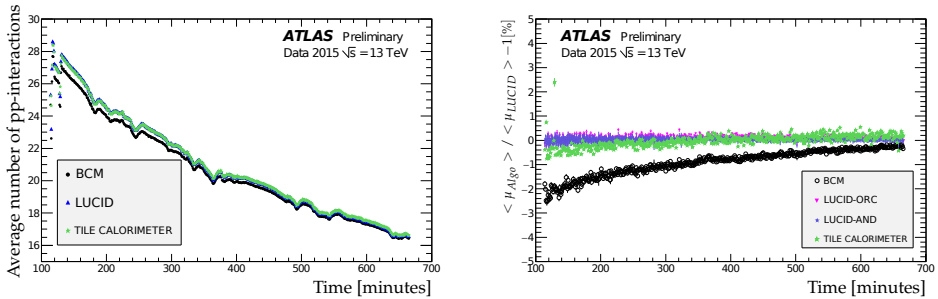
Figure 4.30.: (left) Average number of inelastic proton-proton collisions per bunch crossing during an early 13 TeV fill; (right) Comparison of the measured luminosity by different luminometers in ATLAS with respect to LUCID.

- The beam condition monitor (BCM), consisting of four small diamond sensors (1 cm^2 in cross section) on each side which perform hit counting and provide luminosity on a bunch-by-bunch basis, just like LUCID. It is placed at $|\eta| = 4.2$.

- The Tile calorimeter ,consisting of iron plates and plastic scintillators. Signals from the latter are read by PMTs. Particle flux can be estimated by measuring the current drawn by these PMTs. It can not provide the luminosity for each bunch crossing, only the luminosity summed over all colliding bunches, because the currents are read out only every 10 ms. The calorimeter covers the pseudorapidity range $|\eta| < 1.7$.

- The Electromagnetic end-cap calorimeter (EMEC) and the forward calorimeter (FCAL) cover the pseudorapidity range $1.375 < |\eta| < 3.2$ and $3.2 < |\eta| < 4.9$ respectively. They consist of absorbers with gaps filled with liquid Argon. High voltage is distributed to the gaps by sets of electrodes. The high voltage drops induced by the particle flux is counterbalanced by a continuous injection of electrical current, which is proportional to the particle flux and thereby provide a relative luminosity measurement [63], which is also BCID blind.

- The Inner detector covers $|\eta| < 2.5$ and performs track and vertex reconstructions. The luminosity is measured by counting the number of reconstructed tracks.

- The Minimum Bias Trigger Scintillators (MBTS), which is a scintillator detector designed specially for low luminosity runs (with instantaneous luminosity $\mathscr{L} <$

$10^{33} cm^{-2} s^{-1}$). MBTS covers rapidity range of $2.09 < |\eta| < 3.84$. The measured luminosity is BCID blind and is only used in special runs.

The variety of detectors and methods to measure the luminosity provides a handle to cross-check measurements and estimate systematic errors using the difference in results from different detectors.

As in the case for any other detector, LUCID measurements are monitored constantly by the ATLAS shift crew and on-call experts. Many online checks are implemented to verify that the detector and the electronics conditions are stable and that the quality of the collected data is good. The detector development is still ongoing along with the detector operation because many unexpected new issues can show up. One such case for LUCID was related to the photomultiplier transit time, as described below.

The central trigger processor makes the overall level 1 accept decision and also provides the central ATLAS clock, distributed via the Timing, Trigger and Control (TTC) system to sub-detectors. The time this signal propagates to the different sub-detectors is different. That is why readout electronics have programmable delays which are used to compensate for timing differences, which is the case for LUCID as well. This delay can be used to position the PMT signal inside the 25 ns BCID window. Once this delay was set it was expected that it would be constant and the signal would not move with respect to the time of the BCID. In order to keep the gain of PMTs stable, daily calibrations runs are performed and an automatic high voltage adjustment takes place, as described before. During the 2015 running period the high voltage was increased up to 100V for some PMTs. The increase of high voltage significantly changed the transit time in the PMTs (up to 6 ns). This led to a part of the signal moving outside of the timing window where it was not recorded, which led to a decreasing efficiency of the detector. The problem was different for different photomultipliers. There was one PMT (BI_C9) which was hardly affected. This PMT was therefore used to derive a transit-time correction for the other PMTs. The effect of this correction can be seen in Figure 4.31 where the fractional difference of the ratio of the LUCID measurements to the track counting measurement with and without a transit-time correction is shown. The effect started to become visible in late October 2015, were a 1.5 % drop in the luminosity ratio was observed. The ratio in Figure 4.31 was plotted as a function of high voltage and was fitted by a linear function to the data to obtain the transit-time correction. This correction significantly improved the
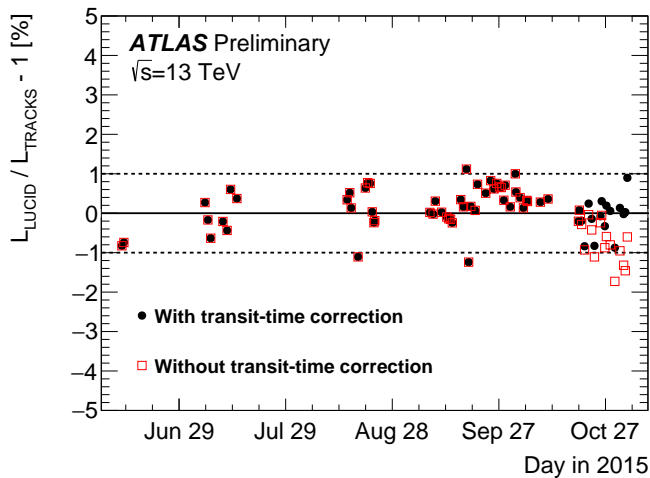
Figure 4.31.: Fractional difference of the measured luminosity per run between LUCID BI_OR_A and track-counting algorithms in 2015. By the end of 2015 the high voltage for some PMTs were changed up to 100 V, which caused a significant change of the transit time of electrons in the PMTs. As a result, part of the signals moved outside the timing windows and in turn decreased the efficiency of the detector. Some PMTs were barely affected and they were used to derive transit-time corrections. The black circles correspond to the LUCID data with these corrections and the red squares without.

consistency of the LUCID data. In order to prevent this effect in the future, a special check was implemented in the LUCID data quality monitor with a program that defines the position of the pulses, and if the peak of the pulse is too close to the BCID border an automatic warning appears to notify the on-call expert that the delay has to be adjusted.

4.4.6. Backgrounds

In order to make correct luminosity measurements one has to be sure that the signals originate only from inelastic proton collisions. Any other signals from other sources are considered a background. The first possible background is the signal from the Bismuth source used in the PMT gain monitoring system. During the design phase one of requirements for the source was that its activity has to be small enough to not significantly affect the luminosity measurements. The effect of the Bismuth source during vdM scans is shown in Figure 4.25. The background is on a permille level
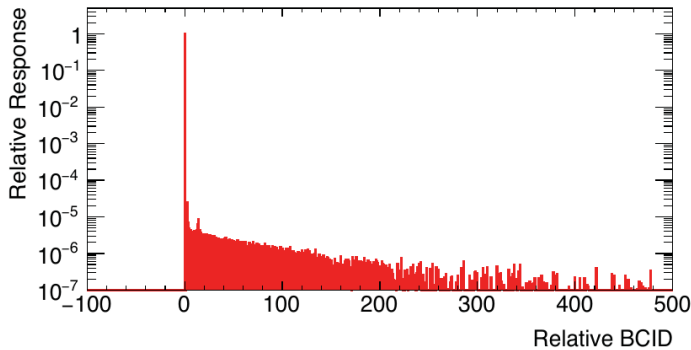
Figure 4.32.: Afterglow background for the LUCID BI_OR_A counting algorithm for single colliding bunches. It it used as a "template" for the so-called template method, which was design to produce an afterglow background estimation for bunch trains with 25 ns distance between bunches.

compared to the signal. The luminosity in typical 25 ns physics runs is 20 times higher with respect to the vdM scans, which makes the effect of the Bismuth source completely negligible during physics runs.

During the Run-1 period it was observed by both the BCM and LUCID detectors that there is some activity detected in the BCIDs immediately following a collision [57, 64] and it was called an afterglow background. It is most likely caused by photons from nuclear de-excitation, which happens because of the hadronic showers from pp interactions which excite detector material [63]. In Run-1, 50 ns bunch trains were used which means that there was one empty bunch slot between filled bunches in the train. This empty slot was used to estimate the afterglow background. 25 ns trains, used in Run-2, do not have empty bunch slots because all slots are filled with bunches, which makes it impossible to use the same approach as in Run-1. For this purpose a so-called template method was invented. The idea is to measure an afterglow "template" using data from single colliding bunches (as shown in Figure 4.32). By assuming that every colliding bunch in the train produces the same afterglow background one can construct templates for each colliding bunch according to the train structure and estimate the total afterglow background caused by the bunch train. As can be seen from Figure 4.32 the maximum rate of the afterglow background for the BI_OR counting algorithm is at the level of 3×10^{-5}. The longest possible train in the LHC can consist of 72 bunches. After detailed studies it was concluded that the total afterglow level is not larger than 10^{-4} compared to the level during collisions and is negligible for physics runs.

4.4.7. Overview of systematic effects in the luminosity measurements

The main approach used by ATLAS to investigate systematic effects is to compare measurements of several luminosity detectors which use different algorithms to measure the luminosity. Different detectors have different acceptance coverage, sensitivity and methods to measure the luminosity, which means different detector behavior and response to pile-up and beam-induced backgrounds.

In Figure 4.33 the ratio of the average number of pp interactions per bunch crossing measured by the Tile Calorimeter to that of BI_OR_A LUCID is shown. Values have been normalized in such a way that the ratio is equal to 1 for the vdM fill. One can observe a clear μ-dependence in both 50 and 25 ns runs. The decrease is equal to 0.1% for one unit of μ for 50 ns runs and is approximately 0.2% for 25 ns runs. A similar dependence has been observed with respect to the track counting algorithm. One of the effects which contribute to the μ-dependence is the assumption that the probability of an individual pp interaction to give a hit (or event) does not depend on the number of interactions in the bunch crossing, which was made during the derivation of equation (4.9). However, in the case of many pp interactions the signals from separate proton collisions which do not provide large enough signal to reach the threshold value can sum up and give a hit. This effect is known as a pile-up (or migration). It is present at some level in any counting algorithm because they rely on the definition of independent hits as a signal exceeding a certain threshold. Algorithms which rely on measurements of values proportional to μ, such as current (charge) from the PMTs or track counting do not suffer from this effect.

Another effect which can contribute to the μ-dependence is related to the LUCID PMT gain decrease. After each physics run the high voltage for the PMTs is changed in order to compensate for the decrease of the PMT gain (see Section 4.2). A test was performed to investigate the PMT gain decrease during the runs. Due to the fact that there is no possibility to monitor PMT gain online during the run the idea was to mimic physics run with the help of LED light by doing many LED calibrations in a row. The mean of the integrated pulse charge distribution as a function of time is shown in Figure 4.34. Every point in the plot corresponds to one LED calibration. This plot represents the PMT gain decrease during a long physics run. The gain is decreasing rapidly in the beginning of the run and later the decrease slows down. Taking this into account as well as the fact that the average μ is slowly decreasing over a run (since the
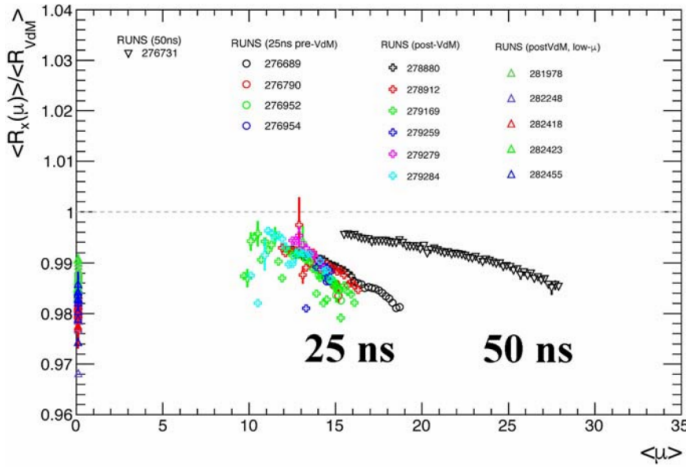
Figure 4.33.: The ratio of measured average μ by the Tile calorimeter to the measurements by LUCID BI_OR_A algorithm. Data is scaled in a way to provide ratio equal to 1 for vdM scan. This figure demonstrates μ-dependence of the LUCID counting algorithm.
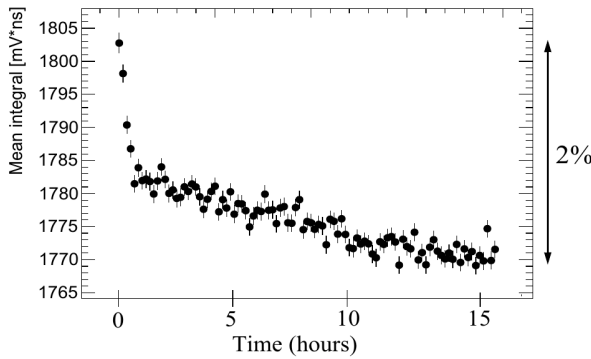
Figure 4.34.: Mean of the charge distribution when pulsing constant LED light as a function of time. The trend represent the change of the PMT gain during the test. The LED setup was used in order to mimic normal conditions during physics run.

number of protons in the beams is constantly decreasing with time) leads to additional contribution to the μ-dependence effect.

Since different runs have different average number of pp interactions or μ, the μ-dependence will create differences in the measured run luminosities from run to run. However, no special systematic uncertainty is assigned to this because these differences will be visible in the run-ro-run luminosity comparison between luminometers and

the estimation of the systematic uncertainty from the run-to-run stability will cover μ-dependence effects as well.

As one can see from Figure 4.33, the ratio of the the average number of pp interactions per bunch crossing measured by the Tile Calorimeter to that of BI_OR_A LUCID is systematically below 1. It means that the calibration constant σ^{vis} (measured in vdM runs for LUCID) is not directly applicable for the high-μ regime, which was the case for 2012 as well [63]. In order to correct for this effect a so-called calibration transfer corrections have to be applied for the LUCID counting algorithms. To estimate this correction for LUCID one can use measurements from calorimeter-based luminometers or track counting. Runs which had both Tile and track counting luminosity available and which happened before the vdM scan were used to made comparisons of the average luminosity for LUCID and track algorithms and to derive corrections from it. Calibration transfer correction was found to be 1.2% for 50 ns and 2.5% for 25 ns runs in 2015. The systematic uncertainty in the calibration transfer was obtained by comparison of four different track selections as well as measurements by the Tile calorimeter and was estimated to be 1.2%.

Additionally one needs to take into account the systematic uncertainty on σ^{vis} itself, determination of which was described previously. The systematic uncertainty was obtained during analysis of the vdM scans and are related to the uncertainty of variables which are used in equation (4.13) to calculate σ^{vis}. Detailed description of the uncertainty estimation of the vdM scans can be found in many notes and papers such as [57, 63–68].

Taking into account all systematic effect of different luminometers one has to choose the preferred detector algorithm to be used as a main algorithm for high-μ runs. For both 2015 and 2016 LUCID Bismuth algorithms were used as main algorithms. In Figure 4.35 the run-to-run stability of measurements from other detectors with respect to the LUCID measurements in 2015 are shown. All luminometers were cross-calibrated in this plot to a LUCID measurement in a reference fill done in the August 2015. The relative variations in measurements of all ATLAS luminometers was found to be within $\pm$ 1.2% during the year.

The list of all systematic uncertainties in the 2015 luminosity measurements with LUCID is shown in Table 4.3. Effect of the background has been found to be negligible, as was described before, thus the systematic uncertainty due to background is estimated to be negligible as well.
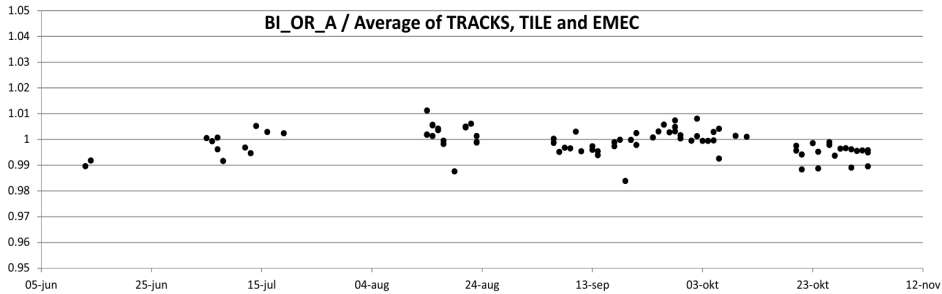
Figure 4.35.: Fractional difference of the measured luminosity per run between LUCID BI_OR_A algorithm and the average of Tile, EMEC and track counting luminosity algorithms in 2015. All luminometers are cross-calibrated with respect to the LUCID measurements in a reference run (used to determine the calibration transfer correction).

4.4.8. Future prospects of the LUCID measurements

As described above, luminosity counting algorithms suffer from a number of unwanted effects. Most of these effects were discovered during the Run-1 operation and the design of the new LUCID detector for Run-2 was aimed to minimize these effects but they still can be observed with the new detector. That is why it was decided to implement the possibility to measure the charge collected by PMTs for each bunch crossing. Charge measurements do not suffer from the migration effect (μ-dependence) and they represent unique luminosity algorithms, because LUCID could make measurements for each BCID, while other ATLAS detectors that exploit charge for luminosity measurements can only provide average values over all BCIDs. Unfortunately, charge luminosity algorithms suffer from other problems. They are far more sensitive to the PMT gain variation than counting algorithms. If the PMT

Source	Uncertainty
Background	< 0.1%
Calibration transfer correction	1.2%
σ_{vis}	1.9%
Run-to-run stability	1.2%
Total	2.6%

Table 4.3.: Sources of systematic uncertainties in the 2015 luminosity measurements with LUCID.

gain decreases by 1% the luminosity measured with the "Event OR C" algorithm will decrease by only 0.2%. For the charge algorithm the same drop of the gain will affect luminosity by 1%. This is why a lot of effort was invested into development of a precise monitoring system with several independent methods, as described in Section 4.2. The PMT gain can decrease by up to a few % during one long physics run (especially for new PMTs), which is why information about the PMT gain change during a physics run would be useful. One possible way to obtain this information can be to pulse the LED light to PMTs in the so-called "forbidden gap" where no bunches are present. Signals from LEDs can then be used in the same way as in the PMT gain monitoring system to estimate the change of the gain. However, PMTs become more stable the more they are exposed to luminosity. This can be seen in Figure 4.36, where one can see that the high voltage corrections applied to correct the PMT gain decrease becomes smaller with more cumulative luminosity. Thus one have to train new PMTs before one use them for luminosity measurements.

Another important aspect is the maximum possible number of interactions which a detector can handle without saturation. During 2016 all LUCID event counting algorithms, which were used in Run 1 and in 2015, started to saturate, and in practice only the "HITOR" algorithm was capable to measure luminosity without saturation. In the future Run 3 μ is expected to be above 100, which will cause saturation of the"HITOR" algorithm as well. One of the possible solutions for Run 3 is to use FIB PMTs. They were installed with the Run 2 detector to make it possible to study their performance. They have two advantages during very high-μ running conditions. Firstly, the PMTs are protected by the muon shielding, which reduce potential problems with radiation damage of the PMTs. Secondly, the bundles of quartz fibers are used as a medium to produce Cherenkov light, which make it easy to choose and change the bundle fiber configuration to obtain the required acceptance of the detector in order to avoid any saturation problems.
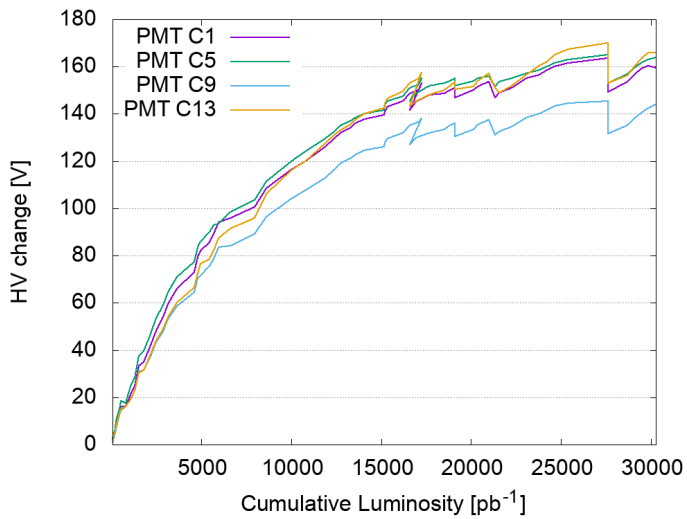
Figure 4.36.: Trending plot of the high voltage change for Bismuth PMTs on side C as a function of cumulative luminosity during 2016.

Chapter 5.

Searches for new physics with same-sign dileptons

5.1. Motivation

Despite the great success of the Standard Model in describing the interactions of the elementary particles, there are a plethora of phenomena which cannot be explained by the SM. Gravity, Dark Energy and Matter, neutrino masses and other observations are not predicted by the SM, which indicates its incompleteness. This is why many studies at LHC experiments are focused on probing the high energy regime to search for new physics, the observation or non-observation of which can support or disprove different extensions of the SM.

Many BSM models predict same-sign dilepton in the final state. It is a very clean signature as few SM processes lead to such a final state. This leads to high sensitivity for new physics.

There are a number of searches in ATLAS which target same-sign dilepton final state signatures, both inclusive ones and searches with additional requirements such as the number of jets or amount of missing transverse momentum [69–71]. The analysis presented here aims to be as model independent as possible and to probe exclusively the same-sign dilepton signature and all the BSM models which predict it.

The signal selection is based on minimal kinematic requirements on leptons. Electrons are clean objects which can be reconstructed with high efficiency in ATLAS. The search observable for the analysis is the same-sign dilepton invariant mass distribution.

If no signal from new physics is found, an upper limit on fiducial cross section for new physics can be set. As an example of a BSM model with the same-sign dilepton final state, the pair production of doubly charged Higgs bosons is studied in detail within the search presented in this thesis.

The analysis searches in three channels: $e^\pm e^\pm$, $\mu^\pm \mu^\pm$ and $e^\pm \mu^\pm$. This chapter will describe the search only for the $e^\pm e^\pm$ channel.

5.2. Background processes

There are four different sources of background which contribute to the signal region. The first source is the so-called prompt background which corresponds to prompt (originating from the primary vertex) same-sign dileptons arising from SM processes. Just a few SM processes have same-sign dileptons in the final state. For example, they can originate from an associate production of $t\bar{t}$ quark pair with vector boson or from production of two vector bosons, where top quarks decay semileptonically and vector bosons decay leptonically. The corresponding Feynman diagrams are shown in Figure 5.1. In general, SM processes with the same-sign dilepton final state have relatively small cross sections at high dilepton invariant mass regions of interest.

The second source comes from wrongful identification of the lepton itself, when a pion or a jet is reconstructed as a lepton, or from leptons which were produced not in the pp collision but from decays of secondary particles, e.g. kaons. This source is called non-prompt or fake background.

The third source comes from the misidentification of the electric charge of the lepton, which makes processes in which an opposite-sign prompt lepton pair is produced contribute to the signal selection as well. The charge misidentification effect becomes significant for high-momentum leptons, when the curvature of the track in the ID is difficult to reconstruct. This source also includes events in which a prompt electron emits a photon due to hard bremsstrahlung. Subsequently the photon creates an electron-positron pair in which one of the two leptons can receive most of the transveerse energy. One lepton from the pair can then form a same-sign electron pair with the original prompt lepton. These two processes are referred to as charge misidentification or charge flip background later in the text.
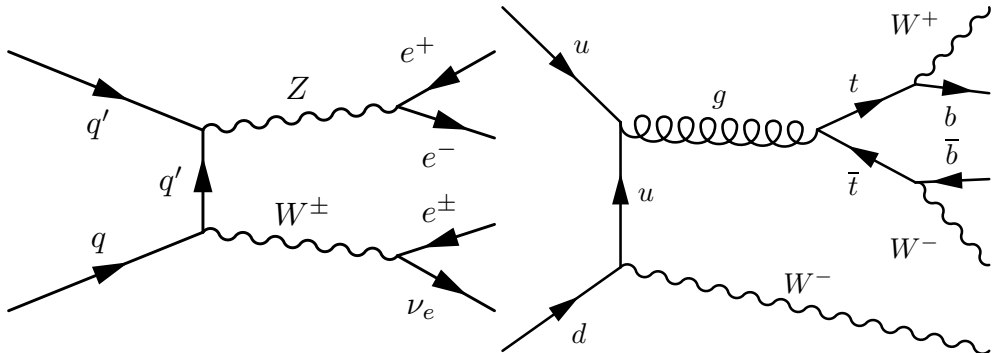
Figure 5.1.: Production diagrams for diboson (left) and $t\bar{t}W$ processes leading to the same-sign dileptons.

The last source arises from $W\gamma$ processes, where an electron-positron pair is created from photon conversion, and by combining with an electron from W decay a same-sign lepton pair can be formed.

Prompt backgrounds are modelled by MC simulations. The contribution from non-prompt backgrounds is derived using a data-driven method, the so-called fake factor method. Charge misidentification and $W\gamma$ backgrounds are estimated from MC simulation as well. However, as will be shown in Section 5.4.1, the electron charge misidentification probability is not properly described by the MC simulation, meaning that a special correction, the so-called charge misidentification scale factor, obtained from the data, is used to correct for this.

The list of all the MC samples used in the analysis is shown in Table 6.1. All listed samples were centrally produced by the ATLAS simulation group. Processes which are not listed in the table do not contribute significantly to the same-sign signal region and are considered negligible. This table summarizes which MC generators and parton distribution function (PDF) sets were used, and shows the perturbative QCD order the cross section calculations were performed to.

Process	Generator + fragmentation/ hadronization	PDF set	Normalization based on
WZ	SHERPA-1.4.1 [47]	CT10 [72]	NLO QCD with MCFM-6.2 [73]
ZZ	SHERPA-1.4.1	CT10	NLO QCD with MCFM-6.2
$W^{\pm}W^{\pm}$	MADGRAPH-5.1.4.8 [74] PYTHIA-8.165 [76]	CTEQ6L1 [75]	LO QCD
$t\bar{t}\,V$, $V = W, Z$	MADGRAPH-5.1.4.8 + PYTHIA-6.426	CTEQ6L1	NLO QCD [77,78]
MPI VV $V = W, Z$	PYTHIA-8.165 [76]	CTEQ6L1	LO QCD
$Z/\gamma^{*}+$ jets	ALPGEN-2.14 [79] + HERWIG-6.520 [46,81]	CTEQ6L1	DYNNLO-1.1 [80] with MSTW2008 NNLO [82]
$t\bar{t}$	MC@NLO-4.06 [83,84] + HERWIG-6.520	CT10	NNLO+NNLL QCD [85–90]
Wt	MC@NLO-4.06 + HERWIG-6.520	CT10	NNLO+NNLL QCD [91,92]
$W^{\pm}W^{\mp}$	SHERPA-1.4.1	CT10	NLO QCD with MCFM-6.2
$W\gamma$	SHERPA-1.4.1	CT10	NLO QCD with MCFM-6.3

Table 5.1.: List of MC generated samples used for background prediction. The used MC generator, the PDF set and the order of the cross section calculations used for the normalization are listed for each sample. The upper part of the table contains MC samples which provide same-sign dilepton in the final state (MPI stands for multiple parton interactions), while the lower part contains samples which contribute to the signal selection due to electron charge misidentification.

5.3. Event selection

The analysis is based on the *pp* collision data collected in 2012 by the ATLAS detector with 8 TeV center of mass energy. The integrated luminosity of the sample corresponds to 20.3 fb^{-1} and the mean number of interactions per bunch crossing was 21.

An event selected for the analysis must have at least one reconstructed vertex with at least three tracks matched to it. If there are several vertices, the one with the highest $\sum p_T^2$, where p_T are transverse momenta of the matched tracks, is chosen. Events should have at least two electron candidates and fire the dilepton trigger, that requires the presence of two electrons with $p_T > 12$ GeV. In order to exclude ambiguities between electron and jet reconstruction, the electrons are required to be isolated. Isolation is calculated by summing up the particle momenta around the electron candidate within a defined cone size, $\Delta R = \sqrt{(\eta_e - \eta_i)^2 + (\phi_e - \phi_i)^2}$, where η_e and ϕ_e are rapidity and azimuthal angle of the electron candidate while η_i and ϕ_i are rapidity and azimuthal angle of track or calorimeter cluster, not related to the electron candidate. Detailed explanations of the isolation and other requirements on electron candidates are given later in this thesis.

5.3.1. Electron selection

The next step is the selection of isolated high-p_T electrons present in the event. Electron reconstruction in the ATLAS detector central region ($\eta < 2.5$) is done by matching tracks from the inner detector with energy deposits in the EM calorimeter. The spatial resolution of the electron candidate in (η,ϕ) plane is taken from the parameters of the matched track, while energy is calculated from energy deposits in the EM calorimeter.

The electrons of interest are well-reconstructed candidates which satisfy the following requirements:

- $p_T > 20$ GeV: to ensure a high and constant trigger efficiency as a function of p_T and to harmonize p_T requirement between the three analysis channels (*ee*, *μμ* and *eμ*)

- $|\eta| < 1.37$ or $1.52 < |\eta| < 2.47$: to be within high-granularity acceptance of the EM calorimeter, but excluding the barrel-end-cap transition region.

- Electron tracks have to originate from the primary vertex. The transverse impact parameter significance which is defined as the ratio of the absolute transverse impact parameter (d_0) to its uncertainty ($\sigma(d_0)$) has to be below three. The distance between the *z*-coordinate of the primary vertex and *z*-position of the point of closest approach of the electron track in the ID to the beamline is required

to be less than 1 mm. These requirements also reject electrons originating from decays of long-lived particles.

- Pass the "tight" electron set of identification criteria. ATLAS defines three sets of reference electron identification criteria designed for use in analyses: "loose", "medium" and "tight". These criteria are designed in a hierarchical way. The background-rejection power is increasing from "loose" to "tight" set at some cost to the identification efficiency. The "tight" set provides a factor of two background rejection power with respect to the "medium" criteria, at the cost of less than 10% electron efficiency [30].

- No reconstructed jet within $\Delta R < 0.4$: to ensure that electron is not part of a jet.

- Pass isolation requirement to distinguish prompt electrons from those associated with jet activity.

The isolation requirement was chosen in order to reach pile-up independent efficiency of more than 99% for electrons with $p_T > 40$ GeV. The requirement has two parts. Firstly, the sum of the transverse energies in the EM and hadronic calorimeters around the electron within $\Delta R < 0.2$, with core electron energy subtracted from the sum, has to be less than 3 GeV $+(p_T - 20 \,\text{GeV}) \times 0.037$ [1], where p_T is electron transverse momentum. Secondly, the sum of the p_T of all tracks with $p_T > 0.4$ GeV within $\Delta R < 0.3$ around the electron track has to be less than 10% of the electron p_T.

Electrons used in the so-called validation regions (VR) defined in Section 5.5, used for validation of the background estimation, are required to fail one or several requirements above but pass a looser one, as will be described further in the text.

5.3.2. Electron pair selection

All the electrons which passed the selection are used in the lepton pair formation step. All combinations are considered, and it is allowed to have more than one pair selected in one event. Electrons in the pair are classified by p_T: the electron with a higher p_T is called leading lepton, while the other one is the subleading lepton. The leading lepton

---

[1] Core electron energy corresponds to the electron energy deposit in the calorimeter in the core cluster, to which electron candidate is assigned. However, not all electron energy is contained in the core cluster, part of it leaks to the neighbor clusters which are used for electron isolation requirement. This effect is taken into account in the isolation requirement formula.

has to pass a stricter cut of $p_T > 25$ GeV, while the subleading lepton has to satisfy $p_T > 20$ GeV as described above.

To avoid low-mass hadronic resonances like J/ψ or Υ showing up in the invariant mass spectrum, only same-sign pairs with $m_{\ell\ell} > 15$ GeV are selected. Additionally, if same-sign lepton pairs with the invariant mass $70 < m_{\ell\ell} < 110$ GeV which corresponds to the Z peak region, are found in the event, the event is discarded. This region is used for estimation of the electron charge misidentification background as described further.

Since more than one pair is allowed in one event, an additional requirement which significantly suppresses the prompt background contribution is required. If an event contains an opposite-sign same-flavour lepton pair which satisfies the condition ($|m_{\ell\ell} - m_Z| < 10$ GeV, where $m_{\ell\ell}$ is the lepton pair invariant mass and m_Z is the mass of Z boson), the event is discarded.

5.4. Estimation of the charge misidentification and non-prompt backgrounds

5.4.1. Prompt opposite-sign dilepton with charge misidentification

Since the charge of one of the reconstructed electrons from the pair can be misidentified, processes with the e^+e^- final state can contribute to the signal region. As the prompt background is relatively small in the signal region, the possibility of a charge misidentification cannot be neglected and has to be precisely estimated. Two cases are considered as a charge misidentification background. The first one is when the electron charge is truly misidentified due to matching of the wrong track to the EM cluster or due to a small curvature of the high-momentum track. The second one arises when an electron emits a photon by bremsstrahlung, which in turn decays to an electron-positron pair. Instead of the original electron, an electron from the photon conversion can be attributed to the pair and can have an opposite charge.

In order to estimate how many events with opposite-sign dileptons contribute to the same-sign dilepton signal region, one has to know the electron charge misidentification rate. It is expected that the charge misidentification depends on the electron
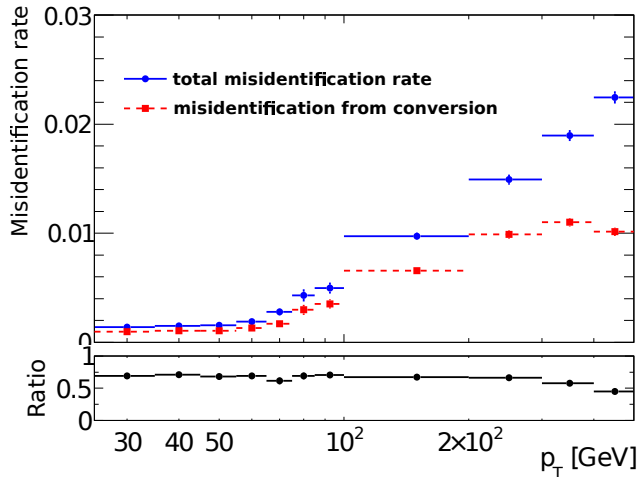
Figure 5.2.: Electron charge misidentification rate, obtained from MC simulation using electrons from Z boson decay. Contribution from charge misidentification due to photon conversion is shown separately on the plot and as a fraction of the total rate in the ratio plot below.

momentum (due to the track curvature) and on η (due to the variation of the detector material with η).

Electrons from Z boson decays provide a huge sample of opposite-sign lepton pairs which can be used to estimate the charge misidentification rate. By applying the signal selection criteria and requiring the invariant mass of the lepton pair to be around the Z mass, $80 < m_{ee} < 100$ GeV, one obtains a pure sample of electron pairs, where the charge of one electron is misidentified. Knowing the number of opposite-sign pairs which pass the signal selection, one can extract the charge misidentification rate.

In Figure 5.2 the charge misidentification rate obtained from MC simulation as a function of p_T is shown. By using generator level information one can distinguish charge misidentification due to photon conversion from other effects as shown in the figure. The contribution from photon conversions from bremsstrahlung dominates the total charge misidentification rate over the entire p_T range except in the high-p_T region, where misidentification of charge due to the very small curvature of the tracks becomes the dominant effect.

To verify the MC estimation of the charge misidentification, a special data-driven technique, the so-called likelihood method, is used in the same way as in Ref. [93].

This method is based on the assumption that charge misidentification rates for different η (p_T) regions are independent. Then one can express the number of same-sign pairs in Z peak region, where one electron is in the region i and another one in the region j, as:

$$N_{SS}^{ij} = N^{ij}(\epsilon_i + \epsilon_j) \tag{5.1}$$

where N^{ij} is the number of all electron pairs and $\epsilon_i(\epsilon_j)$ is the probability of the electron charge misidentification in the region $i(j)$. The number of same-sign pairs, N_{SS}^{ij}, is described by the Poisson distribution if one assumes that all same-sign pairs from Z peak region arise from charge misidentification. By constructing a likelihood function as a product of Poisson probabilities for all possible combinations of i and j regions and making a maximum logarithmic likelihood fit, with ϵ_i and ϵ_i as free parameters, one can obtain misidentification rates for each region.

This method is found to give the most precise estimate as it uses the most of the available statistics and provides kinematically unbiased results for same-sign dilepton analysis with 7 TeV data [33]. Two alternative methods (direct extraction and tag-and-probe methods) use a subset of the available statistics for the rate measurements [94]. The direct extraction method uses only pairs in which both electrons are from the same η (p_T) bin. The tag-and-probe method requires one electron to pass very strict cuts while another one has to pass analysis selection cuts. Meanwhile, the likelihood method uses all pairs which satisfy the signal selection requirements [41].

To cross-check the applicability of the method, it was first applied to reconstructed MC events, and then the charge misidentification rates were compared with those obtained from the generator level information. The comparison demonstrates that the likelihood method provides a very reliable result, as shown in Figure 5.3.

The charge misidentification rate as a function of p_T and η is shown in Figure 5.4 for the MC simulation and the likelihood data-driven prediction. The dependence of the rate on p_T is well described by MC simulation, while some difference is observed in high-η region. This is why η-dependent correction factors were calculated as a ratio of the charge misidentification rate extracted from collision data to the rate predicted by the MC simulation.

The charge misidentification background consists of opposite-sign lepton pairs which were reconstructed as same-sign pairs. The background is estimated from MC
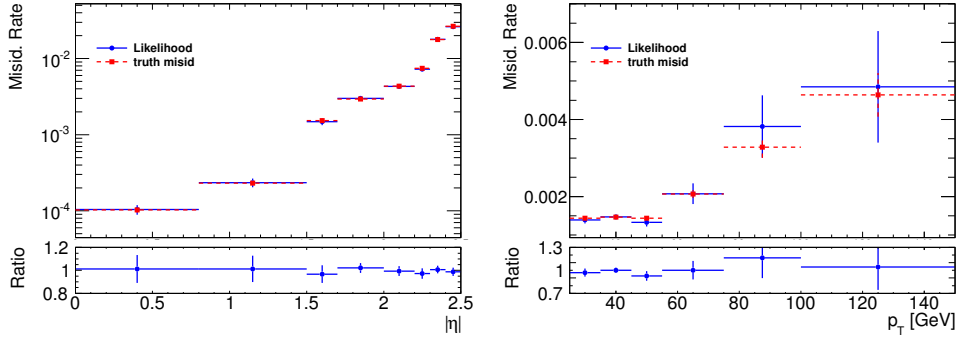
Figure 5.3.: Electron charge misidentification rate, obtained from MC simulation using generator level information and the likelihood method. Ratio between the rate obtained with the likelihood method to the rate obtained with truth MC information is shown below in the ratio plot.
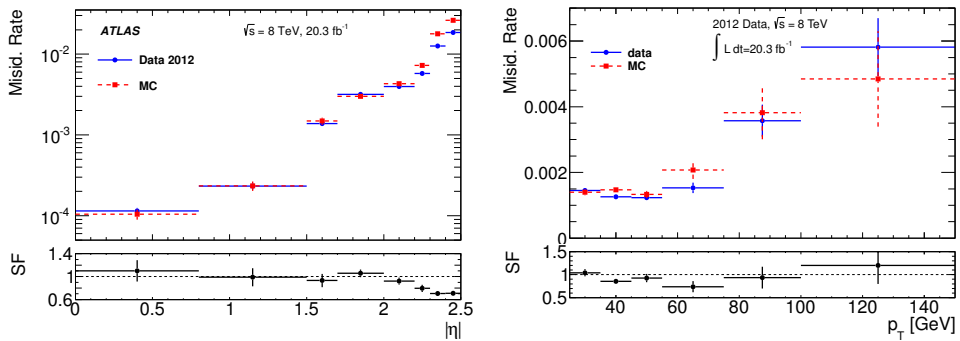
Figure 5.4.: Electron charge misidentification rate, obtained from MC simulation and from real collision data with the likelihood method as a function of $|\eta|$ (lett) and p_T (right). Ratio plot shows charge misidentification scale factor (SF), which corresponds to the ratio between rates from data and MC simulation.

simulation (all the considered processes are shown in the lower part of the Table 6.1) and is corrected by a charge misidentification scale factor to properly reproduce the η-dependence of the charge misidentification rate.

To estimate the systematic error of the derived scale factors, the following uncertainty sources were considered:

- The width of the invariant mass window, used to select electrons from the Z peak, was varied by 10 GeV in both directions. The largest difference between the nominal scale factors and the scale factor obtained from the Z peak window width variation was taken as a systematic error.

- The electron isolation requirement was loosened by 4 GeV in both track- and calorimeter-based isolation criteria.

Electrons from Z decays have a limited p_T-range of up to around 100 GeV. As can be seen in Figure 5.4 (right), the MC simulation describes the p_T dependence of the charge misidentification rate very well, thus it was decided to rely on MC simulation for high-p_T leptons. Additional studies were done to estimate systematic uncertainty in this case. Special MC samples with varied detector alignment and amount of detector material (with variations of 5-20% depending on the sub-detector) were used in order to estimate the effect on the charge misidentification rate. This resulted in an estimate of a 20% error, which was assigned to the high-p_T lepton charge misidentification rate.

The charge misidentification scale factor is also applied for the MC prediction of the background from $W\gamma$ process as the origin of creating a same-sign electron pair is very similar. In this case one electron in the pair originates from the W decay and the other from γ conversion.

The total systematic uncertainty on opposite-sign backgrounds from charge misidentification is 9%, and that on photon misidentificaiton for $W\gamma$ is 13%, making them among the largest single sources of uncertainty, as can be seen in Table 6.2 at the end of this subsection.

5.4.2. Non-prompt background

Another type of background present after the signal selection is the so-called non-prompt background. Main sources of this background are jets misidentified as electrons and electrons which do not originate from the primary vertex, e.g. electrons

from semi-leptonic decays of heavy flavor quarks (b, c). To estimate this background a data-driven method, the so-called fake factor method, is used.

The first step of the method is to define a background region which does not overlap with the signal region, in which the contribution of non-prompt electrons is dominant, while the contribution from prompt electrons is minimal. Events in this region must contain exactly one reconstructed electron (probably a jet misreconstructed as electron) with $p_T > 20$ GeV. To counterbalance the electron, a jet in the opposite azimuthal direction ($\Delta\phi(e, jet) > 2.4$) is required. By requiring strictly one electron one can make sure that the background region does not overlap with the signal selection and processes like Drell-Yan and $t\bar{t}$ will be suppressed. To make sure that the jet and the non-prompt electron are well balanced in terms of energy, the jet is required to have $p_T > 30$ GeV. To suppress contributions from W boson production, a requirement on the transverse invariant mass of $m_T < 40$ GeV is applied [2].

In this background region the fake factor f is defined as:

$$f = \frac{N_P - N_P^{prompt}}{N_F - N_F^{prompt}} \tag{5.2}$$

where N_P is the number of reconstructed electrons in the background region which pass the electron signal selection described above in Section 5.3.1, and N_F is the number of electrons which do not fulfill the signal electron selection requirements but satisfy a looser selection. This looser selection is identical to that for the signal selection, except that the electron only has to satisfy medium electron identification criteria instead of the tight ones, and it has to fail the calorimeter- or track-based isolation criterion. N_P^{prompt} and N_F^{prompt} are the numbers (obtained from MC simulation) of real prompt leptons which pass the signal and looser selections respectively. The contribution of prompt leptons has to be subtracted in order to make sure that the fake factor is evaluated as a ratio of non-prompt electrons that passed the signal selection to the number of non-prompt electrons that passed the looser selection and there is no contamination from real prompt leptons. The fake factor measured in this way can then be used to predict the non-prompt background in the signal region. In order to take into account possible different kinematics of a lepton in the region where the fake factor was derived and the region were it will be applied, the fake factor is measured

---

[2] $m_T = \sqrt{2 p_T E_T^{miss}(1 - \cos \varphi_{\ell\nu})}$, where p_T is the transverse momentum of the electron, E_T^{miss} is the missing transverse momentum of the event and $\varphi_{\ell\nu}$ is the angle in transverse plane between electron direction and direction of the missing momentum.

as a function of electron p_T and η. The total number of non-prompt same-sign pairs, N_{NP}, in the signal region can be estimated as:

$$N_{\mathrm{NP}} = \sum_i^{N_{P_l F_s}} f_s(p_{\mathrm{T}i}, |\eta_i|) + \sum_i^{N_{F_l P_s}} f_l(p_{\mathrm{T}i}, |\eta_i|) - \sum_i^{N_{F_l F_s}} f_l(p_{\mathrm{T}i}, |\eta_i|) \times f_s(p_{\mathrm{T}i}, |\eta_i|). \quad (5.3)$$

The first term corresponds to the number of electron pairs ($N_{P_l F_s}$) where the leading electron (denoted by "l") passes selection criteria (P_l) and the subleading electron (denoted by "s") fails to fulfill it (F_s) but passes the looser selection used for the fake factor calculation. The contribution of every such pair to the signal region is scaled by the fake factor $f_s(p_{\mathrm{T}i}, |\eta_i|)$, where $p_{\mathrm{T}i}$ and η_i are the transverse momentum and pseudorapidity of the subleading electron of a pair which fails the signal selection. Similarly, the second term represents the number of pairs where the leading electron fails the signal selection while the subleading one passes it. The last term corresponds to the case in which both the leading and subleading electrons fail the signal selection. This term has to be subtracted to correct for the double counting of non-prompt electron pairs.

To estimate the systematic errors of the method one can test all the assumptions made and take into account possible differences between the region used to derive fake factors and the region in which they are applied. The following sources were considered:

- statistical uncertainty of the data sample used to derive fake factors;

- prompt MC subtraction, which is done to verify that there is no contamination from prompt leptons when deriving/applying fake factors. Due to the luminosity uncertainty of 2.8% and the uncertainty of MC cross section (7% on major prompt processes), the prompt MC subtraction was varied by a conservative value of 10%;

- requirement on the p_T of the jet balancing the lepton. Results were recomputed with it raised to 50 GeV in order to test the dependence of the fake factor on kinematics of the jets faking electrons;

- difference in the non-prompt background composition in the region used to derive the fake factors and the region where they were applied. Non-prompt background can originate from jets which were created by gluons or light quarks as well as from heavy flavour jets. The fake factor depends on the proportion of

these two categories of jets in the region. Therefore the fake factors were derived separately for heavy and light flavour jets, and the difference between the results was taken as systematic error.

A more detailed description of the evaluated systematic uncertainties and the fake factor method can be found in [33].

The electron fake factor as a function of electron p_T together with the statistical and systematic errors is shown in Figure 5.5.
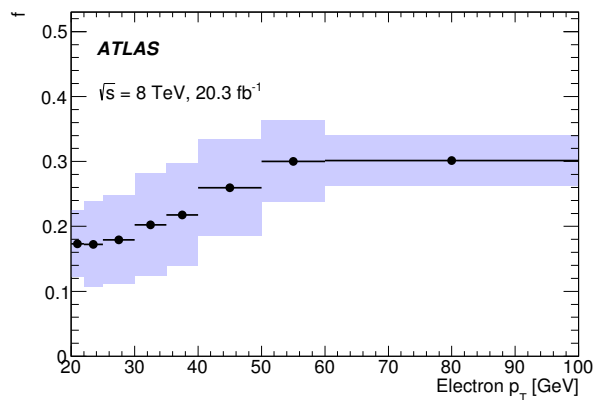
Figure 5.5.: Electron fake factor f as a function of electron p_T. Combined statistical and systematic errors are shown as shaded areas.

Verification of the fake factor method is done with the help of validation regions (VR) which will be described in Section 5.5.4.

5.5. Background validation regions

In order to make sure that all backgrounds are modelled/predicted correctly in the signal region, one can define and use special validation regions. These regions should be kinematically close to the signal region but should not overlap with it. The first validation region tests the overall normalization of the background prediction to data. Other described regions are designed to test one given background type at a time, which means that one background type is dominant over all others.

5.5.1. Prompt opposite-sign dileptons

The first validation region is defined by using exactly the same event selection as for the signal region, but requiring the two leptons to have opposite charges. This validation region does not test any specific background. The MC-based background estimation is normalized only to the luminosity of the data sample, and hence verifies that trigger and lepton reconstruction efficiencies are well modelled. The correct description of the Z peak shape in data by the MC simulation tests electron energy scale and resolution. In Figure 5.6 the invariant mass of opposite-sign electron pairs is shown. Table 5.2 gives the observed and the expected number of the electron pairs. Good agreement between data and simulation is observed.

Process	Number of electron pairs
Drell-Yan	4700000 ± 330000
$t\bar{t}$	14580 ± 870
Dibosons	12210 ± 540
Non-prompt	8320 ± 240
$W\gamma$	243 ± 35
MPI	33 ± 33
Total expectation	4730000 ± 330000
Observation in data	4895830
Agreement	$-0.48\,\sigma$

Table 5.2.: Observed and expected number of lepton pairs for the control region with opposite-sign, isolated leptons. Agreement between the observed and the expected number of pairs is quoted in the bottom of the table as a fraction of the total uncertainty on the prediction.

5.5.2. Prompt same-sign dileptons

The same-sign dilepton prompt background originates predominantly from WZ and ZZ processes, where both Z and W bosons decay leptonically. In order to check the normalization of these processes, a dedicated validation region is used. In a fully reconstructed event in which one of these processes took place, one can find at least
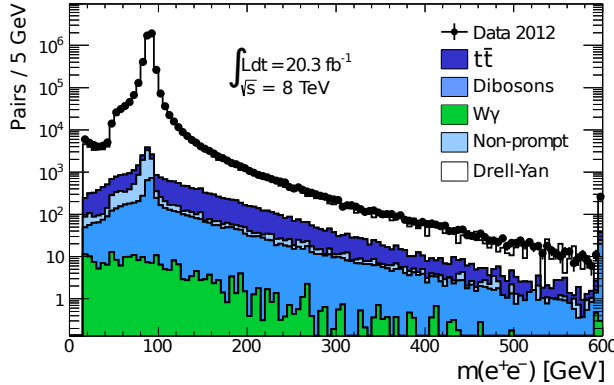
Figure 5.6.: Invariant mass of the opposite-sign electron pairs that passed signal selection. The data is shown as closed circles. The stacked histograms represent the background estimations. The last bin is an overflow bin.

one same-sign and one opposite-sign lepton pair. In order to enhance the WZ and ZZ contributions in the validation region, at least three leptons are required in the event, where one lepton pair has to be a same-sign electron pair and the other one – an opposite-sign same-flavour pair (from Z boson decay). The invariant mass of the opposite-sign pair has to be within 10 GeV of the Z boson mass.

The expected and observed numbers of same-sign pairs in this region are listed in Table 5.3, and the ratios between them are shown in Table 5.4. The expectations are in good agreement with the observation.

Sample	Number of electron-electron pairs with $m(e^{\pm}e^{\pm})$						
	> 15 GeV	> 100 GeV	> 200 GeV	> 300 GeV	> 400 GeV	> 500 GeV	> 600 GeV
Non-prompt	49 ± 14	31.1 ± 8.1	11.1 ± 3.0	3.4 ± 1.3	1.22 ± 0.72	0.81 ± 0.63	0.41 ± 0.44
Prompt total	226 ± 18	133.8 ± 9.2	36.7 ± 3.0	11.6 ± 1.3	3.44 ± 0.63	1.15 ± 0.34	0.38 ± 0.18
W/γ	0.0 ± 0.0	0.0 ± 0.0	0.0 ± 0.0	0.0 ± 0.0	0.0 ± 0.0	0.0 ± 0.0	0.0 ± 0.0
Charge Flip total	0.00036 ± 0.00068	0.0 ± 0.0	0.0 ± 0.0	0.0 ± 0.0	0.0 ± 0.0	0.0 ± 0.0	0.0 ± 0.0
Sum of Backgrounds	275 ± 23	165 ± 12	47.9 ± 4.2	15.0 ± 1.9	4.65 ± 0.95	1.96 ± 0.71	0.78 ± 0.47
Data	268 ± 16	156 ± 12	46.0 ± 6.8	14.0 ± 3.7	6.0 ± 2.4	3.0 ± 1.7	1.0 ± 1.3

Table 5.3.: Expected and observed numbers of pairs for various cuts on the dilepton invariant mass. The uncertainties shown are quadratic sums of the statistical and systematic uncertainties.

Figure 5.7 shows the invariant mass distribution in the prompt validation region. As was mentioned above, the invariant mass $70 < m_{\ell\ell} < 110$ GeV region has been

Ratio between observed and expected for $m(e^{\pm}e^{\pm})$						
> 15 GeV	> 100 GeV	> 200 GeV	> 300 GeV	> 400 GeV	> 500 GeV	> 600 GeV
0.97 ± 0.09	0.95 ± 0.10	0.96 ± 0.17	0.93 ± 0.27	1.3 ± 0.6	1.5 ± 1.0	1.3 ± 1.9

Table 5.4.: Ratio between observed and expected same-sign pairs in the WZ and ZZ control region for various cuts on the dielectron invariant mass. The uncertainties account for both statistical and systematic errors.

excluded to be used for the estimation of the electron charge misidentification background. The simulation agrees well with data.
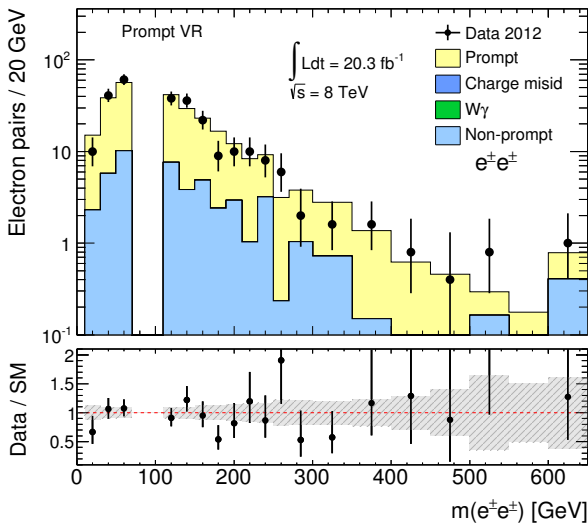
Figure 5.7.: Invariant mass of reconstructed same-sign electron pairs in the prompt background validation region. The last bin is an overflow bin.

5.5.3. Electron charge misidentification

As was described above, events with opposite-sign lepton pairs in the final state can be reconstructed as same-sign lepton pairs, if the charge of one of the leptons was wrongly identified. Misidentification probability is well modelled as a function of p_T by MC simulation, but η-dependence has to be corrected by scale factors obtained with a data-driven method. One can make a sanity check, comparing data from a Z

peak window (same-sign pairs with invariant mass $80 < m_{ee} < 100$ GeV) with MC simulation corrected by the charge misidentification scale factors.

The invariant mass of the same-sign pairs within the Z peak window is shown in Figure 5.8. The p_T and η distributions for the leading electron are shown in Figure 5.9. A good agreement is observed between the data and MC expectations, which demonstrates correctness of the derived charge misidentification scale factor.

The observed and the expected numbers of electron pairs are also shown in Table 5.5 for all same-sign electron pairs and separately for positively and negatively charged pairs.
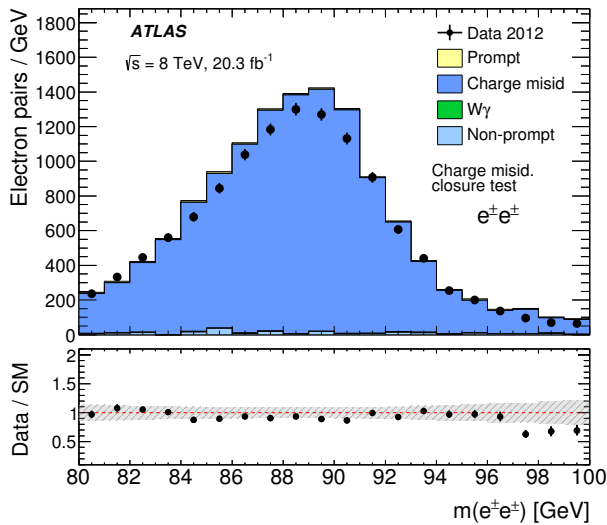
Figure 5.8.: Invariant mass of reconstructed same-sign electron pairs in the validation region for the charge misidentification background prediction. The dominant background contribution arises from electron charge misidentification.

5.5.4. Non-prompt background validation region

To verify the fake factor method, a set of validation regions is checked. These regions have to be as close as possible kinematically to the nominal signal selection as well as to the looser signal selection, which is used in non-prompt background estimation with equation (5.3).

Process	Number of ee pairs
Same-sign ee Z mass window.	
Non-prompt	200 ± 110
Charge Flips	12400 ± 1300
Prompt Electrons	143.4 ± 8.1
$W\gamma$	26.8 ± 5.6
Total Prediction	12700 ± 1300
Data	11793 ± 110
Agreement	$0.8\,\sigma$
Same-sign e^+e^+ Z mass window.	
Fakes	66 ± 60
Charge Flips	6380 ± 670
Prompt Electrons	82.0 ± 5.0
$W\gamma$	17.5 ± 4.0
Total Prediction	6540 ± 680
Data	5908 ± 77
Agreement	$1.0\,\sigma$
Same-sign e^-e^- Z mass window.	
Fakes	131 ± 63
Charge Flips	5990 ± 630
Prompt Electrons	61.4 ± 3.9
$W\gamma$	9.4 ± 2.3
Total Prediction	6190 ± 630
Data	5885 ± 77
Agreement	$0.5\,\sigma$

Table 5.5.: Observed and expected numbers of lepton pairs for the control region with same-sign, isolated electrons falling inside the Z mass window. The uncertainties of the predictions are combined statistical and systematic ones. Agreement between observed and expected number of pairs is quoted as a fraction of the total uncertainty on the prediction.
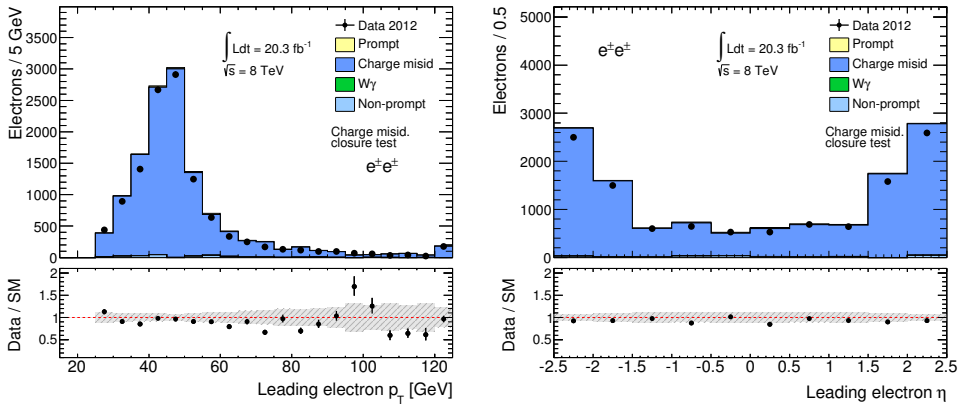
Figure 5.9.: Leading electron p_T (left) and η (right) distributions in the charge misidentification validation region. The last bin is an overflow bin in the left figure.

Two validation regions were defined, shown in dark blue in a schematic representation in Figure 5.10. Both regions are identical to the nominal signal selection (shown in red) except with either a weaker identification requirement (denoted as "VR1"), or a weaker isolation cut ("VR2"). Looser selections for the validation regions which were used for fake factor calculation are shown as well in lighter blue. Such a design of the validation regions provides similar kinematics to the one in the signal region.
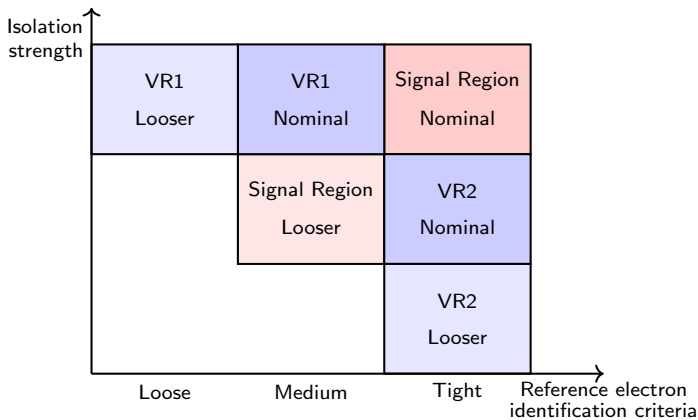
Figure 5.10.: Schematic representation of the kinematic phase space of non-prompt validation regions with respect to signal region.

However, requirements of the VR1 and VR2 regions can be applied either to both electrons in a pair or only to one. Thus, in total four different validation regions are used:

- "Medium electron identification" VR. Corresponds to VR1, when both electrons pass medium identification criteria.

- "Weak isolation on both leptons" VR. Corresponds to VR2, when both electrons pass weaker isolation criteria compared to the signal one [3].

- "Weak isolation on subleading electron" VR. Corresponds to VR2, when only the subleading electron from a pair passes medium identification criteria, while the leading one passes the signal isolation requirement.

- "Weak isolation on leading electron" VR. Corresponds to VR2, when the leading electron from a pair passes medium identification criteria, while the subleading passes the signal isolation requirement.

Figure 5.11 and Figure 5.12 show the invariant mass distributions for the validation regions described above. The agreement between observation and prediction is generally good. Table 5.6 shows the expected and the observed numbers of electron pairs. The uncertainties quoted are statistical only.

Validation region	Fakes	Prompt	Charge Flip	$W\gamma$	Total Pred	Data	Agreement
Medium electron identification	111.04 ± 27.4	2.9 ± 0.5	72.46 ± 16.75	8.78 ± 2.3	195.18 ± 32.2	217 ± 15	$-0.62\,\sigma$
Weak isolation on both electrons	252.9 ± 133.64	1.23 ± 0.3	29.07 ± 10.1	0.27 ± 0.28	283.47 ± 134.02	285 ± 17	$-0.01\,\sigma$
Weak isolation on subleading electron	519.21 ± 120.72	32.88 ± 2.14	52.69 ± 14.87	17.64 ± 4.32	622.42 ± 121.72	574 ± 24	$0.39\,\sigma$
Weak isolation on leading electron	154.97 ± 58.67	13.28 ± 1.21	15.96 ± 7.5	5.12 ± 1.72	189.33 ± 59.19	224 ± 15	$-0.57\,\sigma$

Table 5.6.: Expected and observed numbers of electron pairs for the different same-sign *ee* fake control regions. The uncertainties on the predictions include the statistical and systematic uncertainties (fake factor and charge misidentification uncertainties have been included; other systematic uncertainties are negligible in these regions). Agreement between observed and expected number of pairs is quoted in the last column of the table as a fraction of the total uncertainty on the prediction.

---

[3]"weaker isolation criteria" corresponds to requirement of the sum of the transverse energies in the EM and hadronic calorimeters around the electron within $\Delta R < 0.2$ to be less than 7 GeV $+(p_T - 20$ GeV$) \times 0.037$. While signal requirement is 3 GeV $+(p_T - 20$ GeV$) \times 0.037$
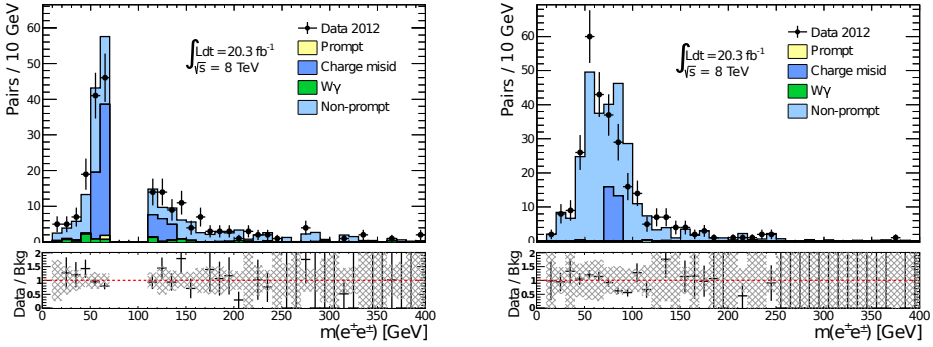
Figure 5.11.: Invariant $e^{\pm}e^{\pm}$ mass distribution plots of prediction and data in the VR with both electron passing medium electron identification criteria (left) and in the VR passing weaker isolation (right). The hatched areas show the statistical uncertainty of the background prediction.
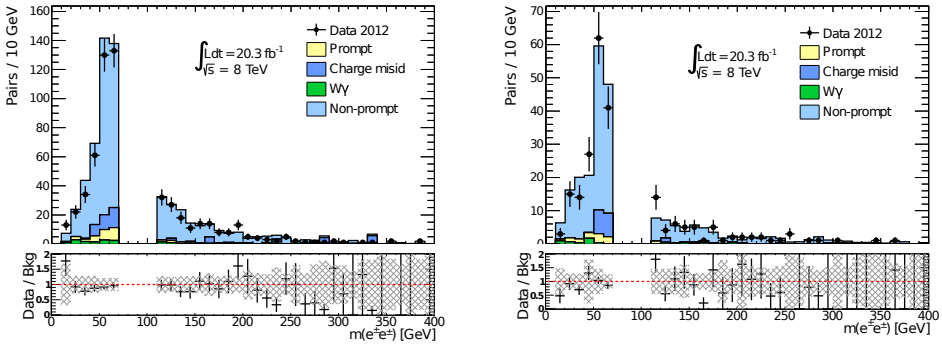
Figure 5.12.: Invariant $e^{\pm}e^{\pm}$ mass distribution plots of prediction and data in the VR with subleading electron passing weaker isolation (left) and in the VR with leading electron passing weaker isolation (right). The hatched areas show the statistical uncertainty of the background prediction.

5.6. Systematic Uncertainties

A set of possible systematic sources which can affect background predictions were studied. These sources are presented below. Systematic uncertainties related to the data-driven methods for non-prompt and charge misidentification background estimations were described already in Section 5.4.2 and Section 5.4.1, respectively.

5.6.1. Electron reconstruction

Several systematic uncertainties are related to the electron reconstruction procedure. These uncertainties are provided by the ATLAS e/gamma working group which studies the electron and photon identification performance of the ATLAS detector. They provide recommendations and uncertainty estimations for all physics analyses which use electron or photon final states.

Electron reconstruction and tight identification criteria efficiencies are obtained with the so-called tag-and-probe data-driven method. This method allows one to measure from data the efficiency of a studied electron selection using $Z \rightarrow ee$ and $J/\psi \rightarrow ee$ resonance decays. One electron from a pair is selected by requiring very strict criteria, while the second one is required to pass the selection in the analysis. By counting the number of pairs from the resonance decays (by fitting the invariant mass resonance peak) which were selected or were rejected due to the cut one can extract the efficiency. Detailed information on the method can be found, for example, in Ref. [95]. The reconstruction efficiency uncertainty range is between 1.3-2.4% depending on η, while the tight identification criteria efficiency uncertainty range is between 2.0-2.8% depending on both p_T and η [96].

Reconstruction of the electron energy is optimized using multivariate algorithms. The electron energy scale and energy resolution are obtained using electrons from Z boson decays. Their uncertainties are provided as a function of p_T and η [97] by the e/gamma working group as well.

The total effect of these uncertainties on the total background prediction is shown under the name "Electron reconstruction and identification" in Table 6.2.

5.6.2. Trigger and luminosity

The electron trigger efficiency varies with p_T and η and is measured with respect to the offline identification. This uncertainty is estimated by the ATLAS trigger group.

To scale the background prediction obtained with MC simulation to the data one has to know the integrated luminosity of the collected data sample. Therefore the luminosity uncertainty propagates to all the backgrounds measured using MC simulation. The uncertainty on the total integrated luminosity in 2012 is equal to 2.8% [57] and it was obtained in a similar way to that described in Section 4.4.

5.6.3. Statistics and theoretical cross section

The limited number of simulated events in the Monte Carlo samples leads to additional uncertainty which is listed as "MC statistics" in Table 6.2. This uncertainty also includes the effect of the limited number of events in data sets used in data-driven methods to measure the charge misidentification rate and the fake factor. The statistical uncertainty is significant in the high-mass region.

As one can see from Table 6.1, different processes were simulated using different MC generators, PDF sets and level of perturbative higher order calculations. Additional uncertainty arises from their choice. To estimate these uncertainties, different MC generators, parton showers and hadronization models are tested. Uncertainties resulting from the choice of PDF and the value of the strong coupling constant α_s are estimated by using different PDF sets following recommendations from [98]. Also renormalization and factorization scales are varied by a factor of two to estimate the effect on the cross section and the selection efficiency. The summary list of uncertainties used in the analysis is shown in Table 5.8. Detailed information about cross section calculations and their errors for some processes are reported in [99–101].

5.7. Signal Region

The same-sign electron pair invariant mass in the signal region is shown in Figure 5.13. The observed number of pairs is compatible with the predicted background. As one

Source	Process	Uncertainty
Trigger	Signal and background from MC simulations	2.1-2.6%
Electron reconstruction and identification	Signal, prompt background	1.9–2.7%
Electron charge misidentification	Opposite-sign backgrounds	9%
Determination of fake factor f	Non-prompt backgrounds	22%
Luminosity	Signal and background from MC simulations	2.8%
MC statistics	Backgrounds from MC simulations	5%
Photon misidentification as electron	$W\gamma$	13%
MC cross sections	Prompt, opposite-sign backgrounds	4%

Table 5.7.: Sources of systematic uncertainty (in %) of the signal yield and the expected background predictions, described in the second column, for the mass range $m_{ee} > 15$ GeV.

Processes affected	Uncertainty
Drell-Yan (Charge flips)	$\pm 7\%$
WZ	$\pm 7\%$
ZZ	$\pm 5\%$
$t\bar{t}W$, $t\bar{t}Z$	$\pm 22\%$
$W^{\pm}W^{\pm}$	$\pm 50\%$
MPI WW, WZ, ZZ	$\pm 100\%$
$t\bar{t}$	$\pm 5\%$
$W\gamma$	$\pm 14\%$

Table 5.8.: Theoretical uncertainties of the production cross section of SM processes modelled by MC.

can see, the dominant background arises from the charge misidentification component. The predicted contributions from each background process with different invariant

mass cuts are shown in Table 5.9. In Figure 5.14 the kinematics of the leading lepton are shown. In Figure 5.15 the angle between same-sign electrons in the pair is shown as well. The background prediction describes the observed numbers of all of these distributions reasonably well within the uncertainty bands.
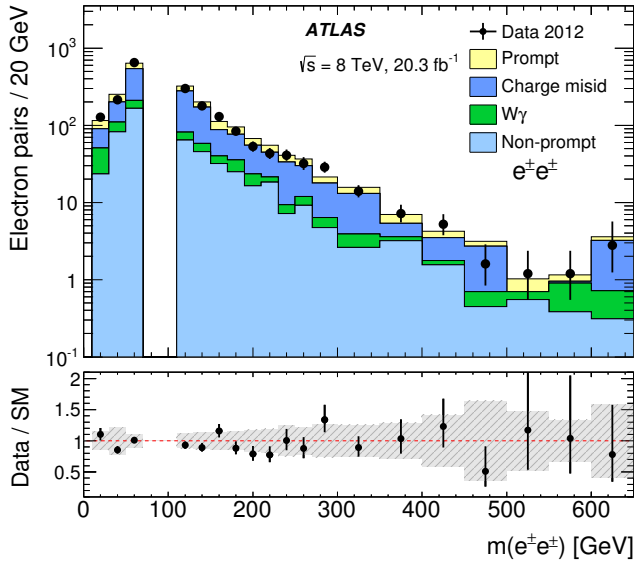
Figure 5.13.: Invariant mass distribution for $e^{\pm}e^{\pm}$ pairs in the signal region. The shaded band in the lower plot corresponds to the combination of the statistical and systematic uncertainties of the background prediction. The last bin is an overflow bin.

5.7.1. Limit setting

The background prediction describes data very well and there are no significant visible deviations which could indicate a potential presence of the BSM signal. The idea of this analysis is to be as general as possible and to perform a search for new physics without favoring any BSM model. Thus, the next step is to calculate exclusion limits on any type of new physics with prompt same-sign lepton pairs.

Due to the limited acceptance of the detector the signal region was designed to use the phase space which is used in ATLAS for precision measurements. This restricted acceptance results in the following relation between total, σ, and measured, or fiducial,

Sample	Number of electron pairs with $m(e^{\pm}e^{\pm})$						
	> 15 GeV	> 100 GeV	> 200 GeV	> 300 GeV	> 400 GeV	> 500 GeV	> 600 GeV
Non-prompt	518.57 ± 120.17	247.49 ± 49.5	71.67 ± 13.15	22.66 ± 4.8	8.13 ± 2.42	3.12 ± 1.49	0.78 ± 1.01
$W\gamma$	175.25 ± 36.28	74.89 ± 15.62	22.42 ± 5.15	8.04 ± 2.26	3.84 ± 1.31	2.69 ± 1.05	1.02 ± 0.57
Drell-Yan	968.61 ± 145.63	513.53 ± 77.7	130.91 ± 26.99	36.1 ± 12.17	12.8 ± 7.89	4.79 ± 4.86	4.79 ± 4.86
$t\bar{t}$	36.92 ± 6.01	30.1 ± 4.99	14.55 ± 2.8	5.05 ± 1.32	2.15 ± 0.78	1.05 ± 0.58	1.18 ± 0.56
WW	13.01 ± 2.34	10.74 ± 1.96	4.85 ± 0.97	1.86 ± 0.45	0.68 ± 0.22	0.43 ± 0.16	0.28 ± 0.13
Charge Flip total	1018.54 ± 145.78	554.37 ± 77.89	150.31 ± 27.16	43.01 ± 12.25	15.62 ± 7.93	6.27 ± 4.89	6.25 ± 4.89
ZZ	86.05 ± 7.21	22.42 ± 2.11	6.75 ± 0.84	1.78 ± 0.37	0.61 ± 0.2	0.34 ± 0.16	0.21 ± 0.12
WZ	234.36 ± 22.24	132.79 ± 12.76	37.12 ± 3.9	10.95 ± 1.43	3.23 ± 0.61	1.5 ± 0.4	0.5 ± 0.22
$t\bar{t}W$	5.33 ± 1.23	3.83 ± 0.89	1.32 ± 0.32	0.44 ± 0.11	0.14 ± 0.04	0.08 ± 0.03	0.03 ± 0.01
$t\bar{t}Z$	1.73 ± 0.41	1.2 ± 0.29	0.4 ± 0.1	0.11 ± 0.04	0.03 ± 0.01	0.02 ± 0.01	0.01 ± 0.01
$WWjj$	14.99 ± 7.59	12.1 ± 6.14	5.55 ± 2.84	2.35 ± 1.22	1.22 ± 0.66	0.4 ± 0.24	0.16 ± 0.11
MPI	4.04 ± 4.06	1.6 ± 1.61	0.38 ± 0.39	0.06 ± 0.07	0.02 ± 0.02	0 ± 0	0 ± 0
Prompt total	346.51 ± 24.95	173.94 ± 14.44	51.52 ± 4.93	15.7 ± 1.92	5.25 ± 0.92	2.34 ± 0.49	0.91 ± 0.28
Total Background	2058.86 ± 193.92	1050.69 ± 94.67	295.92 ± 30.99	89.41 ± 13.49	32.83 ± 8.44	14.41 ± 5.25	8.96 ± 5.04
Data	1976	987	265	83	30	13	7

Table 5.9.: Expected and observed numbers of pairs of isolated same-sign electrons for various cuts on the dielectron invariant mass, m_{ee}. The uncertainties shown include statistical and systematic contributions.
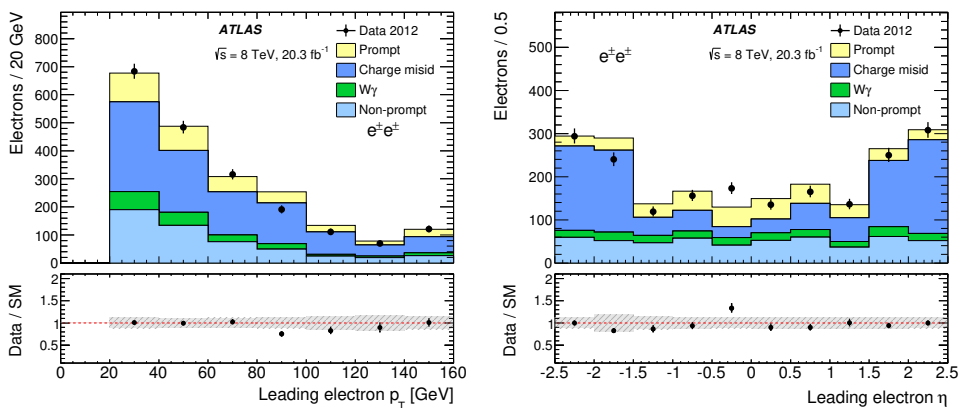
Figure 5.14.: p_T and η distributions of the leading electron in the signal region. The last bin is an overflow bin in the left figure.
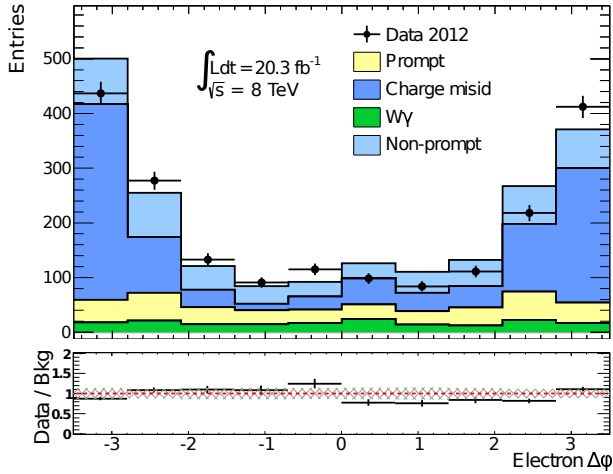
Figure 5.15.: Azimuthal angle difference between two same-sign electrons from the pair in the signal region. The uncertainties shown include statistical and systematic contributions.

σ^{fid}, cross sections:

$$\sigma = \frac{\sigma^{fid}}{\langle N_{pair}\rangle A} \tag{5.4}$$

where $\langle N_{pair}\rangle$ is the average number of same-sign pairs produced per event and A is the fiducial acceptance (or volume). The definition of the fiducial volume is discussed in Section 5.7.2.

The cross section limits are derived using a CL_s [102,103] prescription with the help of the RooStat [104] framework provided by the ATLAS Statistics Committee. The CL_s method states that the signal hypothesis is excluded at the confidence level CL when

$$1 - CL_s \le CL \tag{5.5}$$

where CL_s is defined as

$$CL_s \equiv \frac{CL_{s+b}}{CL_b} \tag{5.6}$$

where CL_b is a confidence level observed for the background-only hypothesis and CL_{s+b} for the background plus signal hypothesis. In practice, CL_b (CL_{s+b}) is a prob-

ability to find the observed data given an expected background (background plus signal). This probability is Poisson-distributed and is calculated based on the number of observed and expected same-sign electron pairs in the signal region. The test statistic used for the limit setting is a log-likelihood-ratio test. Systematic uncertainties and their correlations are taken into account with this method. For example, the charge misidentification scale factor uncertainty is correlated across Drell-Yan, $t\bar{t}$, WW and $W\gamma$ background samples. Experimental errors such as electron reconstruction, identification, energy scale and trigger are each treated as a single shared parameter across all the expected backgrounds and signal. The MC cross section errors are independent except for the diboson (ZZ, WZ and WW) samples. The luminosity is common to all the background samples. The statistical errors are independent.

Following this prescription and using the number of expected and observed same-sign lepton pairs one can compute upper limits at a given confidence level (typically at 95% level) on the number of same-sign lepton pairs (N_{95}) arising from new physics beyond the SM. Limits can be set for different invariant mass thresholds, because the dilepton invariant mass is the main observable in the analysis. Limits on the number of pairs can be translated into upper limits on the fiducial cross section as:

$$\sigma_{95}^{fid} = \frac{N_{95}}{\epsilon_{fid} \times \int \mathcal{L} dt} \tag{5.7}$$

where $\int \mathcal{L} dt$ is the integrated luminosity of the data and ϵ_{fid} is a fiducial efficiency for finding a same-sign electron pair from a possible signal from new physics in the fiducial volume, which is described in the next section.

5.7.2. Fiducial volume and fiducial efficiency

As can be seen from equation (5.4) and (5.7), in order to translate the number of measured and expected lepton pairs to the cross section limit of a signal from new physics, one has to know the fiducial volume and efficiency. The reason is that the detector does not reconstruct leptons with a 100% efficiency, and it does not cover the whole solid angle around the interaction point. The fiducial volume represents the phase space region which is truncated so that it mimics the detector acceptance. It is defined by a set of cuts on the truth (generator) level. Kinematic cuts on the electrons are identical to the ones used in the signal region definition on the reconstruction level:

- Leading electron $p_T > 25$ GeV

- Subleading electron $p_T > 20$ GeV

- $|\eta| < 1.37$ or $1.52 < |\eta| < 2.47$

Requirements on the electron pair are the same as well:

- Same-sign pair with $m_{ee} > 15$ GeV

- Veto pairs with $70 < m_{ee} < 110$ GeV

- No opposite-sign same-flavour pairs with $|m_{ee} - m_Z| < 10$ GeV

Since electrons are required to be isolated on the reconstruction level, isolation has to be applied on the truth level as well. Track-based isolation on the truth level is identical to that on the reconstruction level: all charged particles within the cone $\Delta R < 0.3$ around the electron with $p_T > 0.4$ GeV are considered and the sum of their p_T has to be smaller than 10% of the electron p_T. Calorimeter-based isolation was not applied on the truth level due to a significantly different behaviour at reconstruction and truth levels.

In the case of an ideal detector, fiducial volume would correspond to the geometrical detector acceptance. Since the real detector does not provide a 100% reconstruction and identification efficiency, a fiducial efficiency is used in order to relate the fiducial volume with the real geometrical detector acceptance, which is defined as:

$$\epsilon_{fid} = \frac{N_r}{N_f} \tag{5.8}$$

where N_f is the number of electron pairs which pass the fiducial volume cuts on the truth level and N_r – which pass the fiducial volume cuts on the truth level as well as all the signal selection cuts on the reconstruction level.

In order to perform a search for new physics in a model-independent way, the fiducial efficiency has to be constant and to not depend on the type of the BSM model. However, different models provide different p_T and η spectra, and the electron reconstruction efficiency depends on both p_T and η. As reported in Ref. [30], the efficiency can vary up to 15% for the tight identification criteria with respect to the electron p_T. Also, the presence and number of jets in the final state is model dependent, and affects the electron isolation efficiency, which will have an effect on the fiducial efficiency.

In order to estimate the value of the fiducial efficiency, efficiencies for four different BSM models were calculated:

- Doubly charged Higgs. This model assumes production of two doubly charged scalar bosons which, decaying leptonically, will provide two pairs of same-sign leptons. No jets are produced in the final state of the hard process. The Higgs mass was varied between 100 GeV and 1000 GeV.

- Colored Zee-Babu model. Diquarks are produced, which decay to two lepto-quarks with the same charge, which subsequently decay to a lepton and a quark. The final state consists of one same-sign lepton pair and two jets. The masses considered in the model are 2.5-3.5 TeV for the diquark and 1-1.4 TeV for lepto-quarks.

- Production of a heavy right-handed W_R boson and a heavy Majorana neutrino. W_R decays to a lepton and a Majorana neutrino, which decays to a W boson and another lepton. The final state consists of one same-sign pair and products from the W boson decay. The mass of W_R was varied between 1 TeV and 2 TeV, while the mass of the Majorana neutrino was in the range of 0.25-1.5 TeV

- Pair production of a fourth generation down-type quark. Both quarks decay semi-leptonically to a t quark and subsequently to a b quark. The final state consists of two jets and four W bosons. At least two same-sign bosons have to decay leptonically in order to provide a same-sign lepton pair. This model is characterized by large hadronic activity due to the high jet multiplicity. The mass of the fourth generation quark was varied from 400 GeV to 1 TeV.

The fiducial efficiencies for these models were calculated with different dilepton mass thresholds. The obtained efficiencies are in the range of 48-74%. The lowest efficiency was observed for the fourth generation down-type quark model, while the highest one is found for the heavy right-handed W_R boson and heavy Majorana neutrino process. The latter model has larger efficiency with respect to the doubly charged Higgs model because the final state of the doubly charged Higgs model contains two same-sign pairs compared to one pair in the Majorana model. The efficiencies were measured separately for positive and negative same-sign pairs, and no significant differences were observed.

To provide a conservative cross section limit setting for new physics beyond the SM, the lowest obtained efficiency, which was 48.3%, was used.

5.7.3. Fiducial cross section limits

Computed upper limits at the 95% confidence level on the fiducial cross section (σ_{95}^{fid}) of new physics beyond the SM for the invariant mass thresholds used in Table 5.9 are shown in Figure 5.16. Separate limits for positive and negative same-sign pairs are shown in Figure 5.17. The expected limits are shown together with the 2σ uncertainty bands. The limits are summarized in Table 5.10.
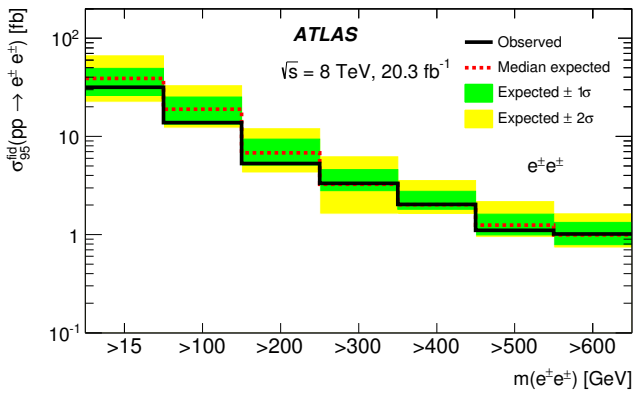
Figure 5.16.: Fiducial cross section upper limits at 95% C.L. for new physics contributing to the signal region for events with $e^{\pm}e^{\pm}$ pairs. Green and yellow bands correspond to the 1σ and 2σ uncertainty bands on the expected limits respectively.
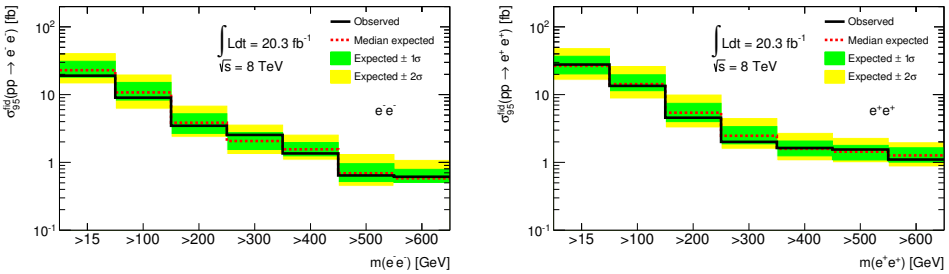
Figure 5.17.: Fiducial cross section upper limits at 95% C.L. for new physics contributing to the signal region for events with $e^{+}e^{+}$ (left) and $e^{+}e^{+}$ (right) pairs. Green and yellow bands correspond to the 1σ and 2σ uncertainty bands on the expected limits respectively.

Mass range	$e^{\pm}e^{\pm}$		e^+e^+		e^-e^-	
	Expected	Observed	Expected	Observed	Expected	Observed
> 15 GeV	39^{+10}_{-13}	32	27^{+11}_{-6}	28	23^{+8}_{-5}	19
> 100 GeV	19^{+6}_{-6}	14	$14.3^{+5.4}_{-2.8}$	13.5	$10.8^{+4.4}_{-2.4}$	9.0
> 200 GeV	$6.8^{+2.6}_{-1.7}$	5.3	$5.4^{+2.0}_{-1.4}$	4.6	$3.9^{+1.4}_{-1.2}$	3.5
> 300 GeV	$3.3^{+1.3}_{-0.4}$	3.3	$2.5^{+0.9}_{-0.6}$	2.0	$2.1^{+0.7}_{-0.5}$	2.6
> 400 GeV	$2.02^{+0.74}_{-0.21}$	2.03	$1.59^{+0.47}_{-0.34}$	1.64	$1.56^{+0.41}_{-0.31}$	1.35
> 500 GeV	$1.25^{+0.36}_{-0.26}$	1.10	$1.44^{+0.34}_{-0.36}$	1.55	$0.69^{+0.27}_{-0.17}$	0.64
> 600 GeV	$0.99^{+0.34}_{-0.20}$	1.02	$1.27^{+0.37}_{-0.26}$	1.10	$0.58^{+0.21}_{-0.08}$	0.61

Table with heading: 95% CL upper limit [fb]

Table 5.10.: Upper limit at 95% CL on the fiducial cross section for $e^{\pm}e^{\pm}$ pairs from non-SM signals. The expected limits and their 1σ uncertainties are given together with the observed limits derived from the data. Limits are given inclusively and separated by charge.

5.8. Mass limits of doubly charged Higgs

As an example of a BSM model which produces same-sign lepton pairs in the final state, the pair production of doubly charged Higgs bosons was studied. The search strategy is the same as described above. Since the final state of this model has two same-sign pairs of leptons, no jet activity and no missing transverse momentum is present in the event. Therefore, there is no need to optimize the signal selection. Doubly charged Higgs decays should be visible as a sharp peak in the dilepton invariant mass. Using a fiducial efficiency calculated in bins of 100 GeV (as it was done for the fiducial limit calculations) is not optimal from the point of view of the signal sensitivity. Thus, the search is performed in mass bins with a mass-dependent width.

5.8.1. MC simulation

Signal samples were generated with Pythia8 [76] with different masses of the left-handed and right-handed doubly charged Higgs bosons. The simulated masses were produced in the range of 50-600 GeV in steps of 50 GeV with one additional mass point at 1 TeV. The kinematics of left- and right-handed Higgs bosons is identical, but the production rate is different due to different coupling to the Z boson mediator [105]. The cross sections were calculated with the NLO precision.

5.8.2. Model acceptance and efficiency

The width of the doubly charged Higgs decay is dominated by the detector momentum resolution of the electrons. Since the decay width depends on the doubly charged Higgs mass, the search was performed using mass bins with variable width. For an optimal bin width, two competing factors have to be considered. On one hand, a mass bin has to cover as much signal as possible, while on the other hand, the background contribution in the mass bin is desired to be as small as possible. To satisfy both conditions, the signal significance, S, was chosen as an optimization criterion:

$$S = \sqrt{2((s + B)ln(1 + s/B) - s)} \tag{5.9}$$

where s is the expected signal and $B = b + \delta b^2$ is the predicted background plus background systematic uncertainty squared. A bin width is parameterized as a second degree polynomial of the Higgs mass. Coefficients of the polynomial were the parameters to optimize. During the optimization procedure it became clear that there is a third effect which has to be taken into account: due to limited statistics of the predicted background, one cannot have too many mass bins, otherwise the cross section exclusion limit will fluctuate significantly from bin to bin.

The next step is to define how many lepton pairs produced in Higgs boson decays are reconstructed, selected and fall into the mass bin. The number of generated Higgs bosons is known, thus one only needs to count number of reconstructed same-sign pairs which pass the signal selection in a given mass bin. The ratio of reconstructed to the total number of generated pairs corresponds to the total efficiency, which includes the effect of the acceptance and efficiency of the signal selection. The efficiencies for each mass point were calculated, but in order to interpolate between the simulated mass points, the total efficiency ε_{tot} is fitted by an empirical piecewise function:

$$\varepsilon_{tot}(m) = \begin{cases} p_0(1 - e^{-(m - p_1)/p_2}) & \text{, if } m < 450 \text{ GeV} \\ p_3 + p_4 m & \text{, if } m \geq 450 \text{ GeV} \end{cases} \tag{5.10}$$

where m is the Higgs mass and p_0, p_1, p_2, p_3, p_4 are fit parameters shown in Table 5.11.

The computed efficiencies for available mass points and their fit are shown in Figure 5.18.

Parameter	Value
p_0	4.76×10^{-1}
p_1	$2.94 \times 10^{+1}$
p_2	$1.05 \times 10^{+2}$
p_3	4.51×10^{-1}
p_4	set by requiring continuity

Table 5.11.: Fitted parameter values for Equation 5.10, which gives $\varepsilon_{tot}(m)$.
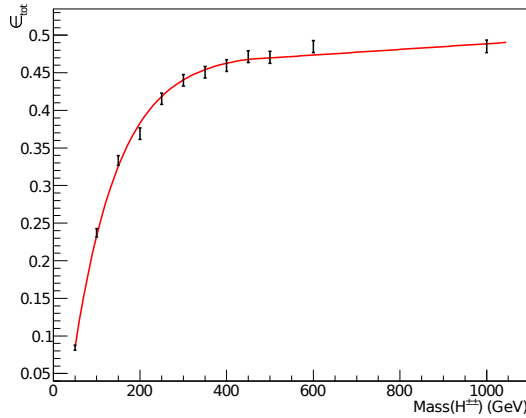
Figure 5.18.: Total reconstruction efficiency (ε_{tot}) of the doubly charged Higgs boson decay to same-sign electron pair as a function of simulated $H^{\pm\pm}$ mass, fitted with a piecewise empirical function.

5.8.3. Cross section and mass limits

The invariant mass distribution of the same-sign electron pairs together with the signal from a left-handed Higgs with masses between 300 GeV and 500 GeV are shown in Figure 5.19. The branching ratio of the $H^{\pm\pm} \to e^{\pm}e^{\pm}$ decay is assumed to be 100%.

The upper cross section limit on pair production of the doubly charged Higgs is set in the same way as the limits on the new physics described above. The cross section is
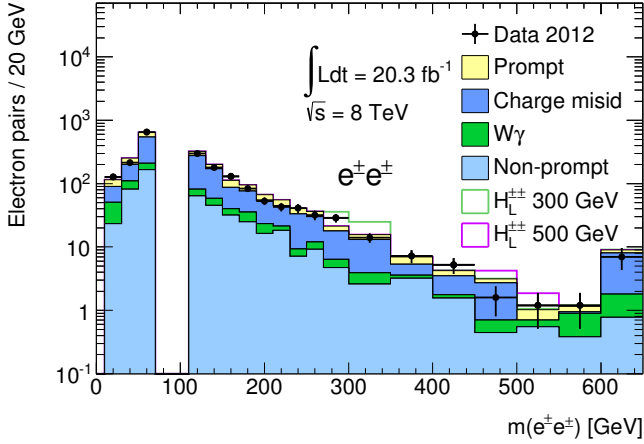
Figure 5.19.: Invariant mass distributions for $e^{\pm}e^{\pm}$ pairs passing the full event selection. Open histograms show the expected signal from simulated $H^{\pm\pm}$ samples, assuming a 100% branching ratio to the same-sign electron pair. The last bin is an overflow bin. Only statistical uncertainties for data are shown.

determined as:

$$\sigma_{HH} \times BR = \frac{N_H^{rec}}{2 \times A \times \epsilon \times \int \mathscr{L} dt} \quad (5.11)$$

where BR is the branching ratio of the $H^{\pm\pm} \to e^{\pm}e^{\pm}$ decay, N_H^{rec} is the number of reconstructed $H^{\pm\pm}$, $A \times \epsilon$ is the total efficiency described earlier and $\int \mathscr{L} dt$ is the integrated luminosity. The factor 2 in the denominator is needed to take into account the presence of two same-sign pairs from H^{++} and H^{--} in the event.

The upper cross section limit times branching ratio (which is assumed to be 100%) at 95% CL is shown in Figure 5.20. The variations between the mass bins are caused by fluctuations of the predicted background due to the low statistics per bin. A good agreement between expected and observed limit lines can be seen, and all deviations are within 2σ. The theoretical cross section curves as a function of Higgs mass for left- and right-handed doubly charged Higgs bosons are shown as well. Lower mass limits of the model correspond to the intersection of the theoretical curve with the expected cross section limit. The obtained mass limits are summarized in Table 5.12.

These limits can also be interpreted as mass limits as a function of the branching ratio for $H_L^{\pm\pm}$ and $H_R^{\pm\pm}$ decays, which are shown in Figure 5.21.
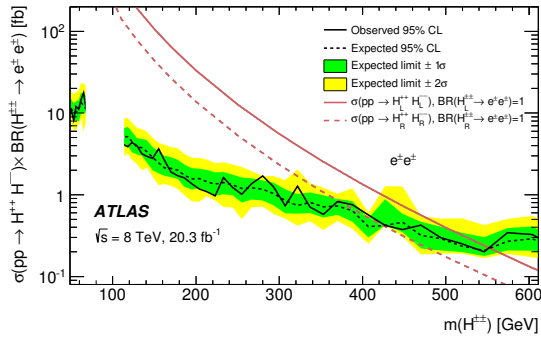
Figure 5.20.: Upper limits at 95% C.L. on the cross section as a function of $e^{\pm}e^{\pm}$ invariant mass for the production of a doubly charged Higgs boson assuming a 100% branching ratio to $e^{\pm}e^{\pm}$. The green and yellow bands correspond to the 1σ and 2σ bands on the expected limits respectively. Pair production cross sections for left and right-handed $H^{\pm\pm}$ are overlaid.

	95% C.L. upper limit [GeV]	
Signal	expected	observed
$H_L^{\pm\pm}$	$552.6^{+11.1}_{-49.9}$	551.2 ± 3.1
$H_R^{\pm\pm}$	$424.8^{+1.0}_{-59.7}$	374.0 ± 6.2

Table 5.12.: Upper limit at 95% C.L. on mass of $H^{\pm\pm}$, assuming 100% branching ratio to $e^{\pm}e^{\pm}$.
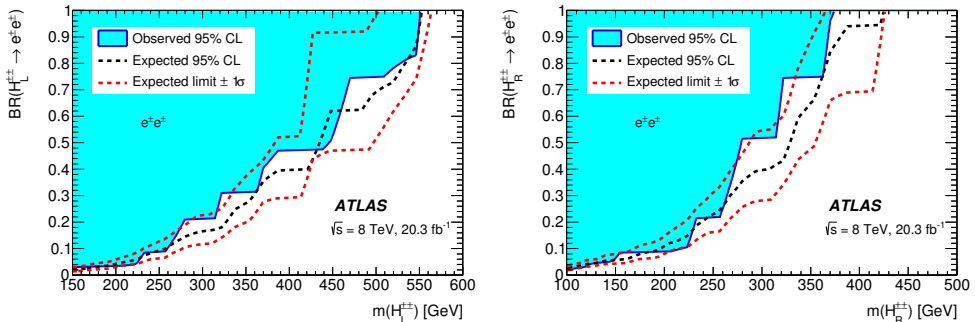
Figure 5.21.: 95% C.L. limits on the doubly charged Higgs mass vs branching ratio of $H_L^{\pm\pm}$ (left) and $H_R^{\pm\pm}$ (right) for events with $e^{\pm}e^{\pm}$ pairs.

	95% C.L. upper limit [GeV]					
	4.7 fb^{-1} at 7 TeV		20.3 fb^{-1} at 8 TeV		13.9 fb^{-1} at 13 TeV	
Signal	Expected	Observed	Expected	Observed	Expected	Observed
$H_L^{\pm\pm}$	407	409	553	551	580	570
$H_R^{\pm\pm}$	329	322	425	374	460	420

Table 5.13.: Upper limit at 95% C.L. on mass of $H^{\pm\pm}$, assuming 100% branching ratio to $e^{\pm}e^{\pm}$ for 7, 8 and 13 TeV analyses results.

5.9. Summary and outlook

An inclusive search for a new physics has been performed in the final state of a same-sign electron pair using 20.3 fb^{-1} of 8 TeV center of mass pp collision data [106]. Limits on the fiducial cross sections has been set as a function of electron pair invariant mass with cuts ranging from > 15 to > 600 GeV. With respect to the previous ATLAS analysis performed with 7 TeV center of mass data (reported in Ref. [107]) cross section limits have been extended with two additional invariant mass bins (> 500 and > 600 GeV).

The analysis result has also been used for a narrow bin search for $H^{\pm\pm}$. Upper limit on the cross section for pair production of right- and left-handed doubly charged Higgs have been set as a function of $H^{\pm\pm}$ mass. Based on predicted cross section limits a mass limit has been derived as well.

Comparison of the obtained 95% C.L. upper $H^{\pm\pm}$ mass limit, assuming 100% branching ratio to $e^{\pm}e^{\pm}$ with results from 7 TeV [108] and 13 TeV [109] analyses performed by ATLAS are shown in Table 5.13. As one can see from Table 5.13 mass limits benefit from the larger center of mass pp collision data though using a dataset with larger integrated luminosity will improve limits further.

The analysis selection can still be improved and developed. One possibility to significantly increase the sensitivity of the search is to optimize the signal region to more efficiently reject the charge misidentification background, which is the dominant background source. In the Run-2 LHC period, many studies have been undertaken in the ATLAS collaboration to investigate electron charge misidentification effect and to suppress it by using new variables e.g. electron E/p (where E is the energy measured in the calorimeter and p is measured by the inner detector).

Another possibility is to investigate sources of systematic uncertainty more deeply. Comparing the three analyses, the dominant sources of systematic uncertainties arise from modelling of the charge misidentification and non-prompt backgrounds for all three. Thus, improving the method used for estimation of these backgrounds would reduce the systematic uncertainty. This is especially important for high-p_T electrons where the charge misidentification rate is poorly understood. Also, increased statistics available in Run-2 can be used for better understanding of the non-prompt background source.

As was mentioned before, the analyses have been performed with three channels: $e^{\pm}e^{\pm}$, $\mu^{\pm}\mu^{\pm}$ and $e^{\pm}\mu^{\pm}$. However, it might be possible to add a tau lepton channel, which would complement results from the other three.

Chapter 6.

Search for new charged bosons in final states with one muon and missing transverse momentum

This chapter describes a search for new spin-1 heavy charged boson (called W') in the final state with one lepton and missing transverse momentum (E_T^{miss}). The search was done with the first $\sqrt{s}$=13 TeV data collected by ATLAS in 2015, corresponding to a luminosity of 3.2 fb^{-1}. The search has been performed in the muon and electron channels, however, this chapter focuses only on the muon channel while for the electron channel only the final results are shown, and the combination of both channels is presented.

6.1. Search strategy

As described in Section 1.3.2, there is a large number of models which predict a new spin-1 charged gauge boson W'. Thus it is not practical to perform a number of dedicated searches for all of them. Therefore, the so-called "sequential" Standard Model (SSM) is often used, as a reference benchmark model. This model provides a clear interpretation of the experimental results and is also used for comparing the results between experiments. It assumes the W' boson to be a heavy "copy" of the SM W with the same couplings to leptons, quarks and gauge bosons. This implies that a new decay channel (with respect to the SM W) should be present: $W' \rightarrow WZ$. This would be the dominant decay mode for high W' masses and lead to the W' width

larger than its mass at $m_{W'} > 500$ GeV. Some models, such as the Left-Right Symmetric model, described previously, predict this channel to be heavily suppressed, in a case of $m_{W_R} \gg m_{W_L}$. The branching ratio for this channel is thus set in searches to be zero for any W' mass. The branching ratio of W' $\rightarrow \mu\nu$ or $e\nu$ as a function of W' mass is shown in Figure 6.1. The rapid decrease at approximately 200 GeV corresponds to the decay channel W' $\rightarrow tb$.
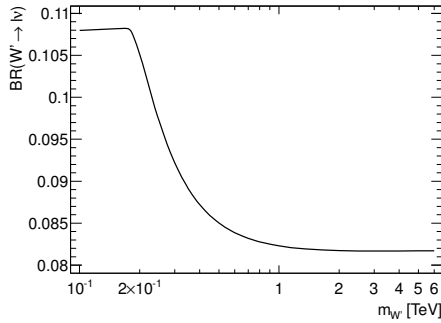
Figure 6.1.: Branching ratio of W' $\rightarrow e\nu$ or $\mu\nu$ as a function of the W' mass. Calculated with Pythia8 MC generator.

Considering this model one can highlight three key features essential for this search:

- Precise modeling of the background prediction. The dominant part of the background originates from the charged-current Drell-Yan process and the analysis selection tests it up to few TeV. Thus, it is crucial to use the latest and most precise high-order calculations and corrections available at the time.

- High-p_T lepton selection. Due to a simple event selection (one isolated lepton and E_T^{miss}) this analysis uses the most energetic lepton candidates available at 13 TeV center-of-mass energy collisions. This is why the understanding of the reconstruction efficiency and momentum resolution of high-p_T leptons are very important for the analysis.

- Missing transverse momentum, E_T^{miss}. Along with the lepton momentum, E_T^{miss} is used in the calculation of the transverse invariant mass m_T (which will be defined in Section 6.4.3), which is the signal discriminant and search variable in the analysis. For m_T to be precisely reconstructed and modelled a good understanding of the missing E_T reconstruction as well as good lepton momentum resolution is needed.
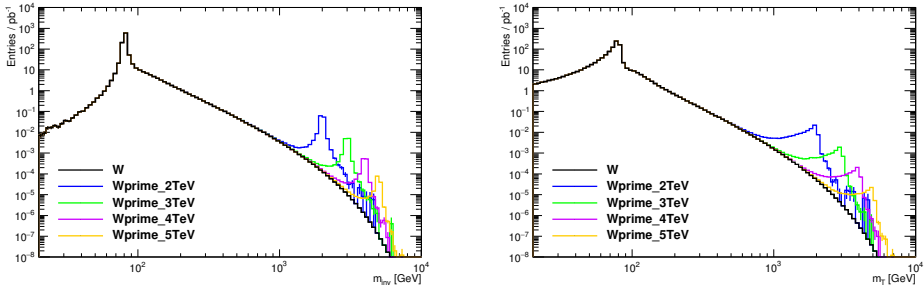
Figure 6.2.: Invariant mass (left) and transverse mass (right) spectrum of the W' signal on top of the W background on generated MC level.

6.2. W' signal in Monte Carlo

Samples for the signal process $W' \rightarrow \mu\nu$ are produced with the leading-order (LO) PYTHIA-8.183 [76] generator for a series of W' masses. Additionally, the so-called flat sample is produced. This sample has a flat lepton-neutrino invariant mass spectrum. Thus, it can be reweighted with the correct line shape to any desired W' mass by an appropriate reweighting function. To verify the validity of this sample and validity of the reweighting procedure, comparisons with fixed mass samples were done. The flat sample was generated with large statistics to cover a wide range of transverse invariant mass m_T.

The invariant mass and transverse mass distributions for the W' samples with pole masses of 2, 3, 4 and 5 TeV are shown superimposed on top of the SM W background in Figure 6.2.

6.3. Background processes

In order to look for a potential signal from new physics, one has to examine all other SM processes which contribute to the final state of interest.

Since this chapter is focused on the muon decay channel, the processes which produce a muon and missing transverse momentum will be discussed, however, in general, the same processes are relevant for the electron decay channel.

The dominant expected background in the analysis comes from the charged current Drell-Yan process. The SM W decays to a lepton and a neutrino, which will be reconstructed as missing transverse momentum in the detector. The contribution of this process appears like a Jacobian peak in the m_T spectrum with a maximum around 80 GeV and a slowly falling tail above 80 GeV. Since W' conceptually is a heavier version of the SM W, it also appears in the transverse mass distribution as a Jacobian peak around the pole mass of the W' boson (as shown in Figure 6.2). The charged current Drell-Yan process is simulated with POWHEG-BOX v2 [110]and PYTHIA-8.186 generators at the next-to-leading-order (NLO) using the CT10 [72] NLO PDFs. The cross section is corrected to the next-to-next-to leading order (NNLO) using the CT14NNLO PDF set by applying QCD and Electroweak (EW) mass-dependent K-factors to the MC generator cross sections. To get a sufficient statistics at the high transverse mass, several samples, binned in invariant mass of the lepton-neutrino pair, are used and are shown in Figure 6.3.
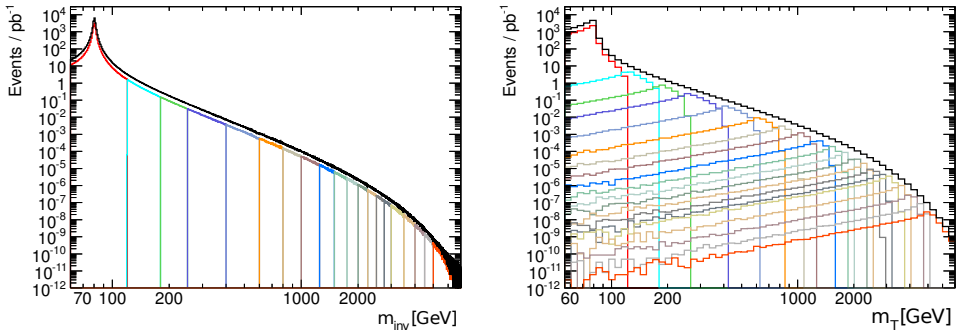
Figure 6.3.: Invariant mass and transverse mass spectrum of the invariant mass-binned W samples on generated MC level. The coloured lines show the different mass slices and the black line – the sum of all, scaled up with a factor of 2.

The neutral current Drell-Yan process $Z/\gamma^* \to \mu\mu$ can contribute to the muon plus E_T^{miss} final state if one of the muons is not properly reconstructed in the detector and thus contributes to the value of E_T^{miss}. In this case, it will not be used in the E_T^{miss} calculation itself, but will contribute to the E_T^{miss}, as will be described in Section 6.4.3. This process is simulated with the same MC generators and at the same order as the W boson production process. The contribution of the processes $W \to \tau\nu$ and $Z \to \tau\tau$, which can affect the muon channel, if the tau lepton decays to muon and neutrinos $(\tau^- \to \mu^- \overline{\nu_\mu} \nu_\tau)$, are considered and simulated in the same way.

Another background which contributes to the final state of interest is the $t\bar{t}$ and single top production. The top quarks decay immediately to a W boson and a b quark. The further leptonic decay of the W provides an isolated muon and E_T^{miss} from the the neutrino. Some Feynman diagrams of the top production processes are shown in Figure 6.4 and Figure 6.5. This background is simulated with POWHEG-BOX and PYTHIA-6.428 [45] at NLO using the CT10 [72] NLO PDFs. All these processes are considered as "Top" background in what follows.
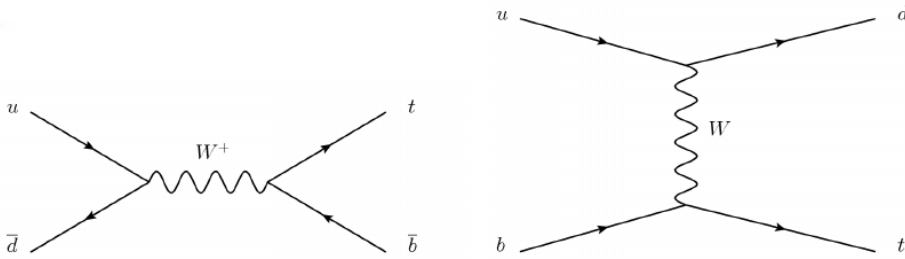
Figure 6.4.: Feynman diagrams for the single top production in the s-channel (left) and t-channel (right).
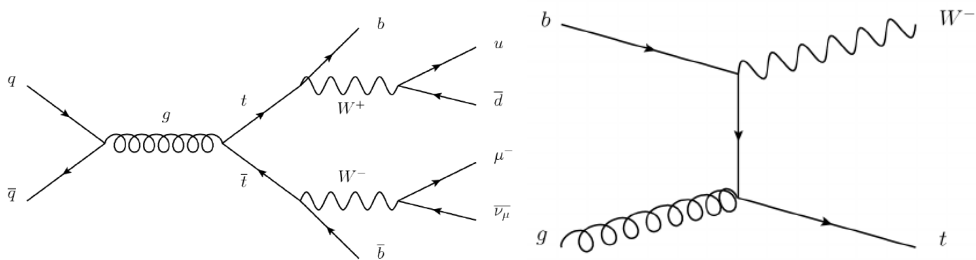
Figure 6.5.: Feynman diagrams for the production of a top quark pair (left) and $W + t$.

More than one SM gauge boson can be produced in a single hard interaction, thus processes with WW, WZ and ZZ boson pairs produced in the final state are also contributing to the background. Some Feynman diagrams of such processes are shown in Figure 6.6. Contribution to the muon plus E_T^{miss} final state can come from decays like $WZ \to \ell\nu\nu\nu$ or $WZ \to \ell\nu q\bar{q}$. These processes are simulated with SHERPA-2.1.1 [47] using the CT10 NLO PDFs. They are called a "diboson" background in what follows.

Only the inclusive samples for both diboson and top backgrounds were available from the official ATLAS production. This is why it was decided to produce samples binned in the transverse mass of lepton plus E_T^{miss}. However, due to technical
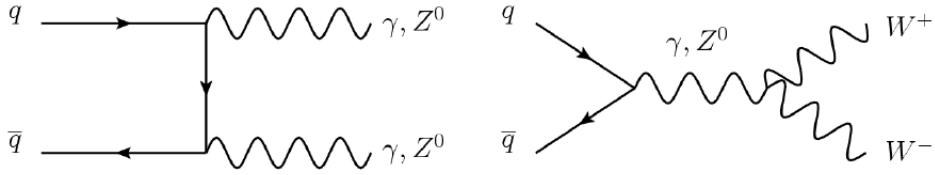
Figure 6.6.: Feynman diagram for the diboson production.

complications, these samples were not finished in time for the 2015 analysis, thus a dedicated extrapolation procedure to the high-m_T region has been used to estimate these backgrounds. It is planned to use these samples for the upcoming paper with the combined results of 2015 and 2016.

The list of all background processes and used MC generators is shown in Table 6.1.

Process	Generator + fragmentation/ hadronization	PDF set	Normalization based on
$W+$ jets, Z/γ^*+ jets	POWHEG-BOX v2 [110] + PYTHIA-8.186 [76]	CT14NNLO [111]	NNLO QCD with VRAP [112], NLO QED with MCSANC [113,114]
$t\bar{t}$, t-channel t, s-channel Wt	POWHEG-BOX + PYTHIA-6.428 [45]	CT10	NLO QCD
WW, WZ, ZZ	SHERPA-2.1.1 [47]	CT10	NLO QCD
$W' \to \ell\nu$	PYTHIA-8.183	NNPDF2.3 LO	NNLO QCD with VRAP,

Table 6.1.: List of MC generated samples used for background prediction. The used MC generator, PDF set and order of cross section calculations used for the normalization are listed for each sample.

6.4. Event object selection

The analysis is based on *pp* collision data collected in 2015 by the ATLAS detector with 13 TeV CM energy. The integrated luminosity of the data sample corresponds to 3.2 fb^{-1} and the mean number of interactions per bunch crossing was 14.

An event selected for the analysis has to have at least one reconstructed vertex with at least two tracks matched to it. If there are several vertices, the one with the highest $\sum p_T^2$, where p_T is the transverse momentum of the matched tracks, is chosen. Events should have at least one muon candidate, and fire the single muon trigger, which requires the presence of one muon with $p_T > 50$ GeV.

6.4.1. Lepton selection

The muon reconstruction in ATLAS is performed independently in ID and MS detectors. Information from the detectors is then combined to form a muon track [115]. The track reconstruction is done separately in the ID and MS, after which a global refit is done to form a combined track. Muon p_T is measured from the track curvature.

Muons of interest are high-p_T isolated muons, with tracks that originate from the primary vertex. Candidates have to satisfy the following set of criteria:

- $p_T > 55$ GeV: to ensure a high and uniform trigger efficiency.

- $|\eta| < 2.5$, excluding $1.01 < |\eta| < 1.1$: muons have to be within ID acceptance. A small region is excluded in order to reject muons whose tracks in the muon spectrometer fall into poorly aligned chambers (relative barrel-endcap alignment).

- Transverse and longitudinal impact parameters $|d_0|/\sigma(d_0) < 3$ and $|z_0 \times sin\theta| < 10$ mm: this selection ensures that the muon was produced close to the primary vertex and rejects muons originating from decays of long-lived particles. The recommendation by the muon combined performance (MCP) working group has a more strict requirement $|z_0 \times sin\theta| < 0.5$ mm, however, as this criteria rejects many muons and just a little background it was decided to relax this requirement to 10 mm as will be described in Section 6.4.2.

- Pass "high-p_T" set of muon identification criteria. In the same way, as for electrons, ATLAS defines three sets of reference muon identification criteria designed

for use in analyses: "loose", "medium", "tight". These criteria are designed in a hierarchical way – increasing the background rejection power at some cost to the identification efficiency. In 2015 a new "high-p_T" set has been introduced which aims to maximize the momentum resolution for tracks with $p_T > 100$ GeV [115, 116]. It includes strict requirements on the MS part of the track, which improves the p_T resolution by approximately 30% in comparison with the "tight" criteria. However, the muon reconstruction efficiency drops by 20% as well.

- Pass "LooseTrackOnly" isolation requirement. ATLAS defines seven muon isolation working points for use in analyses. They differ by used discriminating variables and by definition [115, 116]. "LooseTrackOnly" requirement provides 99% constant efficiency over the complete (η,p_T) phase space. The discriminating variable is the ratio of the sum of p_T of all tracks (excluding the muon itself) with $p_T > 1.0$ GeV within $\Delta R = min(10$ GeV $/p_T^\mu, 0.3)$ cone around the muon track, to the muon track p_T^μ.

6.4.2. Optimization of the signal selection

To suppress the contribution from the neutral current Drell-Yan Z/γ^* and $t\bar{t}$ processes, in which two isolated leptons are expected in the final state, an additional lepton veto requirement is applied. Events are rejected if a second muon with $p_T > 20$ GeV is found passing either the high-p_T or the medium identification criteria. Events are also vetoed if an additional electron passing the following selection is found:

- $|\eta| < 2.47$, excluding barrel-endcap calorimeter transition region $1.37 < |\eta| < 1.52$

- $p_T > 20$ GeV

- Transverse impact parameter $|d_0|/\sigma(d_0) < 5$

- Pass the medium muon identification criteria

- Pass the "Loose" isolation criteria [115, 116]. In contrary to the "LooseTrackOnly" isolation described before, it uses an additional calorimeter-based discriminating variable to provide the same efficiency. The additional variable is the ratio of the sum of the transverse momentum of topological clusters [117] (excluding the

muon contribution itself) within $\Delta R = 0.2$ cone around the muon track, to the muon track p_T^μ.

- Electron must not overlap with the muon: $\Delta R(e, \mu) > 0.1$. If it overlaps ($\Delta R(e, \mu) > 0.1$) it is assumed that the electron candidate arises from photon radiation from the muon and the event is kept.

These veto requirements lead to a significant reduction of the dimuon (Z) background at high transverse mass as well as some reduction of the $t\bar{t}$ background. The reduction of the total background level is approximately 10–15% at high transverse mass. The signal efficiency is found to be essentially unaffected. The possibility of using the "loose" identification working point for the additional muon veto was also considered. However, it was found to provide only a tiny improvement (1–3% additional reduction of the total background level) with respect to using "medium" working point, thus the latter was chosen to be used.

As mentioned before, the requirement $|z_0 \times sin\theta| < 0.5$ mm should be applied by default. The main purpose of this requirement is to veto events with cosmic muons. However, vetoing additional muon in the event we "automatically" discard most of the events with cosmic muons. After a dedicated study by the MCP group, it was found that the $|z_0 \times sin\theta|$ requirement can be loosened to 10 mm, without significant decrease of the cosmic muon rejection power. Figure 6.7 shows the d_0 significance ($|d_0|/\sigma(d_0)$) and $|z_0 \times sin\theta|$ cut efficiencies. The efficiency shown in the left panel is for the recommended $|z_0 \times sin\theta|$ selection value of 0.5 mm, while in the right panel – for a looser cut value of 10 mm. The nominal cut value leads to a reduction of the selection efficiency by about 1% due to a wrong vertex being associated to the primary vertex. This efficiency is partially restored by the loosened cut.

6.4.3. Transverse mass and missing transverse momentum

The missing transverse momentum, E_T^{miss}, is calculated following the ATLAS recommendation described in Ref. [118, 119]. E_T^{miss} is calculated as a vector sum of the p_T of selected objects:

- muons which satisfy the analysis signal selection;
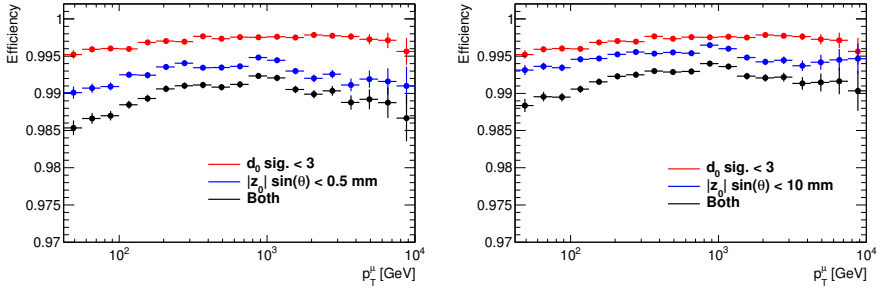
Figure 6.7.: d_0 and $|z_0 \times sin\theta|$ cut efficiencies. The d_0 efficiency is shown for the cut recommended by the tracking group. In the $|z_0 \times sin\theta|$ case the recommended cut of 0.5 mm (left) and an alternative cut of 10 mm (right) are shown. The efficiencies are calculated for combined muons in the W′ flat sample passing the medium or high-p_T working point requirements.

- electrons which satisfy the requirements described previously in Section 6.4.2 with a stronger transverse momentum requirement of $p_T > 55$ GeV and passing tight electron identification criteria (which is the electron signal selection);

- tau leptons which satisfy the "medium" identification criteria [120] and $|\eta| < 2.5$, excluding $1.37 < |\eta| < 1.52$ and $p_T > 20$ GeV requirements;

- photons which satisfy the "tight" identification criteria [121], $|\eta| < 2.37$, excluding $1.37 < |\eta| < 1.52$ and $p_T > 25$ GeV requirements;

- jets reconstructed with the anti-k_t algorithm [122] with the radius parameter of 0.4 in $|\eta| < 4.9$. Jets are calibrated using the method described in Ref. [123]. Only jets with $p_T > 20$ GeV are used;

- tracks originating from the primary vertex with $p_T > 0.5$ GeV and $|\eta| < 2.5$ but not belonging to any of the reconstructed physics objects listed above.

The missing transverse momentum is required to be larger than 55 GeV in order to balance the lepton transverse momentum cut. This cut value allows one to significantly suppress the multi-jet background, which will be described below.

The main variable of interest, m_T, which is used for statistical discovery analysis is defined as:

$$m_T = \sqrt{2p_T E_T^{miss}(1 - \cos \varphi_{\ell\nu})} \tag{6.1}$$

where $\varphi_{\ell\nu}$ is the angle between the muon momentum and the missing transverse momentum in the transverse plane.

The transverse mass has to be $m_T > 110$ GeV which corresponds to twice the required value of the muon momentum and E_T^{miss}.

6.5. Background estimation

The background which arises from neutral and charged current Drell-Yan processes (W, Z), diboson production (WW,WZ,ZZ) and top background ($t\bar{t}$, single top) is estimated with MC simulation.

Processes with multijet final state have a small chance to have a reconstructed muon present in these events. There are two cases when jets can lead to a reconstructed muon. In the first case a hadron is not stopped in the calorimeter and passes through to the muon spectrometer and is misidentified as a muon. Another possibility is if a real muon originates from a jet. However, such muons are not produced in the primary vertex, because they originate from decays of heavy flavor hadrons, which have long lifetimes and travel for few hundreds of μm's before they decay. Thus, such muons from jets are called "fake" muons.

Due to the huge cross section of the processes which lead to multijet final states it would be very difficult to model this background in the simulation, this is why a data-driven method, the so-called Matrix Method, is used to estimate the contribution of multijet processes to the signal muon selection.

6.5.1. The Matrix Method

The goal of this method is to get an estimation of the "fake" muon contribution to the signal region. The "fake" muons are expected to be non-isolated, however, a fraction of them pass the isolation cut. The idea of the method is to measure the probability (efficiency) of the "fake" muons (which pass the loosened signal selection without isolation requirement) to pass the nominal muon signal selection without requiring isolation. The same efficiency is measured for "real" muons, which originate from processes with muons from the primary vertex.

The matrix method provides a connection between the number of true "fakes" (N_F) and "real" muons (N_R) with the measurable quantities: the number of muon candidates which pass loose but fail tight selection criteria (N_L) and the number of candidates which pass the tight selection criteria (N_T), via equation (6.2).

$$\begin{pmatrix} N_T \\ N_L \end{pmatrix} = \begin{pmatrix} \epsilon_R & \epsilon_F \\ 1 - \epsilon_R & 1 - \epsilon_F \end{pmatrix} \begin{pmatrix} N_R \\ N_F \end{pmatrix} \qquad (6.2)$$

The vector on the right hand side of the equation corresponds to the truth quantities which are independent from each other. This implies the quantities in the vector on the left hand side have to be independent as well, thus N_L should not contain any events from N_T, and therefore the former value is defined as passing the loose selection but failing the tight one.

The matrix consists of efficiencies of "fake" and "real" muons passing the signal selection which are denoted as ϵ_F and ϵ_R, respectively. The efficiency is defined as the ratio of the number of "fake"("real") muons which pass the tight selection, N_{tight}^{fake} (N_{tight}^{real}), to the number of muons which fail the tight but pass the loose selection, N_{loose}^{fake} (N_{loose}^{real}):

$$\epsilon_F = \frac{N_{tight}^{fake}}{N_{loose}^{fake}}, \qquad \epsilon_R = \frac{N_{tight}^{real}}{N_{loose}^{real}}. \qquad (6.3)$$

The total number of muons passing the signal selection is given in the first line of the matrix:

$$N_T = N_{tight}^{real} + N_{tight}^{fake} = \epsilon_R N_R + \epsilon_F N_F, \qquad (6.4)$$

and consists of the fraction of "fake" muons which pass the signal selection and the fraction of "real" muons. The value of interest is the true number of "fake" muons which pass the signal selection. One can express this quantity by inverting the matrix in equation (6.2) and using the relation in equation (6.4):

$$\begin{pmatrix} N_R \\ N_F \end{pmatrix} = \frac{1}{\epsilon_R(1 - \epsilon_F) - \epsilon_F(1 - \epsilon_R)} \begin{pmatrix} 1 - \epsilon_F & -\epsilon_F \\ \epsilon_R - 1 & \epsilon_R \end{pmatrix} \begin{pmatrix} N_T \\ N_L \end{pmatrix} \qquad (6.5)$$

Thus, the true number of "fake" muons which pass the signal selection is:

$$N_{tight}^{fake} = \epsilon_F N_F = \frac{\epsilon_F}{\epsilon_R - \epsilon_F} \left(\epsilon_R (N_L + N_T) - N_T \right) \tag{6.6}$$

which is expressed by quantities which can be calculated from the data.

The cut used to distinguish between loose and tight muons is the isolation cut, and the loose muons are thus defined as passing the signal muon selection cuts, except the isolation cut. Tight muons correspond to the baseline selection.

The "real" muon efficiency is extracted from MC simulation, which reproduces well the efficiency of the isolation cut in data. The "fake" muon efficiency is measured in a control region designed to have a high purity of "fake" muons. The region is defined in the same way as the signal selection besides cuts on E_T^{miss} and m_T, and requiring in addition:

- At least one jet with $p_T > 40$ GeV which does not overlap ($\Delta R > 0.2$) with the selected muon.

- Opening angle in the transverse plane between the muon and the E_T^{miss}, $\Delta\phi_{\mu, E_T^{miss}} < 0.5$.

- No Z candidate (any two muons with $80 < m_{\mu\mu} < 100$ GeV).

- d_0 significance, $|d_0|/\sigma(d_0)$, greater than 1.5.

- $E_T^{miss} < 55$ GeV, ensuring that the control region does not overlap with the signal region.

This region is enhanced with "fake" muons, however, a significant "real" muon contamination is present in the region as well. This contribution, as predicted by MC simulation, is subtracted.

The obtained efficiencies are shown in Figure 6.8.

The systematic uncertainty was estimated for both "real" and "fake" muon efficiencies. The "fake" muon efficiency uncertainty was estimated by variation of the requirements for "fake" muon control region. These variations are:

- Removing the Z veto and $\Delta\phi_{\mu, E_T^{miss}}$ cuts.
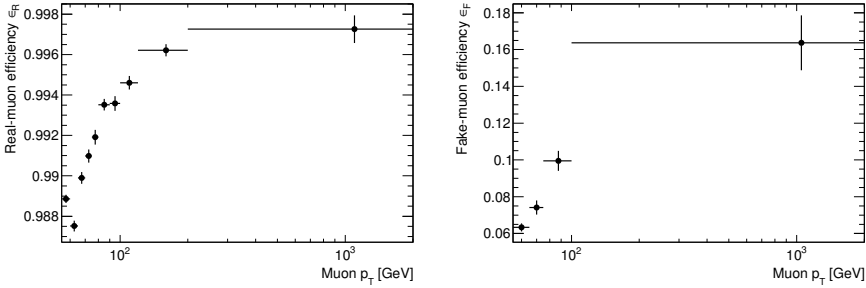
Figure 6.8.: Efficiency of the "real" (left) and "fake" (right) muons as a function of muon p_T used in the data-driven matrix method to estimate contribution of the multijet background to the signal selection.

- Removing the Z veto and $\Delta\phi_{\mu,E_T^{miss}}$ cuts, but tightening the d_0 significance cut to 2.

- Removing the d_0 significance cut.

- Using a tighter d_0 significance cut of 2.

- Removing the jet requirement.

- Removing the jet requirement, but tightening the d_0 significance cut to 2.

- Requiring $E_T^{miss} < 20$ GeV.

- Requiring $20 < E_T^{miss} < 55$ GeV.

The "fake" efficiency was recalculated by using each of this requirements separately. The effect on the "fake" muon efficiency is shown in Figure 6.9 (right).

Since the "real" muon efficiency is obtained from MC simulation one can use the efficiency obtained with the tag-and-probe method (using muon pairs in the invariant mass window $80 < m_{\mu\mu} < 102$ GeV from $Z \to \mu\mu$ decays) as a variation of the systematic uncertainty. A comparison of the efficiencies obtained with MC simulation and with the tag-and-probe method are shown in Figure 6.9 (left).

The impact of the systematic variations of the efficiencies on the final m_T spectrum of the multijet background will be discussed in Section 6.6.6.
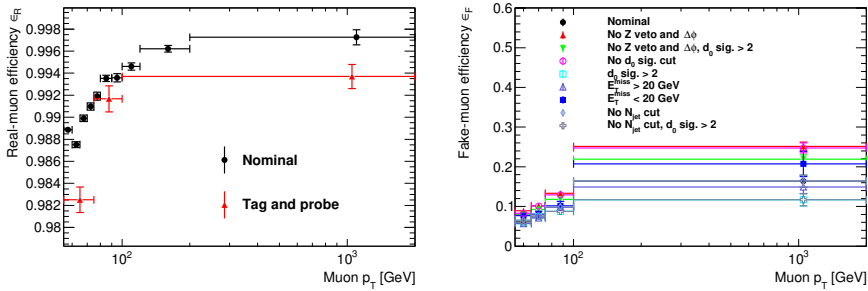
Figure 6.9.: Systematic variations of the "real" (left) and "fake" (right) muon efficiencies as a
function of muon p_T.

6.5.2. Multijet validation region

To test the data-driven multijet background prediction, one has to find a region in
which its contribution will be enhanced. This region has to be kinematically close to the
signal region. Therefore, a validation region is defined in the same way as the signal
selection but without the E_T^{miss} and m_T requirements. Two sets of validation regions
are considered: with and without using isolation requirements. They correspond to
the tight and loose muon definitions used in the matrix method.

The distributions of the variables used to define the enhanced "fake" muon control
region are shown in Figure 6.10. A reasonable agreement within 10% for both the
tight and loose distributions is observed for $\Delta\phi_{\mu,E_T^{miss}}$ and muon d_0 significance, as can
be seen from the data over background prediction ratio plots in the bottom of each
plot. The shape of the distributions is modelled well too for both the tight and loose
regions. The most obvious discrepancy is seen in the distribution of the number of
jets. The disagreement most likely arises from the modeling of jet emission in the $W+$
jets MC, where only one jet emission is included at the matrix element level. This
in principle affects the MC subtraction in the "fake" muon control region. However,
the discrepancy is present only for $N_{jet} \geq 2$, while the control region is defined with
the requirement $N_{jet} \geq 1$ and thus this discrepancy does not affect strongly the "fake"
muon efficiency calculations. Furthermore, one of the systematic variations of the
"fake" muon efficiency was obtained with no N_{jet} cut at all. The effect of the variation
of the N_{jet} requirement was found to be negligible.

The E_T^{miss}, muon momentum and m_T distributions are shown in Figure 6.11. The
contribution of the "fake" background to the tight distributions (right-hand plots) is

tiny. Thus, the agreement between background estimation and observation demonstrates that the background is well modelled by the MC simulation. Since no E_T^{miss} and m_T cuts are applied there is significantly more statistics available than in the signal region. This allows to test the overall background prediction more precisely.

In the sample fulfilling the looser muon definition (left-hand plots) the multijet background is significantly enhanced which provides us with a handle to check the "fake" background estimate. A reasonable agreement within 10-15% for both the tight and loose selections is observed for all distributions. The level of the agreement is comparable between loose and tight distributions, which shows the validity of the "fake" background estimation.

Taking into account the size of the systematic uncertainties, discussed in Section 6.6, the data and background prediction agree reasonably well.

6.5.3. Background extrapolation

The MC simulation of the top and diboson background processes was available from the official ATLAS production only as inclusive samples. They did not provide enough statistics in the high-m_T region. Therefore, these backgrounds were fitted in the low-m_T region and extrapolated to obtain a smooth description in the high-m_T region.

The fit was done with functions that were previously used to extrapolate the background, as for example in the 8 TeV dilepton resonance search [124]. One choice is defined as:

$$f(m_T) = e^{-a} m_T^b m_T^{c \log(m_T)} \tag{6.7}$$

The second one is:

$$f(m_T) = \frac{a}{(m_T + b)^c} \tag{6.8}$$

These two functions were used to preform fits of the backgrounds in different ranges. The best fit according to the $\chi^2/N.d.o.f$ value has been used as a central value. The systematic uncertainty is estimated as the envelope of all fits. The statistical uncertainty of the fit was found to be negligible.
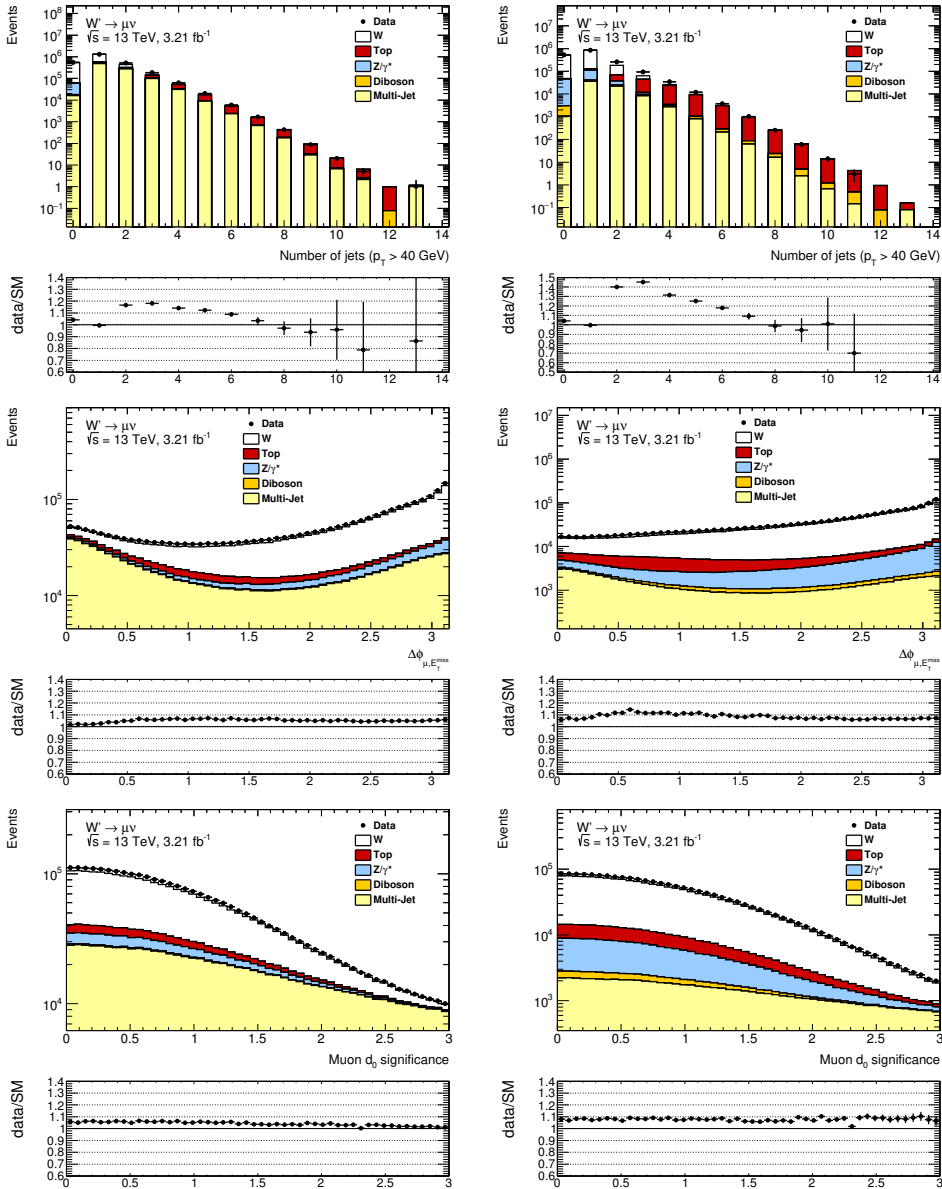
Figure 6.10.: Distributions of the number of jets (top), $\Delta\phi_{\mu,E_T^{miss}}$ (middle), and d_0 significance (bottom) in the inclusive loose (left) and tight (right) muon samples. The distributions are considered before the E_T^{miss} and m_T cuts.

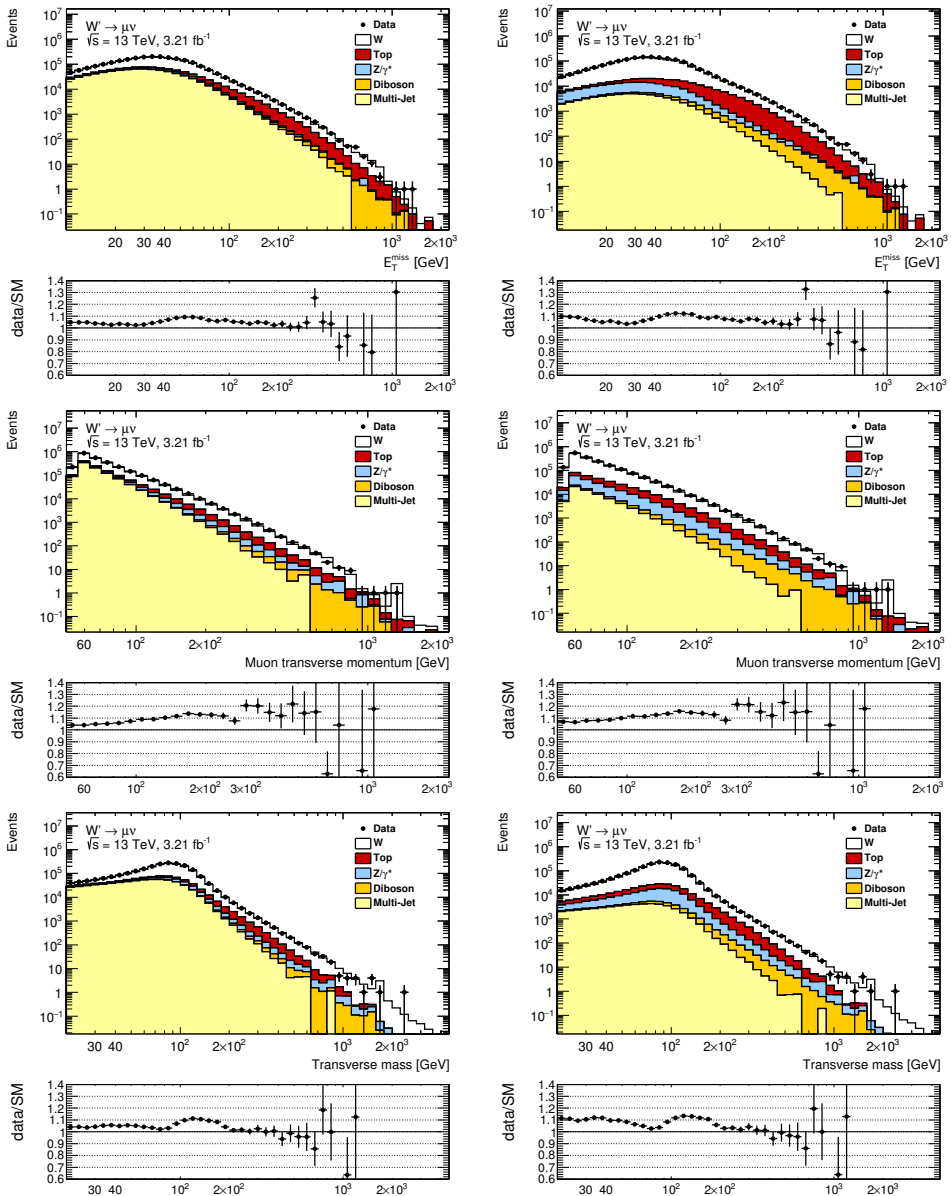**Figure 6.11.:** Distributions of the E_T^{miss} (top), p_T (middle), and m_T (bottom) in the inclusive loose (left) and tight (right) muon samples. The distributions are considered before the E_T^{miss} and m_T cuts.

The starting value for the top background was varied in the range from 140 GeV to 260 GeV in steps of 20 GeV. The end fit point was varied from 600 GeV to 900 GeV in steps of 25 GeV. For the diboson background these values were from 120 GeV to 240 GeV and from 500 GeV to 700 GeV, respectively, with the same step widths as for the top sample. The extrapolation is used in the m_T spectrum starting from $m_T = 600$ GeV for both top and diboson background estimations.

The fits and appropriate systematic uncertainty estimates are shown in Figure 6.12 for the top and in Figure 6.13 for the diboson backgrounds.

Figure 6.12.: Fit and extrapolation of the top background. Both the full set of individual fits (left) and the resulting central value and uncertainty (right) are shown.
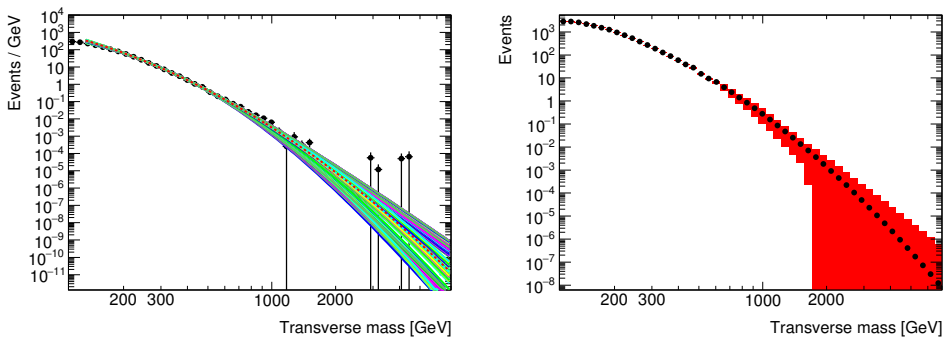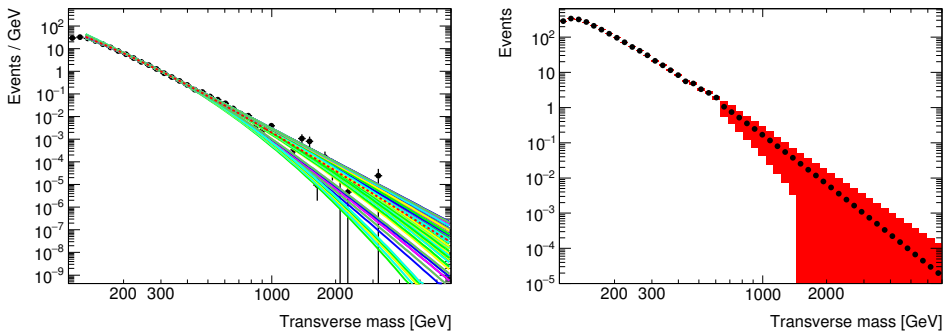

Figure 6.13.: Fit and extrapolation of the diboson background. Both the full set of individual fits (left) and the resulting central value and uncertainty (right) are shown.

The multijet data-driven background estimation suffers from large statistical fluctuations in the high-m_T region, thus the same fitting and extrapolation procedures are

also used here. The fits are performed in the ranges of 150–300 GeV and 200–300 GeV. The extrapolation was stitched to the multijet background estimate at $m_T = 300$ GeV.

6.6. Systematic Uncertainties

6.6.1. Muon efficiency, resolution and scale

The muon efficiency corrections are obtained by the MCP group using the tag-and-probe method on $Z \to \mu\mu$ and $J/\psi \to \mu\mu$ decays in data [125]. Systematic uncertainties are derived from variations of the tag-and-probe selection, background subtraction and other parameters as defined by the group. [31].

The muon momentum corrections are obtained by fitting certain correction constants to match the invariant mass distribution in $Z \to \mu\mu$ and $J/\psi \to \mu\mu$ decays in MC to that observed in data [125]. The dependence of the muon momentum on the fit parameters is given by a model where each parameter is associated to a certain source of potential data/MC disagreement. Systematic uncertainties are derived from variations of the fit procedure, alignment studies and other parameters as defined in [31].

6.6.2. Jet energy scale and resolution

The jet energy scale and resolution uncertainties enter the analysis through the E_T^{miss} calculation, since the E_T^{miss} is calculated using calibrated jets. The uncertainties for the jet energy scale and resolution are provided by the ATLAS JetEtMiss working group [123, 126]. The jet energy scale uncertainty has been tested for different recommended scenarios and was found to be negligible for all of them.

No resolution smearing is applied in the default scenario. According to the working group recommendation, effect of the smearing has to be used as a systematic uncertainty.

The jet uncertainties are fully correlated between the electron and muon channel.

6.6.3. Missing transverse momentum scale and resolution

The uncertainties for the E_T^{miss} scale and resolution are provided by the JetEtMiss group [118]. They enter the analysis through the soft term in the E_T^{miss} calculation, which corresponds to the energy deposits in the calorimeter not associated with any reconstructed physics objects (leptons, photons, jets). The uncertainties cover differences between data and MC and are only applied to MC. The E_T^{miss} uncertainties are fully correlated between the electron and muon channel. The jet, electron and muon energy/momentum uncertainties are affecting the E_T^{miss} calculation. These uncertainties are propagated to the E_T^{miss} calculation in the same way.

6.6.4. Background estimate uncertainty

The uncertainties of the charged and neutral current Drell-Yan processes were estimated by variations of the value of α_s and electroweak corrections as well as by using different PDF error sets and estimating the difference between these PDF sets. The α_s influence was estimated by varying α_s by ± 0.0003. This corresponds to the 90% CL uncertainty. The effect on the W background was 3% at most and the effect is therefore neglected. The variation of the electroweak corrections was estimated to be larger than 3% and was taken into account during extraction of limits. The PDF uncertainty of the CT14NNLO PDF is one of the main theory uncertainties and it was calculated by using 90% CL PDF error set. The uncertainty related to the choice of the PDF set used was estimated by comparing results with NNPDF3.0 [127]. The difference between CT14 and HERAPDF2.0 is not considered as the PDF does not include high Bjorken-x data.

The uncertainty of the "Top" and "Diboson" backgrounds modelling consists of the theoretical cross section uncertainty and the high-m_T extrapolation uncertainty. The former uncertainty affects the total background prediction by less than 3% and thus is neglected; the latter one becomes considerable at the high-m_T region and is taken into account during the limit setting step.

The detailed description of the theoretical uncertainties on the MC cross section can be found in [128].

6.6.5. Trigger and luminosity

The systematic uncertainty of the trigger efficiency is evaluated by the ATLAS trigger group and it is related to the trigger efficiency of muons which is dependent on η and p_T. The luminosity uncertainty was estimated in the same way as described in Section 4.4, however, the current analysis is using a preliminary luminosity uncertainty (which was available at the time of the publication of the first 13 TeV paper) equal to 5%. It was obtained from the preliminary calibration of the luminosity scale done using data from van der Meer scans in August 2015.

6.6.6. Multijet background

The systematic variations of the "real" and "fake" efficiency used in the matrix method were described previously in Section 6.5.1. The multijet background has a very small contribution to the muon signal selection, as can be seen in Figure 6.14 (left), where the fraction of the multijet background to the total background after the final selection is shown as a function of m_T. Thus the effect from the systematic variations of the matrix method efficiencies on the total background is small as well, as shown in Figure 6.14 (right). The systematic uncertainty on the total background is at the level of 1% for $m_T < 4$ TeV and less than 2% for $m_T > 4$ TeV.
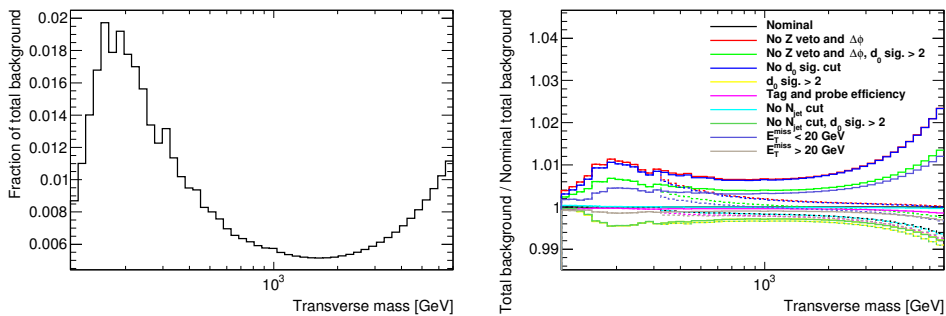
Figure 6.14.: The fraction that the fake muon background constitutes of the total background as a function of m_T (left) and the effect of systematics variations on the total background level as function of m_T (right). The power law fits are used for the fake muon background above $m_T = 300$ GeV. In the left plot, the fit range 150–300 GeV is used, and in the right plot, the range 150–300 GeV corresponds to solid lines while 200–300 GeV – to dashed lines.

Source	Background	Signal
Trigger	3% (4%)	4% (4%)
Lepton reconstruction and identification	5% (8%)	5% (7%)
Lepton isolation	5% (5%)	5% (5%)
Lepton momentum scale and resolution	3% (11%)	1% (4%)
E_T^{miss} resolution and scale	$< 0.5\%$ ($< 0.5\%$)	$< 0.5\%$ ($< 0.5\%$)
Jet energy resolution	1% (2%)	$< 0.5\%$ ($< 0.5\%$)
Multijet background	1% (1%)	N/A (N/A)
Diboson & top-quark bkg.	5% (15%)	N/A (N/A)
PDF choice for DY	$< 0.5\%$ (1%)	N/A (N/A)
PDF variation for DY	8% (12%)	N/A (N/A)
Electroweak corrections	4% (6%)	N/A (N/A)
Luminosity	5% (5%)	5% (5%)
Total	14% (25%)	9% (12%)

Table 6.2.: Systematic uncertainties on the expected number of events as evaluated at $m_T = 2$ (4) TeV, both for signal events with a W'_{SSM} mass of 2 (4) TeV and for background. Uncertainties estimated to have an impact $< 3\%$ on the expected number of events in both channels and for all values of m_T are not listed. Uncertainties that are not applicable are denoted "N/A".

6.6.7. Summary

Table 6.2 lists various systematic uncertainty sources and their sizes for the background and for the W′ signal with $m_T(W') = 2$ and 4 TeV at transverse masses equal to 2 and 4 TeV. All uncertainties below 3% have been neglected so far since they do not affect the final result of the statistical analysis. The remaining experimental and theoretical systematics are applied to the background. Only the experimental uncertainties are applied to the signal.
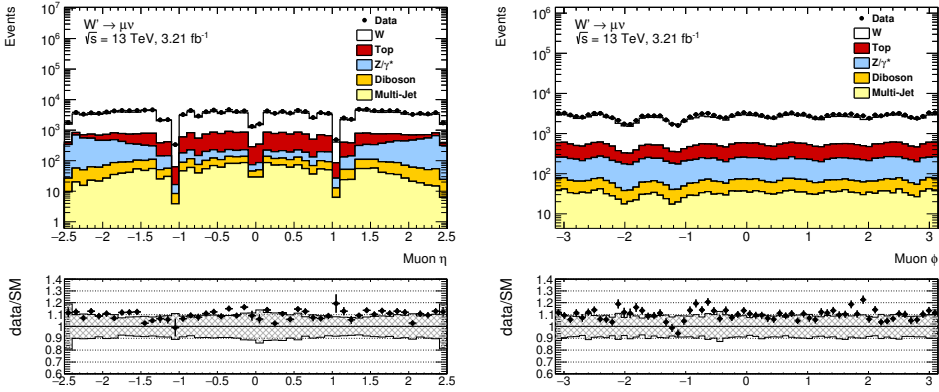
Figure 6.15.: Muon η (left) and ϕ (right) distributions after the final selection. The uncertainty band in the ratio plot indicate the sum in quadrature of the systematic uncertainties.

6.7. Signal Region

The muon η, ϕ, p_T, and E_T^{miss} distributions in the signal region are shown in Figure 6.15 and Figure 6.16. The dominant contribution to the signal region originates from the W boson background. No visible excess and good agreement between data and background estimate are observed.

The basis for the statistical analysis and the main distribution of interest is the transverse mass distributions which are shown in Figure 6.17. The resonant W' signal overlaid on the background prediction is shown as well. As one can see from the data over background prediction ratio plot, the data is systematically above the total background prediction in the low-m_T region but are still within the $\pm 1\sigma$ uncertainty band, which is dominated by the E_T^{miss} systematic uncertainty at low m_T.

Table 6.3 shows the contributions of individual backgrounds as well as the total background and the data in different m_T regions. The quoted uncertainties include both systematic and statistical uncertainties except the uncertainty on the integrated luminosity (5%). One can observe a good agreement between the data and the total background prediction in all m_T regions. The charged-current Drell-Yan is the dominant contribution in the high-m_T region which is more than 90% of the total background for $m_T > 1$ TeV. No events with $m_T > 3$ TeV are observed in the data.
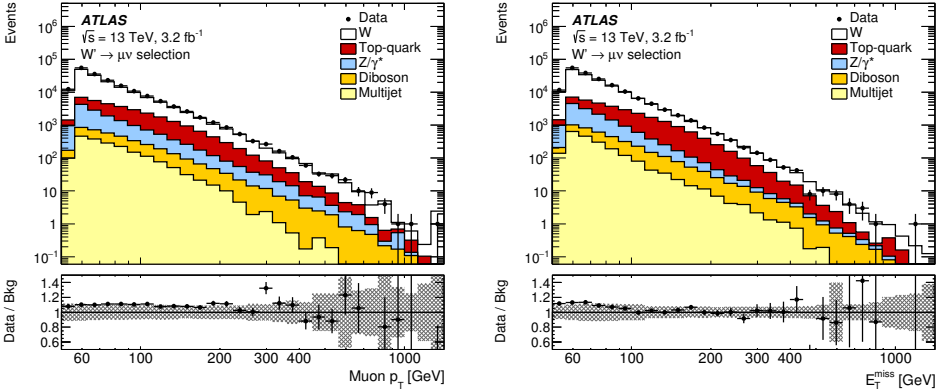
Figure 6.16.: Muon p_T (left) and E_T^{miss} (right) distributions after the final selection. The uncertainty band in the ratio plot indicate the sum in quadrature of the systematic uncertainties.

Figure 6.17.: Muon m_T distribution after final selection. Shown is the total background estimate with resonant W' signal overlaid for various pole masses. The uncertainty band in the ratio plot indicate the sum in quadrature of the systematic uncertainties.

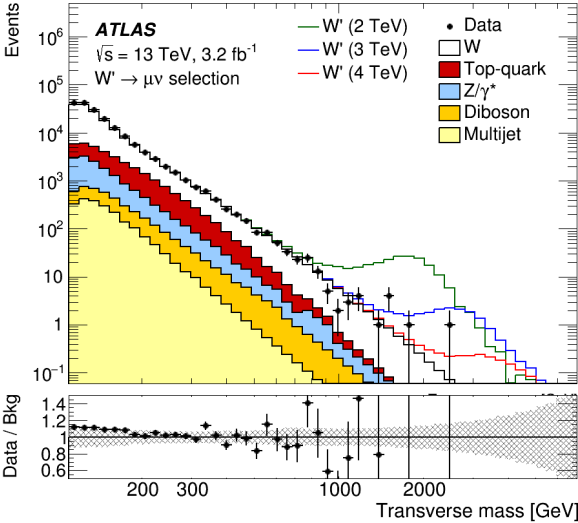| Process	m_T [GeV]						
	110–150	150–200	200–400	400–600	600–1000	1000–3000	3000–7000
W	98100 ± 10000	21000 ± 2000	7700 ± 400	476 ± 30	110 ± 9	13.0 ± 1.2	0.051 ± 0.010
Top	9900 ± 700	5410 ± 340	3090 ± 140	120 ± 6	13 ± 5	0.44 ± 0.32	0.00005 ± 0.00030
Z/γ^*	7700 ± 1000	2130 ± 250	840 ± 70	37 ± 4	7.6 ± 1.8	0.64 ± 0.06	0.0037 ± 0.0007
Diboson	1140 ± 80	588 ± 33	326 ± 14	20.6 ± 1.2	3.8 ± 2.1	0.4 ± 0.4	0.002 ± 0.008
Multi-jet	1350 ± 40	551 ± 23	180 ± 10	5.6 ± 1.0	0.85 ± 0.21	0.078 ± 0.028	0.00038 ± 0.00022
Total SM	118000 ± 12000	29700 ± 2600	12100 ± 600	660 ± 40	135 ± 11	14.6 ± 1.4	0.058 ± 0.013
Data	131672	31980	12393	631	121	15	0

Table 6.3.: Contributions of individual backgrounds with uncertainties for different m_T regions. The uncertainties include both statistical and systematic uncertainties, and all weights are included so that the total background level can be compared to data. The systematic uncertainty includes all systematic uncertainties which are included in the statistical analysis except the uncertainty on the integrated luminosity (5%). For the multi-jet background, only the statistical uncertainty is shown, since the multi-jet systematics are not included in the statistical analysis.

6.8. Cross section and mass limits

To search for a W$'$ signal-like excess in the data a log likelihood ratio test is performed using the RooStat [104] framework. The likelihood function is constructed as the product of Poisson probabilities of all m_T bins in the search region. The effect of systematic uncertainties is described by nuisance parameters in the likelihood function.

Since no significant deviations have been observed, the upper limit on the cross section for the production of W$'$ times branching ratio has been set. A Bayesian approach has been used for the limit settings, and the limits were calculated with the Bayesian Analysis Toolkit [129].

Upper limits are set on the cross section times branching ratio, W$' \to \ell\nu$, at 95% C.L. The limits for the electron, muon, and combined lepton channels are presented in Table 6.4, Figure 6.18 and Figure 6.19. The theoretical cross section curves as a function of W$'$ mass are shown as well. The lower mass limits of the model correspond to the intersection of the theoretical curve with the expected cross section limit. The obtained mass limits are summarized in Table 6.4. The mass limit has improved by 800 GeV in comparison with the previous ATLAS search reported in Ref. [130].
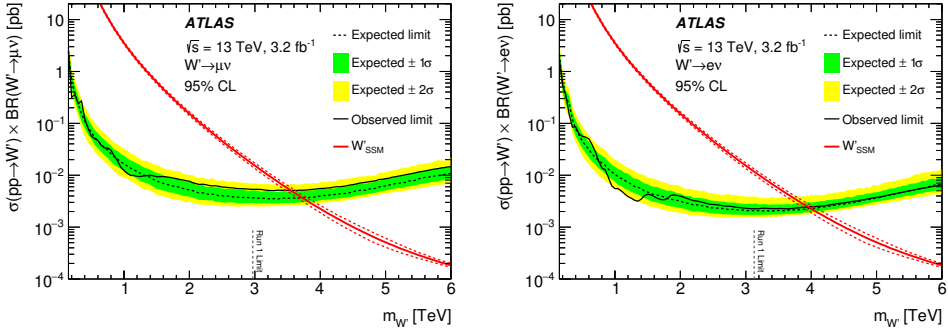
Figure 6.18.: W$'$ cross section limit results for the muon (left) and electron (right) channels.
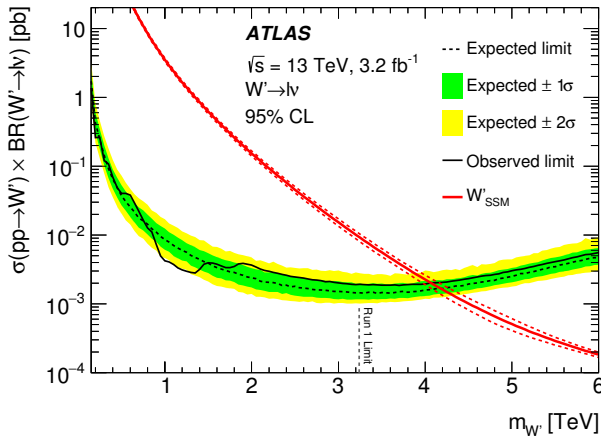
Figure 6.19.: Combined W$'$ cross section limit results.

	$m_{W'}$ lower limit [TeV]	
Decay	Expected	Observed
W$' \rightarrow e\nu$	3.99	3.96
W$' \rightarrow \mu\nu$	3.72	3.56
W$' \rightarrow \ell\nu$	4.18	4.07

Table 6.4.: Expected and observed 95% CL lower limit on the W'_{SSM} mass in the electron and muon channels and their combination.
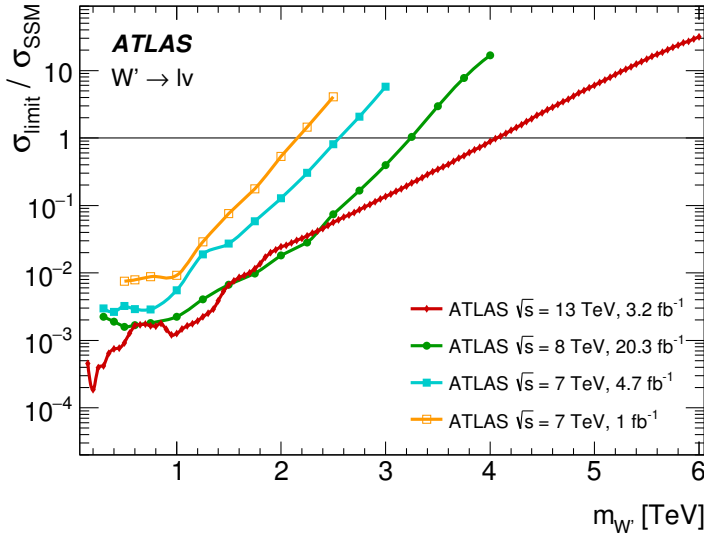
Figure 6.20.: Cross section limits for W' searches performed by ATLAS normalized to the SM background cross section prediction. The region above each curve is excluded at 95% CL.

6.9. Summary and outlook

A search for a new heavy gauge boson W' has been performed in the final state with a muon and missing transverse momentum using 3.2 fb^{-1} of $\sqrt{s} = 13$ TeV pp collision data collected in 2015. This has also been reported in Ref. [128]. Upper limits on the cross section for SSM W' production have been set as a function of the W' pole mass. A significantly stronger exclusion mass limit has been obtained in comparison to previous ATLAS searches [130–132] as shown in Figure 6.20. For comparison, the mass limits for three ATLAS analyses using $\sqrt{s} = 8$ and 13 TeV data are shown in Table 6.5 and the results from the CMS collaboration shown are in Table 6.6. As can be seen, the measured mass limits are compatible between the two experiments.

One of the possibilities to extend the analysis is to consider BSM models which predict an associated pair production of the DM particles with SM W boson. Such models have been investigated in a previous ATLAS search [130]. A sensitivity study of the signal selection for different DM models has been performed (see Appendix A). The study concluded that the sensitivity of the DM models, recommended by the

Signal	95% C.L. upper limit [TeV]					
	20.3 fb^{-1} at 8 TeV		3.2 fb^{-1} at 13 TeV		13.3 fb^{-1} at 13 TeV	
	Expected	Observed	Expected	Observed	Expected	Observed
$W' \to e\nu$	3.13	3.13	3.99	3.96	4.59	4.64
$W' \to \mu\nu$	2.97	2.97	3.72	3.56	4.33	4.19
$W' \to \ell\nu$	3.17	3.24	4.18	4.07	4.77	7.74

Table 6.5.: Upper limit at 95% C.L. on mass of SSM W' for three ATLAS analyses using $\sqrt{s} = 8$ and 13 TeV pp collision data [128, 130, 133].

Signal	95% C.L. upper limit [TeV]			
	19.7 fb^{-1} at 8 TeV		2.2 fb^{-1} at 13 TeV	
	Expected	Observed	Expected	Observed
$W' \to e\nu$	3.18	3.22	3.7	3.8
$W' \to \mu\nu$	3.09	2.99	3.8	4.0
$W' \to \ell\nu$	3.26	3.28	4.2	4.4

Table 6.6.: Upper limit at 95% C.L. on mass of SSM W' for two CMS analyses using $\sqrt{s} = 8$ and 13 TeV pp collision data [134, 135].

ATLAS/CMS Dark Matter Forum [136] for Run-2 searches, is small. Even with more luminosity, the DM interpretation in this channel is not worthwhile.

There are still ways to improve the analysis. One of the possibilities is to include phase-space that has been excluded due to the problem with the alignment in the muon spectrometer as was described in Section 6.4.1. Another improvement mentioned previously is to use m_T binned diboson and top MC background samples, which will provide enough statistics to populate the high-m_T region and no extrapolations will be needed (which is the dominant contribution to the systematic uncertainty).

One can investigate the possibility to apply less strict muon identification criteria in a way such that the muon efficiency is increased without affecting significantly neither the muon resolution nor the background rejection power.

A better understanding of the missing transverse momentum could result in a significant reduction of the systematic uncertainty in the low-m_T region, which is used to validate the background estimations.

Appendix A.

Sensitivity study of the mono-W Dark Matter models

A.1. Introduction

Besides the W$'$ model discussed in Chapter 6, there are other BSM models which can provide a signal in the lepton plus E_T^{miss} selection. For example, some models (which are referred to as mono-W models further down in the text) that try to explain Dark Matter (DM) through hypothetical particles which can be produced at the LHC, assume an associated production of pairs of weakly interacting massive particles (WIMPs) with the SM W boson. Because these DM candidates do not interact strongly or electromagnetically, they will escape undetected in the same way as neutrinos from leptonic W decays, and will contribute to the E_T^{miss} of the event.

There is a plethora of different models available which aims to explain the DM. However, only a few benchmark models are used for the interpretation of results in order to be able to compare results between different analyses and experiments. Many LHC Run-1 analyses were using models based on the Effective Field Theories (EFT). This was the case for the previous search with a lepton and E_T^{miss} final state in 8 TeV collision data, where limits on the DM production have been set considering three DM models: D1, D5 and D9 [130].

However, recent studies have shown that these models do not respect gauge symmetries of the SM, which leads to spurious cross section enhancements at the LHC energies [137]. Thus, simplified models are recommended to be used instead for Run-2 analyses by the ATLAS/CMS Dark Matter Forum, as described in Ref. [136]

This appendix contains a qualitative study of the sensitivity of the analysis selection to the recommended simplified models. D5 EFT DM and W$'$ models are used as a reference for the comparison.

A.2. Theoretical models

The EFT DM models are based on the assumption that the DM-SM interactions are mediated through the exchange of particles that are much heavier than the typical momentum transfer of that interaction [138]. Under such an assumption, the propagator which connects SM quarks to the DM particles becomes independent from the momentum transfer of the interaction. In this case the SM-DM interaction is described with the mass scale $M_* = M/\sqrt{g_q g_\chi}$, where M is the mediator particle mass, and g_q and g_χ are the mediator couplings to the SM quarks and the DM particle, respectively. As described in Ref. [139], different types of DM particles (Dirac fermions, scalars) and types of interaction (effective operators) can be used, which leads to many different models. Models used in the previous analysis [130] assume DM particles to be Dirac fermions with scalar (D1), vector (D5) and tensor (D9) effective operators. In this study we consider two EFT models: the D5 EFT model with only constructive interference with the SM included (which is denoted as D5c later in the text) and the WW$\chi\chi$ EFT model. Feynman diagrams illustrating these models are shown in Figure A.1. It is worth to mention that the DM interacts directly with pairs of electroweak bosons in the WW$\chi\chi$ EFT model. Thus, mass scale M_* characterize strength of the coupling of the DM with electroweak bosons [140].

Simplified models resolve the EFT contact interaction in single-particle s- or t-channel exchange. Thus, one can consider different types of SM-DM mediators (spin-0, spin-1 or Higgs bosons) [141]. Simplified models considered in this study assume a spin-1 neutral mediator, namely, the Z$'$. Both the s- and t-channel scenarios are considered, as shown in Figure A.2.

The DM model samples have been generated with the default configurations recommended by the ATLAS DM Forum. Information about the MC generators and PDF sets used to produce the DM samples is summarized in Table A.1. A set of samples with different Z$'$ masses for simplified models has been generated (see Table A.2), however, only one sample per EFT model was generated, with mass scales equal to 1 TeV and 3 TeV for D5c and WW$\chi\chi$ models, respectively.
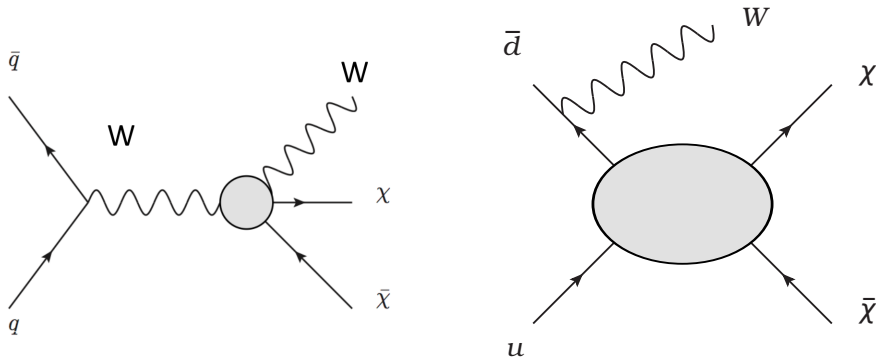
Figure A.1.: Representative diagrams for production of Dark Matter pairs ($\chi\bar{\chi}$) associated with a W boson in models where Dark Matter interacts directly with the W boson (left) or with quarks (right). Unresolved vertices are shown with shaded areas which correspond to the contact interaction between SM and DM sectors described by the Effective Field Theories.
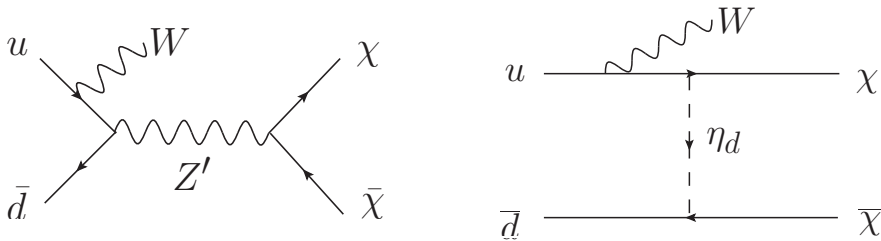
Figure A.2.: Feynman diagrams of production of the Dark Matter pairs ($\chi\bar{\chi}$) associated with a W boson in the simplified model in the s-channel (left) and t-channel (right) scenarios.

| Model	Generator	Fragmentation/Hadronization	PDF set
Simplified s-channel	MADGRAPH-5	PYTHIA-8	NNPDF2.3 LO
Simplified t-channel	MADGRAPH-5	PYTHIA-8	NNPDF2.3 LO
EFT D5	MADGRAPH-5	PYTHIA-8	MSTW2008 LO
EFT WW$\chi\chi$	MADGRAPH-5	PYTHIA-8	NNPDF2.3 LO

Table A.1.: List of MC generated samples for DM models. The used MC generator and the PDF set are listed for each sample.

A.3. Sensitivity studies

The main idea of this study is to understand the kinematics of the simplified DM models in the final states with one lepton and missing transverse momentum and to estimate the sensitivity of this analysis to such models. The signal selection is designed with focus on the high-m_T region since the low-m_T region has been tested in many other analyses during Run-1. The kinematic distributions of the DM models were studied to evaluate the contribution in the signal region and to perform a comparison with a signal from the W$'$ model. It is worth mentioning that the simplified DM model samples with different masses of the produced DM particles have been studied as well and it was found that the shape of the m_T spectrum does not depend significantly on

Model	Channel	Parameters	Cross section, [nb]
Simplified	s-channel	$M_{Z'}$=10 GeV	5.2×10^{-2}
		$M_{Z'}$=100 GeV	2.0×10^{-3}
		$M_{Z'}$=10 TeV	7.5×10^{-11}
	t-channel	$M_{Z'}$=10 GeV	1.9×10^{-3}
		$M_{Z'}$=100 GeV	9.2×10^{-5}
		$M_{Z'}$=2 TeV	4.9×10^{-8}
EFT	WW$\chi\chi$	M_*=3 TeV	3.6×10^{-10}
	D5c	M_*=1 TeV	4.4×10^{-4}
W$'$		$m_{W'} = 2$ GeV	1.1×10^{-4}

**Table A.2.:** Mono-W cross section for different theoretical models.
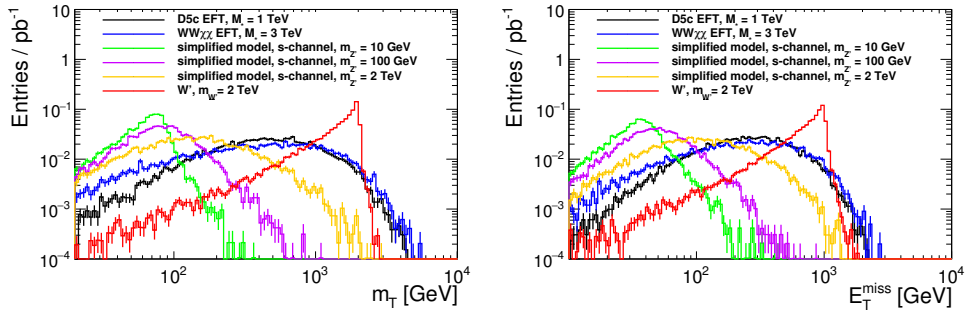
Figure A.3.: Normalized transverse mass (left) and missing transverse momentum (right) distributions of the simplified model in the s-channel and EFT models together with the W′ model.

the mass. Therefore, all the simplified DM model samples described below have the mass of the DM particles set to 1 GeV.

In Figure A.3 the normalized distributions of the transverse mass of the lepton and E_T^{miss} on the generated MC level for the s-channel simplified model and EFT models are shown together with the W′ model. The first observation that can be made is that there is no sharp peak structure in any of these distributions for the DM models. This is expected, because the missing transverse momentum is formed by a neutrino from W boson decay and two DM particles which are independent of each other.

The second observation is that the largest part of the signal of the simplified DM models is in the low-m_T region and is outside of the signal selection for any mediator mass parameter. However, with increasing mediator mass the m_T spectrum tends to become more flat and shifts towards higher m_T values. Distributions obtained from the EFT models have dominant signal contribution in the high-m_T region.

Figure A.4 shows the transverse mass distributions scaled to the integrated luminosity of the respective sample for the DM and W′ models with comparison to the SM W boson background. As one can see from Figure A.4 (left), both W′ and D5c models show an excess with respect to the SM W boson background at the high-m_T region. The $WW\chi\chi$ EFT model has a significantly lower contribution, which can be explained by the fact that the sample has been generated with the mass scale $M_* = 3$ TeV, while it was equal to 1 TeV for the D5c model. This is why a scan for a range of M_* values from 100 GeV to 6 TeV for the $WW\chi\chi$ process was done, and cross sections were estimated by the MADGRAPH MC generator. The dependence is shown in Figure A.5.
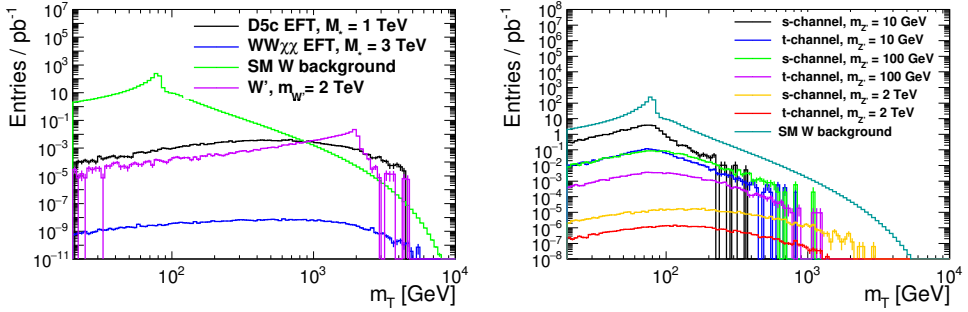
Figure A.4.: The transverse mass distribution of the EFT and W′ models (left) and the simplified model in the s- and t-channels (right) in comparison with the SM W background scaled to the respective process cross section.
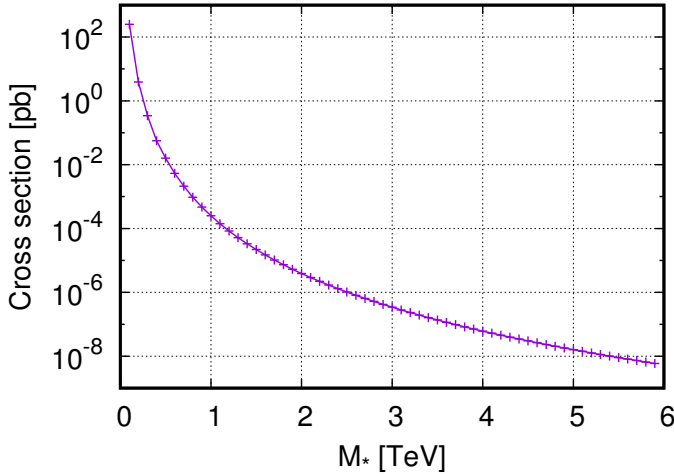
Figure A.5.: Cross section of DM pair production in the $WW\chi\chi$ EFT model as a function of mass scale M_*.

As one can see, the cross section for $M_* = 1$ TeV is approximately three orders of magnitude higher than for $M_* = 3$ TeV. Since the kinematics of the final state for the EFT models does not depend on the value of parameter M_*, one can simply scale the m_T distribution. As one can see from Figure A.4 (left), even if one scales up the $WW\chi\chi$ distribution by three orders of magnitude, it will still be lower than the contribution from the D5c EFT model.

Figure A.4 (right) shows the transverse mass distributions for s- and t-channel simplified DM models together with the SM W boson background. The shape of the distributions from the simplified DM models is very similar to the one for the SM W boson background, which jeopardizes the effectiveness of the m_T distribution as the signal discriminant. In general, the m_T spectrum contribution of the SM W background is a few orders of magnitude larger than the signal from the simplified DM models. A comparison of the distributions for the s- and t-channels shows that the t-channel distributions have similar shapes as the one from the s-channel, however cross sections of the t-channel processes are one-two orders of magnitude lower than for the s-channel (as can be seen from Table A.2).

A.4. Validity of EFT approach

The cross section for both EFT processes strongly depends on the mass scale M_*, as shown in Figure A.5 for the $WW\chi\chi$ EFT model. In order for the $WW\chi\chi$ process to have a sizeable cross section compared to the W' ($M_{W'}$=2TeV) model, the mass scale M_* has to be of the order of 200-300 GeV. However, the EFT approximation is valid only when the momentum transfer in a given process of interest is much smaller than the mass of the mediating particle. In Ref. [142] the authors investigate the validity of the EFT approach at the LHC energy scale. They demonstrate that for $\sqrt{s} = 14$ TeV the EFT approach can be used only for M_* values higher than 1-2 TeV, depending on the assumptions on the SM-DM couplings.

A.5. Conclusion

The transverse mass and E_T^{miss} distributions for all the presented DM models are shown in Figure A.4. This can be compared to a W' signal with $M_{W'} = 2$ TeV. It is clearly seen that the simplified DM models tend to contribute to the low-m_T region outside of the signal selection and have distributions similar to the SM W boson background. This demonstrates that the signal selection used in the search presented in this appendix has low sensitivity to the simplified DM models recommended for Run-2 DM searches at LHC.

On the other hand, the EFT DM models contribute to the high-m_T region, but, as described above, the D5c model has a spuriously enhanced cross section at the LHC energies and are not recommended to be used in Run-2. The $WW\chi\chi$ EFT model has a significantly smaller contribution for physically motivated values of the mass scale M_*.

Similar studies were done by Bell and collaborators [138] where the authors estimated an approximate upper limits using simplified DM models with 3000 fb^{-1} of integrated luminosity at the LHC. They considered a set of different final states (di-jets, mono-jets and mono-leptons) and showed that the sensitivity in the mono-lepton channel is incredibly weak even with 3000 fb^{-1} and is significantly worse than those from all other channels, especially the one from the di-jet analysis. The conclusion of the authors is identical to the conclusion of this study: that the mono-lepton channel is not sensitive enough for the DM searches and is significantly worse compared to hadronic channels.

Bibliography

[1] SLD Electroweak Group, DELPHI, ALEPH, SLD, SLD Heavy Flavour Group, OPAL, LEP Electroweak Working Group, L3 Collaboration, S. Schael et al., *Precision electroweak measurements on the Z resonance*, Phys. Rept. **427** (2006) 257–454, arXiv:hep-ex/0509008 [hep-ex].

[2] Particle Data Group Collaboration, K. A. Olive et al., *Review of Particle Physics*, Chin. Phys. **C38** (2014) 090001.

[3] G. Arnison et al., *Experimental observation of isolated large transverse energy electrons with associated missing energy at s=540 GeV*, Physics Letters B **122** no. 1, (1983) 103 − 116. http://www.sciencedirect.com/science/article/pii/0370269383911772.

[4] P. Bagnaia et al., *Evidence for $Z_0 \rightarrow e^+e$ at the CERN pp collider*, Physics Letters B **129** no. 1, (1983) 130 − 140. http://www.sciencedirect.com/science/article/pii/037026938390744X.

[5] TASSO Collaboration, R. Brandelik et al., *Evidence for Planar Events in e+ e-Annihilation at High-Energies*, Phys. Lett. **B86** (1979) 243–249.

[6] ATLAS Collaboration, *Observation of a new particle in the search for the Standard Model Higgs boson with the ATLAS detector at the LHC*, Phys.Lett. **B716** (2012) 1–29, arXiv:1207.7214 [hep-ex].

[7] CMS Collaboration, *Observation of a new boson at a mass of 125 GeV with the CMS experiment at the LHC*, Phys.Lett. **B716** (2012) 30–61, arXiv:1207.7235 [hep-ex].

[8] https://twiki.cern.ch/twiki/bin/view/AtlasPublic/ StandardModelPublicResults.

[9] Y. Gershtein et al., *Working Group Report: New Particles, Forces, and Dimensions*, in

Proceedings, Community Summer Study 2013: Snowmass on the Mississippi (CSS2013): Minneapolis, MN, USA, July 29-August 6, 2013. 2013.
arXiv:1311.0299 [hep-ex].
https://inspirehep.net/record/1263192/files/arXiv:1311.0299.pdf.

[10] M. C. Brak, *The Hierarchy Problem in the Standard Model and Little Higgs Theories*, Master's thesis, NIKHEF, 2004.
https://www.nikhef.nl/pub/theory/masters-theses/maarten_brak.pdf.

[11] Super-Kamiokande Collaboration, Y. Fukuda et al., *Measurements of the solar neutrino flux from Super-Kamiokande's first 300 days*, Phys. Rev. Lett. **81** (1998) 1158–1162, arXiv:hep-ex/9805021 [hep-ex]. [Erratum: Phys. Rev. Lett.81,4279(1998)].

[12] R. N. Mohapatra and G. Senjanovic, *Neutrino Mass and Spontaneous Parity Violation*, Phys. Rev. Lett. **44** (1980) 912.

[13] J. Ellis, *Searching for Particle Physics Beyond the Standard Model at the LHC and Elsewhere*, AIP Conf. Proc. **1446** (2012) 9–28, arXiv:1102.5009 [hep-ph].

[14] W. de Boer, *Grand unified theories and supersymmetry in particle physics and cosmology*, Prog. Part. Nucl. Phys. **33** (1994) 201–302, arXiv:hep-ph/9402266 [hep-ph].

[15] P. Langacker, R. W. Robinett, and J. L. Rosner, *New Heavy Gauge Bosons in p p and p anti-p Collisions*, Phys. Rev. **D30** (1984) 1470.

[16] M. Cvetic and S. Godfrey, *Discovery and identification of extra gauge bosons*, arXiv:hep-ph/9504216 [hep-ph].

[17] G. Azuelos, K. Benslama, and J. Ferland, *Prospects for the search for a doubly-charged Higgs in the left-right symmetric model with ATLAS*, J. Phys. **G32** no. 2, (2006) 73–91, arXiv:hep-ph/0503096 [hep-ph].

[18] W. Grimus, *Introduction to left-right symmetric models*,.
http://lss.fnal.gov/archive/other/uwthph-1993-10.pdf.

[19] T. Han, H. E. Logan, B. McElrath, and L.-T. Wang, *Phenomenology of the little Higgs model*, Phys. Rev. **D67** (2003) 095004, arXiv:hep-ph/0301040 [hep-ph].

[20] M. Benedikt, P. Collier, V. Mertens, J. Poole, and K. Schindl, *LHC Design Report. 3. The LHC injector chain*,.

[21] O. S. Bruning, P. Collier, P. Lebrun, S. Myers, R. Ostojic, J. Poole, and P. Proudlock, *LHC Design Report Vol.1: The LHC Main Ring,*.

[22] T. Kawamoto, S. Vlachos, L. Pontecorvo, J. Dubbert, G. Mikenberg, P. Iengo, C. Dallapiccola, C. Amelung, L. Levinson, R. Richter, and D. Lellouch, *New Small Wheel Technical Design Report*, Tech. Rep. CERN-LHCC-2013-006. ATLAS-TDR-020, Jun, 2013. https://cds.cern.ch/record/1552862. ATLAS New Small Wheel Technical Design Report.

[23] F. Akesson, T. Atkinson, M. J. Costa, M. Elsing, S. Fleischmann, A. Gaponenko, W. Liebig, E. Moyse, A. Salzburger, and M. Siebel, *ATLAS tracking event data model,*.

[24] T. G. Cornelissen, N. Van Eldik, M. Elsing, W. Liebig, E. Moyse, N. Piacquadio, K. Prokofiev, A. Salzburger, and A. Wildauer, *Updates of the ATLAS Tracking Event Data Model (Release 13),*.

[25] ATLAS Collaboration Collaboration, *ATLAS magnet system: Technical Design Report, 1.* Technical Design Report ATLAS. CERN, Geneva, 1997. https://cds.cern.ch/record/338080.

[26] ATLAS Collaboration Collaboration, N. Wermes and G. Hallewel, *ATLAS pixel detector: Technical Design Report.* Technical Design Report ATLAS. CERN, Geneva, 1998. https://cds.cern.ch/record/381263.

[27] ATLAS TRT Collaboration, E. Abat et al., *The ATLAS Transition Radiation Tracker (TRT) proportional drift tube: Design and performance*, JINST **3** (2008) P02013.

[28] ATLAS TRT Collaboration, E. Abat et al., *The ATLAS TRT barrel detector*, JINST **3** (2008) P02014.

[29] E. Abat et al., *The ATLAS TRT end-cap detectors*, JINST **3** (2008) P10003.

[30] ATLAS Collaboration, G. Aad et al., *Electron reconstruction and identification efficiency measurements with the ATLAS detector using the 2011 LHC proton-proton collision data*, Eur. Phys. J. **C74** no. 7, (2014) 2941, arXiv:1404.2240 [hep-ex].

[31] ATLAS Collaboration, *Measurement of the muon reconstruction performance of the ATLAS detector using 2011 and 2012 LHC proton-proton collision data*, Eur. Phys. J. **C74** no. 5, (2014) 3130, arXiv:1407.3935 [hep-ex].

[32] ATLAS Collaboration Collaboration, P. Jenni, M. Nessi, M. Nordberg, and

K. Smith, *ATLAS high-level trigger, data-acquisition and controls: Technical Design Report.* Technical Design Report ATLAS. CERN, Geneva, 2003.
https://cds.cern.ch/record/616089.

[33] A. Hawkins, *Searches for beyond Standard Model physics with same-sign dileptons.* PhD thesis, Lund U., 2014-10-20.
http://inspirehep.net/record/1429567/files/fulltext_mMv9hN.pdf.

[34] R. Veenhof, *Garfield, a drift chamber simulation program*, Conf. Proc. **C9306149** (1993) 66–71. [,66(1993)].

[35] https://atlas.web.cern.ch/Atlas/GROUPS/PHYSICS/PLOTS/TRT-2016-001/.

[36] J. H. Hubbell and S. M. Seltzer, *Tables of X-ray mass attenuation coefficients and mass energy-absorption coefficients 1 keV to 20 MeV for elements Z=1 to 92 and 48 additional substances of dosimetric interest*, Tech. Rep. NISTIR-5632, May, 1995.
http://cds.cern.ch/record/353989.

[37] ATLAS Collaboration Collaboration, *ATLAS inner detector: Technical Design Report, Volume 1.* Technical Design Report ATLAS. CERN, Geneva, 1997.
https://cds.cern.ch/record/331063.

[38] ATLAS Collaboration Collaboration, S. Haywood, L. Rossi, R. Nickerson, and A. Romaniouk, *ATLAS inner detector: Technical Design Report, Volume 2.* Technical Design Report ATLAS. CERN, Geneva, 1997.
https://cds.cern.ch/record/331064.

[39] E. Abat et al., *The ATLAS TRT electronics*, JINST **3** (2008) P06007.

[40] ATLAS Collaboration, G. Aad et al., *The ATLAS Experiment at the CERN Large Hadron Collider*, JINST **3** (2008) S08003.

[41] A. Alonso, *Transition Radiation Tracker calibration, searches beyond the Standard Model and multiparticle correlations in ATLAS.* PhD thesis, Lund U., Apr, 2012.
https://cds.cern.ch/record/1452211.

[42] W. Blum, W. Riegler, and L. Rolandi, *Particle detection with drift chambers.* Springer-Verlag, Berlin, Heidelberg, 2008.
http://dx.doi.org/10.1007/978-3-540-76684-1.

[43] R. L. Gluckstern, *Uncertainties in track momentum and direction, due to multiple scattering and measurement errors*, Nucl. Instrum. Meth. **24** (1963) 381–389.

[44] ATLAS Collaboration, G. Aad et al., *The ATLAS Inner Detector commissioning and calibration*, Eur. Phys. J. **C70** (2010) 787–821, `arXiv:1004.5293 [physics.ins-det]`.

[45] T. Sjöstrand, S. Mrenna, and P. Z. Skands, *PYTHIA 6.4 Physics and Manual*, JHEP **05** (2006) 026, `arXiv:hep-ph/0603175 [hep-ph]`.

[46] G. Corcella et al., *HERWIG 6: An Event generator for hadron emission reactions with interfering gluons (including supersymmetric processes)*, JHEP **01** (2001) 010, `hep-ph/0011363; hep-ph/0210213`.

[47] T. Gleisberg et al., *Event generation with SHERPA 1.1*, JHEP **02** (2009) 007, `arXiv:0811.4622 [hep-ph]`.

[48] GEANT4 Collaboration, S. Agostinelli et al., *GEANT4: A Simulation toolkit*, Nucl. Instrum. Meth. **A506** (2003) 250–303.

[49] ATLAS Collaboration, G. Aad et al., *The ATLAS Simulation Infrastructure*, Eur. Phys. J. **C70** (2010) 823–874, `arXiv:1005.4568 [physics.ins-det]`.

[50] T. H. Kittelmann, *Slepton spin determination and simulation of the transition radiation tracker at the ATLAS experiment*. PhD thesis, Copenhagen U., 2007. `https://cds.cern.ch/record/2224292`.

[51] W. W. M. Allison and J. H. Cobb, *Relativistic Charged Particle Identification by Energy Loss*, Ann. Rev. Nucl. Part. Sci. **30** (1980) 253–298.

[52] G. Marr and J. West, *Absolute photoionization cross-section tables for helium, neon, argon, and krypton in the VUV spectral regions*, Atomic Data and Nuclear Data Tables **18** no. 5, (1976) 497 – 508. `http://www.sciencedirect.com/science/article/pii/0092640X76900152`.

[53] P. Cwetanski, F. Dittus, and R. Orava, *Straw Performance Studies and Quality Assurance for the ATLAS Transition Radiation Tracker*. PhD thesis, Helsinki U., Helsinki, 2006. `https://cds.cern.ch/record/962570`.

[54] E. B. Klinkby, *W mass measurement and simulation of the transition radiation tracker at the ATLAS experiment*. PhD thesis, Copenhagen U., Copenhagen, 2008. `https://cds.cern.ch/record/1123367`.

[55] ATLAS TRT Collaboration, T. Akesson et al., *ATLAS Transition radiation tracker test-beam results*, Nucl. Instrum. Meth. **A522** (2004) 50–55.

[56] A. Romaniouk. Personal communication.

[57] ATLAS Collaboration, G. Aad et al., *Improved luminosity determination in pp collisions at sqrt(s) = 7 TeV using the ATLAS detector at the LHC*, Eur. Phys. J. **C73** no. 8, (2013) 2518, arXiv:1302.4393 [hep-ex].

[58] S. van der Meer, *Calibration of the effective beam height in the ISR*, Tech. Rep. CERN-ISR-PO-68-31. ISR-PO-68-31, CERN, Geneva, 1968. https://cds.cern.ch/record/296752.

[59] C. Rubbia, *Measurement of the luminosity of p−overlinep collider with a (generalized) Van der Meer Method*, Tech. Rep. CERN-p$\overline{p}$-Note-38, CERN, Geneva, Nov, 1977. http://cds.cern.ch/record/1025746.

[60] G. L. Alberghi et al., *Choice and characterization of photomultipliers for the new ATLAS LUCID detector*, JINST **11** no. 05, (2016) P05014.

[61] https://www.arduino.cc/.

[62] H. H. E. 3a, *Photomultiplier tubes, Basics and applications*,. https://www.hamamatsu.com/resources/pdf/etd/PMT_handbook_v3aE.pdf.

[63] ATLAS Collaboration, M. Aaboud et al., *Luminosity determination in pp collisions at $\sqrt{s}$ = 8 TeV using the ATLAS detector at the LHC*, arXiv:1608.03953 [hep-ex].

[64] ATLAS Collaboration, G. Aad et al., *Luminosity Determination in pp Collisions at $\sqrt{s} = 7$ TeV Using the ATLAS Detector at the LHC*, Eur. Phys. J. **C71** (2011) 1630, arXiv:1101.2185 [hep-ex].

[65] ATLAS Collaboration, *Luminosity Determination Using the ATLAS Detector*,.

[66] ATLAS Collaboration Collaboration, *Updated Luminosity Determination in pp Collisions at root(s)=7 TeV using the ATLAS Detector*, Tech. Rep. ATLAS-CONF-2011-011, CERN, Geneva, Mar, 2011. https://cds.cern.ch/record/1334563.

[67] ATLAS Collaboration, *Luminosity Determination in pp Collisions at sqrt(s) = 7 TeV using the ATLAS Detector in 2011*,.

[68] ATLAS Collaboration, *Improved Luminosity Determination in **pp** Collisions at $\sqrt{\mathbf{s}} = \mathbf{7}$ TeV using the ATLAS Detector at the LHC*,.

[69] ATLAS Collaboration, G. Aad et al., *Search for heavy Majorana neutrinos with the*

ATLAS detector in pp collisions at $\sqrt{s} = 8$ *TeV*, JHEP **07** (2015) 162, `arXiv:1506.06020 [hep-ex]`.

[70] ATLAS Collaboration, G. Aad et al., *Search for direct production of charginos, neutralinos and sleptons in final states with two leptons and missing transverse momentum in pp collisions at* $\sqrt{s} = 8$ *TeV with the ATLAS detector*, JHEP **05** (2014) 071, `arXiv:1403.5294 [hep-ex]`.

[71] ATLAS Collaboration, G. Aad et al., *Search for supersymmetry at* $\sqrt{s}=8$ *TeV in final states with jets and two same-sign leptons or three leptons with the ATLAS detector*, JHEP **06** (2014) 035, `arXiv:1404.2500 [hep-ex]`.

[72] H.-L. Lai, M. Guzzi, J. Huston, Z. Li, P. M. Nadolsky, J. Pumplin, and C. P. Yuan, *New parton distributions for collider physics*, Phys. Rev. **D82** (2010) 074024, `arXiv:1007.2241 [hep-ph]`.

[73] J. M. Campbell and R. K. Ellis, *MCFM for the Tevatron and the LHC*, Nucl. Phys. Proc. Suppl. (2010) 205, `arXiv:1007.3492 [hep-ph]`.

[74] J. Alwall, M. Herquet, F. Maltoni, O. Mattelaer, and T. Stelzer, *MadGraph/MadEvent v4: The New Web Generation*, JHEP **09** (2007) 028, `arXiv:0706.2334 [hep-ph]`.

[75] J. Pumplin et al., *New Generation of Parton Distributions with Uncertainties from Global QCD Analysis*, JHEP **07** (2002) 012, `hep-ph/0201195`.

[76] T. Sjöstrand, S. Mrenna, and P. Skands, *A Brief Introduction to PYTHIA 8.1*, Comput. Phys. Commun. **178** (2008) 852, `arXiv:0710.3820 [hep-ph]`.

[77] A. Kardos et al., *Top quark pair production in association with a Z-boson at NLO accuracy*, Phys. Rev. **D 85** (2012) 054015, `arXiv:1111.0610 [hep-ph]`.

[78] J. M. Campbell, and R. K. Ellis, $t\bar{t}W^{\pm}$ *production and decay at NLO*, JHEP **07** (2012) 052, `arXiv:1204.5678 [hep-ph]`.

[79] M. L. Mangano et al., *ALPGEN, a generator for hard multiparton processes in hadronic collisions*, JHEP **07** (2003) 001, `arXiv:hep-ph/0206293`.

[80] S. Catani et al., *Vector boson production at hadron colliders: A fully exclusive QCD calculation at NNLO*, Phys. Rev. Lett. **103** (2009) 082001, `arXiv:0903.2120 [hep-ph]`.

[81] G. Marchesini et al., *HERWIG: a Monte Carlo event generator for simulating hadron emission reactions with interfering gluons. Version 5.1 - april 1991*, Comput. Phys. Commun. **67** (1992) 465.

[82] A. D. Martin, W. J. Stirling, R. S. Thorne, and G. Watt, *Parton distributions for the LHC*, Eur. Phys. J. **C 63** (2009) 189, `arXiv:0901.0002 [hep-ph]`.

[83] S. Frixione, and B. R. Webber, *Matching NLO QCD computations and parton shower simulations*, JHEP **06** (2002) 029, `arXiv:hep-ph/0204244 [hep-ph]`.

[84] S. Frixione, F. Stoeckli, P. Torrielli, B. R. Webber, and C. D. White, *The MC@NLO 4.0 Event Generator*, `arXiv:1010.0819 [hep-ph]`.

[85] M. Cacciari et al., *Top-pair production at hadron colliders with next-to-next-to-leading logarithmic soft-gluon resummation*, Phys. Lett. **B 710** (2012) 612, `arXiv:1111.5869 [hep-ph]`.

[86] P. Bärnreuther, M. Czakon, and A. Mitov, *Percent Level Precision Physics at the Tevatron: First Genuine NNLO QCD Corrections to $q\bar{q} \to t\bar{t} + X$*, Phys. Rev. Lett. **109** (2012) 132001, `arXiv:1204.5201 [hep-ph]`.

[87] M. Czakon and A. Mitov, *NNLO corrections to top-pair production at hadron colliders: the all-fermionic scattering channels*, JHEP **12** (2012) 054, `arXiv:1207.0236 [hep-ph]`.

[88] M. Czakon and A. Mitov, *NNLO corrections to top pair production at hadron colliders: the quark-gluon reaction*, JHEP **01** (2013) 080, `arXiv:1210.6832 [hep-ph]`.

[89] M. Czakon, P. Fiedler, and A. Mitov, *The total top quark pair production cross-section at hadron colliders through $O(\alpha_s^4)$*, Phys. Rev. Lett. **110** (2013) 252004, `arXiv:1303.6254 [hep-ph]`.

[90] M. Czakon and A. Mitov, *Top++: A Program for the Calculation of the Top-Pair Cross-Section at Hadron Colliders*, Comput. Phys. Commun. **185** (2014) 2930, `arXiv:1112.5675 [hep-ph]`.

[91] N. Kidonakis, *NNLL resummation for s-channel single top quark production*, Phys. Rev. **D 81** (2010) 054028, `arXiv:1001.5034 [hep-ph]`.

[92] N. Kidonakis, *Two-loop soft anomalous dimensions for single top quark associated production with a W^- or H^-*, Phys. Rev. **D 82** (2010) 054018, `arXiv:1005.4451`

`[hep-ph]`.

[93] ATLAS Collaboration, G. Aad et al., *Search for anomalous production of prompt like-sign lepton pairs at $\sqrt{s} = 7$ TeV with the ATLAS detector*, JHEP **12** (2012) 007, `arXiv:1210.4538 [hep-ex]`.

[94] ATLAS Collaboration, G. Aad et al., *Search for same-sign top-quark production and fourth-generation down-type quarks in pp collisions at $\sqrt{s} = 7$ TeV with the ATLAS detector*, JHEP **04** (2012) 069, `arXiv:1202.5520 [hep-ex]`.

[95] D0 Collaboration, V. M. Abazov et al., *Measurement of the shape of the boson rapidity distribution for $p\bar{p} \to Z/gamma^* \to e^+e^- + X$ events produced at $\sqrt{s}$ of 1.96-TeV*, Phys. Rev. **D76** (2007) 012003, `arXiv:hep-ex/0702025 [HEP-EX]`.

[96] ATLAS Collaboration, G. Aad et al., *Electron reconstruction and identification efficiency measurements with the ATLAS detector using the 2011 LHC proton-proton collision data*, Eur. Phys. J. **C74** no. 7, (2014) 2941, `arXiv:1404.2240 [hep-ex]`.

[97] ATLAS Collaboration, G. Aad et al., *Electron and photon energy calibration with the ATLAS detector using LHC Run 1 data*, Eur. Phys. J. **C74** no. 10, (2014) 3071, `arXiv:1407.5063 [hep-ex]`.

[98] M. Botje et al., *The PDF4LHC Working Group Interim Recommendations*, `arXiv:1101.0538 [hep-ph]`.

[99] J. M. Campbell, R. K. Ellis, and C. Williams, *Vector boson pair production at the LHC*, JHEP **07** (2011) 018, `arXiv:1105.0020 [hep-ph]`.

[100] J. M. Campbell and R. K. Ellis, *$t\bar{t}W^{+-}$ production and decay at NLO*, JHEP **07** (2012) 052, `arXiv:1204.5678 [hep-ph]`.

[101] M. V. Garzelli, A. Kardos, C. G. Papadopoulos, and Z. Trocsanyi, *$t\bar{t}W^{+-}$ and $t\bar{t}Z$ Hadroproduction at NLO accuracy in QCD with Parton Shower and Hadronization effects*, JHEP **11** (2012) 056, `arXiv:1208.2665 [hep-ph]`.

[102] A. L. Read, *Presentation of search results: The CL(s) technique*, J. Phys. **G28** (2002) 2693–2704. [,11(2002)].

[103] A. L. Read, *Modified frequentist analysis of search results (The CL(s) method),*. `http://weblib.cern.ch/abstract?CERN-OPEN-2000-205`.

[104] L. Moneta, K. Belasco, K. S. Cranmer, S. Kreiss, A. Lazzaro, D. Piparo, G. Schott,

W. Verkerke, and M. Wolf, *The RooStats Project*, PoS **ACAT2010** (2010) 057, `arXiv:1009.1003 [physics.data-an]`.

[105] M. Muhlleitner and M. Spira, *A Note on doubly charged Higgs pair production at hadron colliders*, Phys. Rev. **D68** (2003) 117701, `arXiv:hep-ph/0305288 [hep-ph]`.

[106] ATLAS Collaboration, G. Aad et al., *Search for anomalous production of prompt same-sign lepton pairs and pair-produced doubly charged Higgs bosons with $\sqrt{s} = 8$ TeV pp collisions using the ATLAS detector*, JHEP **03** (2015) 041, `arXiv:1412.0237 [hep-ex]`.

[107] ATLAS Collaboration, G. Aad et al., *Search for anomalous production of prompt like-sign lepton pairs at $\sqrt{s} = 7$ TeV with the ATLAS detector*, JHEP **12** (2012) 007, `arXiv:1210.4538 [hep-ex]`.

[108] ATLAS Collaboration, G. Aad et al., *Search for doubly-charged Higgs bosons in like-sign dilepton final states at $\sqrt{s} = 7$ TeV with the ATLAS detector*, Eur. Phys. J. **C72** (2012) 2244, `arXiv:1210.5070 [hep-ex]`.

[109] ATLAS Collaboration, T. A. collaboration, *Search for doubly-charged Higgs bosons in same-charge electron pair final states using proton-proton collisions at $\sqrt{s} = 13$ TeV with the ATLAS detector,*.

[110] S. Alioli, P. Nason, C. Oleari, and E. Re, *A general framework for implementing NLO calculations in shower Monte Carlo programs: the POWHEG BOX*, JHEP **06** (2010) 043, `arXiv:1002.2581 [hep-ph]`.

[111] S. Dulat et al., *The CT14 Global Analysis of Quantum Chromodynamics*, Phys. Rev. D **93** (2016) 033006, `arXiv:1506.07443 [hep-ph]`.

[112] C. Anastasiou, L. Dixon, K. Melnikov, and F. Petriello, *High precision QCD at hadron colliders: Electroweak gauge boson rapidity distributions at NNLO*, Phys. Rev. D **69** (2004) 094008, `arXiv:hep-ph/0312266 [hep-ph]`.

[113] D. Bardin et al., *SANC integrator in the progress: QCD and EW contributions*, JETP Lett. **96** (2012) 285, `arXiv:1207.4400 [hep-ph]`.

[114] S. G. Bondarenko and A. A. Sapronov, *NLO EW and QCD proton-proton cross section calculations with mcsanc-v1.01*, Comput. Phys. Commun. **184** (2013) 2343,

arXiv:1301.3687 [hep-ph].

[115] ATLAS Collaboration, G. Aad et al., *Muon reconstruction performance of the ATLAS detector in protonâĂŞproton collision data at* $\sqrt{s}$ *=13 TeV*, Eur. Phys. J. **C76** no. 5, (2016) 292, arXiv:1603.05598 [hep-ex].

[116] ATLAS Collaboration Collaboration, *Electron efficiency measurements with the ATLAS detector using the 2015 LHC proton-proton collision data*, Tech. Rep. ATLAS-CONF-2016-024, CERN, Geneva, Jun, 2016. http://cds.cern.ch/record/2157687.

[117] ATLAS Collaboration, G. Aad et al., *Jet energy measurement with the ATLAS detector in proton-proton collisions at* $\sqrt{s} = 7$ *TeV*, Eur. Phys. J. **C73** no. 3, (2013) 2304, arXiv:1112.6426 [hep-ex].

[118] *Expected performance of missing transverse momentum reconstruction for the ATLAS detector at* $\sqrt{s} = 13$ *TeV*, Tech. Rep. ATL-PHYS-PUB-2015-023, CERN, Geneva, Jul, 2015. https://cds.cern.ch/record/2037700.

[119] *Performance of missing transverse momentum reconstruction for the ATLAS detector in the first proton-proton collisions at at* $\sqrt{s}=$ *13 TeV*, Tech. Rep. ATL-PHYS-PUB-2015-027, CERN, Geneva, Jul, 2015. https://cds.cern.ch/record/2037904.

[120] ATLAS Collaboration, G. Aad et al., *Identification and energy calibration of hadronically decaying tau leptons with the ATLAS experiment in pp collisions at* $\sqrt{s}=8$ *TeV*, Eur. Phys. J. **C75** no. 7, (2015) 303, arXiv:1412.7086 [hep-ex].

[121] ATLAS Collaboration Collaboration, *Measurements of the photon identification efficiency with the ATLAS detector using 4.9 fbâĹŠ1 of pp collision data collected in 2011*, Tech. Rep. ATLAS-CONF-2012-123, CERN, Geneva, Aug, 2012. http://cds.cern.ch/record/1473426.

[122] M. Cacciari, G. P. Salam, and G. Soyez, *The Anti-k(t) jet clustering algorithm*, JHEP **04** (2008) 063, arXiv:0802.1189 [hep-ph].

[123] *Jet Calibration and Systematic Uncertainties for Jets Reconstructed in the ATLAS Detector at* $\sqrt{s} = 13$ *TeV*, Tech. Rep. ATL-PHYS-PUB-2015-015, CERN, Geneva, Jul, 2015. https://cds.cern.ch/record/2037613.

[124] ATLAS Collaboration, G. Aad et al., *Search for high-mass dilepton resonances in pp*

collisions at $\sqrt{s} = 8$âĂĽâĂĽTeV with the ATLAS detector, Phys. Rev. **D90** no. 5, (2014) 052005, arXiv:1405.4123 [hep-ex].

[125] *Muon reconstruction performance in early $\sqrt{s} = 13$ TeV data*, Tech. Rep. ATL-PHYS-PUB-2015-037, CERN, Geneva, Aug, 2015. https://cds.cern.ch/record/2047831.

[126] ATLAS Collaboration, ATLAS Collaboration, *A method for the construction of strongly reduced representations of ATLAS experimental uncertainties and the application thereof to the jet energy scale*, ATL-PHYS-PUB-2015-014 (2015). https://cds.cern.ch/record/2037436.

[127] NNPDF Collaboration, R. D. Ball et al., *Parton distributions for the LHC Run II*, JHEP **04** (2015) 040, arXiv:1410.8849 [hep-ph].

[128] ATLAS Collaboration, M. Aaboud et al., *Search for new resonances in events with one lepton and missing transverse momentum in pp collisions at $\sqrt{s} = 13$ TeV with the ATLAS detector*, arXiv:1606.03977 [hep-ex].

[129] F. Beaujean, A. Caldwell, D. Kollar, and K. Kroninger, *BAT: The Bayesian analysis toolkit*, J. Phys. Conf. Ser. **331** (2011) 072040.

[130] ATLAS Collaboration, G. Aad et al., *Search for new particles in events with one lepton and missing transverse momentum in pp collisions at $\sqrt{s} = 8$ TeV with the ATLAS detector*, JHEP **09** (2014) 037, arXiv:1407.7494 [hep-ex].

[131] ATLAS Collaboration, ATLAS Collaboration, *Search for a heavy gauge boson decaying to a charged lepton and a neutrino in 1 fb^{-1} of pp collisions at $\sqrt{s} = 7$ TeV using the ATLAS detector*, Phys. Lett. B **705** (2011) 28, arXiv:1108.1316 [hep-ex].

[132] ATLAS Collaboration, ATLAS Collaboration, *Search for high-mass states with one lepton plus missing transverse momentum in proton-proton collisions at $\sqrt{s} = 7$ TeV with the ATLAS detector*, Phys. Lett. B **701** (2011) 50, arXiv:1103.1391 [hep-ex].

[133] ATLAS Collaboration, T. A. collaboration, *Search for new resonances decaying to a charged lepton and a neutrino in pp collisions at $\sqrt{s} = 13$ TeV with the ATLAS detector*,.

[134] CMS Collaboration, V. Khachatryan et al., *Search for physics beyond the standard model in final states with a lepton and missing transverse energy in proton-proton*

collisions at sqrt(s) = 8 TeV, Phys. Rev. **D91** no. 9, (2015) 092005, `arXiv:1408.2745 [hep-ex]`.

[135] CMS Collaboration, C. Collaboration, *Search for SSM W' production, in the lepton+MET final state at a center-of-mass energy of 13 TeV,*.

[136] D. Abercrombie et al., *Dark Matter Benchmark Models for Early LHC Run-2 Searches: Report of the ATLAS/CMS Dark Matter Forum*, `arXiv:1507.00966 [hep-ex]`.

[137] N. F. Bell, Y. Cai, J. B. Dent, R. K. Leane, and T. J. Weiler, *Dark matter at the LHC: Effective field theories and gauge invariance*, Phys. Rev. **D92** no. 5, (2015) 053008, `arXiv:1503.07874 [hep-ph]`.

[138] N. F. Bell, Y. Cai, and R. K. Leane, *Mono-W Dark Matter Signals at the LHC: Simplified Model Analysis*, JCAP **1601** no. 01, (2016) 051, `arXiv:1512.00476 [hep-ph]`.

[139] J. Goodman, M. Ibe, A. Rajaraman, W. Shepherd, T. M. P. Tait, and H.-B. Yu, *Constraints on Dark Matter from Colliders*, Phys. Rev. **D82** (2010) 116010, `arXiv:1008.1783 [hep-ph]`.

[140] L. M. Carpenter, A. Nelson, C. Shimmin, T. M. P. Tait, and D. Whiteson, *Collider searches for dark matter in events with a Z boson and missing energy*, Phys. Rev. **D87** no. 7, (2013) 074005, `arXiv:1212.3352 [hep-ex]`.

[141] J. Abdallah et al., *Simplified Models for Dark Matter Searches at the LHC*, Phys. Dark Univ. **9-10** (2015) 8–23, `arXiv:1506.03116 [hep-ph]`.

[142] *Sensitivity to WIMP Dark Matter in the Final States Containing Jets and Missing Transverse Momentum with the ATLAS Detector at 14 TeV LHC*, Tech. Rep. ATL-PHYS-PUB-2014-007, CERN, Geneva, Jun, 2014. `https://cds.cern.ch/record/1708859`.

This thesis covers two searches for new physics in the ATLAS experiment, which uses proton-proton collisions provided by the Large Hadron Collider. These searches are performed by the comparison of the observed number of events containing high momentum leptons with a prediction by the Standard Model. Also, a number of studies are presented related to the design, performance and operation of the ATLAS luminosity monitor called LUCID, as well as the description of the simulation of the ATLAS Transition Radiation Tracker with a new Argon-based gas mixture.